Ultra-High Vacuum Systems for Experiments with Cold Atoms in Space

Vom Fachbereich Produktionstechnik

der

UNIVERSITÄT BREMEN

zur Erlangung des Grades
Doktor der Ingenieurwissenschaften (Dr.-Ing.)
genehmigte

Dissertation

von

Michael Elsen, M. Sc.

Gutachter:	Prof. Dr. rer. nat. Claus Braxmaier
	Prof. Dr. rer. nat. Hansjörg Dittus

Tag der mündlichen Prüfung: 06.06.2023

Ich habe die vorgelegte Dissertation selbständig, ohne unerlaubte fremde Hilfe und nur mit den Hilfen angefertigt, die ich in der Dissertation angegeben habe. Alle Textstellen, die wörtlich oder sinngemäß aus veröffentlichten oder nicht veröffentlichten Schriften entnommen sind, sind als solche kenntlich gemacht.

Michael Elsen

Abstract

Dual-species atom interferometry, with Bose-Einstein condensates, is a promising technique for ultra-precise and accurate measurements for spaceborne applications, such as inertial sensing, future detection of gravitational waves, earth observation, and testing fundamental physics. An ultracold atom experiment on a future satellite mission could improve the precision of testing general relativity, with the test of the universality of free fall. The technology discovery of such a complex and challenging experiment, requires a multitude of space qualified technologies and developments.

The MAIUS-2/3 (Matter-Wave Interferometry Under Microgravity) missions, within the QUANTUS (Quantum Gases in Microgravity) consortium, aims to perform the first dual-species atom interferometer with ultracold rubidium and potassium atoms on a sounding rocket. It is used as a pathfinder mission to further develop the technologies which enable future cold atom missions. Space suitable ultra-high vacuum (UHV) systems are one of the enabling technologies for missions on long-duration microgravity platforms, such as the International Space Station or a satellite.

The scientific payload MAIUS-B, flying on both missions MAIUS-2 and MAIUS-3, is introduced in this thesis. The payload is sheltered within seven RADAX (radial-axial) hull segments, and is divided into five subsystems; electronics, physics package, laser system, laser electronics, and batteries. The newly developed thermal control system and ground support equipment is capable of accounting for an internally produced heat load of 707.6 W and a temperature rise by aerodynamic drag during launch. The mass and size

was continuously optimized, with a final mass of 335.3 kg and a length of 2.8 m, which is within the limits of 340.0 kg and 3.0 m. A load assessment of the new suspension system showed that the payload is capable of carrying the MAIUS-B payload up to $981\,\mathrm{m\,s^{-2}}$ ($100\,\mathrm{g_0}$) within a reasonable safety margin. A new umbilical and sealing concept was implemented, providing the payload until lift-off with power, data, and cooling liquid connections.

The UHV system was redesigned to fit within the mass and size requirements. Two titanium sublimation pumps and one ion getter pump are maintaining a pressure of 2×10^{-11} hPa. This is one order of magnitude better than the experiment required pressure of 5×10^{-10} hPa. Several vacuum components, such as the differential pumping stage, the oven design, and the pumps itself, were modified or redesigned. The physics package, including the UHV system, was qualified for a vibration level of $19.6\,\mathrm{m\,s^{-2}_{RMS}}$ ($2.0\,\mathrm{g_{0RMS}}$), compared to the maximum flight level of $17.7\,\mathrm{m\,s^{-2}_{RMS}}$ ($1.8\,\mathrm{g_{0RMS}}$) throughout a sounding rocket mission. The UHV system is capable of regaining the required pressure within 19 s.

To investigate the influence of static loads on the leakage rate of ConFlat (CF) seals, a test setup was built. The tests were performed to indicate the influence on the tightening torque (10 N m, 12.5 N m, 15 N m), the flange material (aluminum [*AluVaC®*], stainless steel [316LN-ESR, 14429-ESU]), and different oxygen free high conductivity (OFHC) copper gaskets (annealed, non-annealed). The presented results provide the first data set on the leakage rate for CF DN40 flange connections tested up to a applied force of 1 950 N.

Zusammenfassung

Hochpräzise Atominterferometrie mit Bose-Einstein-Kondensaten (BEC) ist eine vielversprechende Technik für raumfahrtbasierte Anwendungen, wie die Detektion von Gravitationswellen, Sensoren zur Erdbeobachtung und Tests fundamentaler Physik mit bisher unerreichter Genauigkeit. Ein Experiment mit ultrakalten Atomen an Bord eines Satelliten könnte mithilfe des Tests der Universalität des freien Falls die Genauigkeit der Überprüfung der allgemeinen Relativitätstheorie verbessern. Aufgrund der Komplexität und den Herausforderungen eines solchen Experiments ist eine Vielzahl an Raumfahrt qualifizierten Technologien und Neuentwicklungen notwendig.

Die Missionen MAIUS-2/3 (Materiewelleninterferometer unter Schwerelosigkeit), innerhalb des QUANTUS-Konsortiums (Quantensysteme unter Schwerelosigkeit), hat die Durchführung des ersten Zwei-Spezies-Atominterferometer mit ultrakalten Rubidium- und Kaliumatomen auf einer Höhenforschungsrakete zum Ziel. Es wird als Pathfinder-Mission genutzt, um mit Hilfe von Technologieentwicklung zukünftige Missionen zu ermöglichen. Weltraumtaugliche Ultrahochvakuum (UHV)-Systeme sind eine der Schlüsseltechnologien für Missionen auf Mikrogravitationsplattformen, wie der Internationalen Raumstation oder einem Satelliten.

In dieser Arbeit wird die wissenschaftliche Nutzlast MAIUS-B vorgestellt, welche in beiden Missionen MAIUS-2 und MAIUS-3 fliegt. Die Nutzlast ist in sieben RADAX (Radial-Axial) Hüllensegmente untergebracht und in fünf Subsysteme unterteilt: Kontrollelektronik, Experimentapparatur, Lasersystem, Laserelektronik und Batterien. Das neu entwickelte Thermalkon-

trollsystem und die Bodenversorgung sind in der Lage, die intern erzeugte Wärmelast von 707.6 W und den Temperaturanstieg durch Luftwiderstand beim Start zu regulieren. Masse und Größe wurden kontinuierlich optimiert, sodass die endgültige Masse 335.3 kg und die Länge 2.8 m beträgt, was innerhalb der Grenzen von 340.0 kg und 3.0 m liegt. Eine Belastungsanalyse des neuen Aufhängungssystems hat gezeigt, dass sie in der Lage ist, die MAIUS-B-Nutzlast bis zu einer Belastung von $981\,\mathrm{m\,s^{-2}}$ ($100\,\mathrm{g_0}$) mit einer angemessenen Sicherheitsmarge zu tragen. Es wurde ein neues Versorgungs- und Dichtungskonzept umgesetzt, das die Nutzlast bis zum Raketenstart mit Strom-, Daten- und Kühlflüssigkeitsanschlüssen versorgt.

Das UHV-System wurde neu designt, um die Anforderungen an Masse und Größe zu erfüllen. Zwei Titansublimationspumpen und eine Ionengetterpumpe halten einen Druck von 2×10^{-11} hPa aufrecht. Dies ist um eine Größenordnung besser, als der für das Experiment erforderliche Druck von 5×10^{-10} hPa. Mehrere Vakuumkomponenten, wie z.B. die differentielle Pumpstufe, die Konstruktion des Ofens und die Pumpen selbst, wurden geändert oder neu konstruiert. Die Experimentapparatur, einschließlich des UHV-Systems, wurde für ein Vibrationsniveau von $19.6\,\mathrm{m\,s^{-2}_{RMS}}$ ($2.0\,\mathrm{g_{0RMS}}$) qualifiziert, verglichen mit dem maximalen Flugniveau von $17.7\,\mathrm{m\,s^{-2}_{RMS}}$ ($1.8\,\mathrm{g_{0RMS}}$) während einer Höhenforschungsraketenmission. Das UHV-System ist in der Lage, den erforderlichen Druck innerhalb von 19 s nach Auftreten der Last wiederherzustellen.

Um den Einfluss statischer Lasten auf die Leckrate von ConFlat (CF)-Dichtungen zu untersuchen, wurde ein Testaufbau entwickelt und aufgebaut. Die Tests wurden durchgeführt, um den Einfluss auf das Anzugsmoment (10 N m, 12.5 N m, 15 N m), das Flanschmaterial (Aluminium [*AluVaC®*], Edelstahl [316LN-ESR, 14429-ESU]) und verschiedene OFHC Kupferdichtungen (weichgeglüht, ungeglüht) zu testen. Die vorgestellten Ergebnisse liefern den ersten Datensatz über die Leckrate für DN40 CF-Flanschverbindungen, die bis zu einer Kraft von 1.950 N getestet wurden.

Contents

Abbreviations

ACES	Atomic Clock Ensemble in Space
AOM	Acousto-Optic Modulator
ARIS	Active Rack Isolation System
ASD	Acceleration Spectral Density
BA	Batteries
BEC	Bose-Einstein Condensate
BECCAL	Bose-Einstein Condensate and Cold Atom Laboratory
CAL	Cold Atom Lab
CDR	Critical Design Review
CEPF	Columbus External Payload Facility
CF	ConFlat
CMSP	China Manned Space Program
CNES	Centre National d'Etudes Spatiales
COTS	Commerial Off-The-Shelf
CPOT	Copper Pinch-Off Tube
DFB	Distributed Feedback
DKC	Delta-Kick Collimation
DLR	German Aerospace Center
DPS	Differential Pumping Stage
EC	Experiment Chamber
ECDL	Extended Cavity Diode Laser

ECLSS	Environmental Control and Life Support System
EL	Electronics
ESA	European Space Agency
EXPRESS	Expedite the Processing of Experiments to the Space Station
FCDP	Frequency Comparison and Distribution Package
GSE	Ground Support Equipment
IGP	Ion Getter Pump
ISPR	International Standard Payload Racks
ISS	International Space Station
JPL	Jet Propulsion Laboratory
LE	Laser Electronics
LEO	Low Earth Orbit
LS	Laser System
MAIUS	Matter-Wave Interferometry Under Microgravity
MICROSCOPE	Micro-Satellite à traînée Compensée pour l'Observation du Principe d'Equivalence
MOPA	Master-Oscillator-Power-Amplifier
MORABA	Mobile Rocket Base
MOT	Magneto-Optical Trap
MWL	Microwave Time-Transfer System
NASA	National Aeronautics and Space Administration
NEG	Non-Evaporable Getter
OFHC	Oxygen Free High Conductivity
PHARAO	Horloge Atomique par Refroidissement d'Atomes de Césium
PLL	Phase Lock Loop
PM	Polarization Maintaining
PP	Physics Package
PS	Pumping System

PSD	Power Spectral Density
QUANTUS	Quantum Gases in Microgravity
RADAX	Radial-Axial
RF	Radio-Frequency
RMS	Root-Mean-Square
SCAC	Space Cold Atom Clock
SHM	Space Hydrogen Maser
SIP	Sputter Ion Pump
SSC	Swedish Space Corporation
STE-QUEST	Spacetime Explorer and Quantum Equivalence Principle Space Test
TCS	Thermal Control System
TRL	Technology Readiness Level
TSP	Titanium Sublimation Pump
UFF	Universality of Free Fall
UHV	Ultra-High Vacuum
WEP	Weak Equivalence Principle
ZARM	Center of Applied Space Technology and Microgravity

1 Introduction

Within the QUANTUS (Quantum Gases in Microgravity) consortium, multiple universities and institutes are aiming to build up the knowledge and the necessary technologies to perform spaceborne dual-species atom interferometry with ultracold rubidium and potassium atoms. In the framework of fundamental science experiments in space, an atom interferometer with two ultracold atom clouds is a promising candidate for testing general relativity with high-precision, such as the test of the universality of free fall (UFF) as proposed in STE-QUEST (Spacetime Explorer and Quantum Equivalence Principle Space Test) [Agu14]. A future STE-QUEST-like satellite mission could improve the accuracy for the test of the UFF of matter waves within the earth's gravitational field, comparing the trajectory of two Bose-Einstein condensates (BECs). Such a mission takes advantage of the microgravity environment which allows measuring times not feasible for terrestrial experiments. Atom interferometry with ultracold atoms has the major advantage of being drift free and absolute calibrated, since the atomic properties are not changing.

An STE-QUEST-like satellite mission with a dual-species atom interferometer is a challenging task. The stringent requirements given on technologies and applications used throughout such a payload, makes an intensive technology development and space qualification essential. To pave the way for future STE-QUEST-like satellite missions, technology developments and demonstrations are more easily accessible on pathfinder microgravity platforms, such as sounding rockets.

The QUANTUS consortium started with two drop tower missions at the Center of Applied Space Technology and Microgravity (ZARM), producing the first BEC in 2007 within the QUANTUS-1 project [Zoe10]. The following project, QUANTUS-2, was built to perform dual-species atom interferometry, with rubidium-87 (^{87}Rb) and potassium-41 (^{41}K) [Her13]. With the ongoing experiment, QUANTUS-2 gains essential knowledge in the operation of a dual-species atom interferometer [Dep21]. Since the drop tower in Bremen only provides an experimental time of 4.7 s (in catapult mode 9.2 s), the next step was taken with the sounding rocket mission MAIUS-1 (Matter-Wave Interferometry Under Microgravity) [Bec18]. MAIUS-1 was successfully launched in January 2017 on a VSB-30 sounding rocket from Esrange in Sweden. During the 6 min microgravity time, the scientific payload MAIUS-A was able to create a ^{87}Rb BEC and conducted around 110 experiments central to matter-wave interferometry [Bec18]. Building up on this heritage, the next step, from a single-species experiment in MAIUS-1 (scientific payload MAIUS-A), to a dual-species experiment in MAIUS-2/3 with its scientific payload MAIUS-B, was undertaken. In chapter 5, a general mission overview of the MAIUS missions is given, and the scientific payload MAIUS-B with its five subsystems is introduced.

One of the crucial components for the success of ultracold atom experiments, ground or space based, is an ultra-high vacuum (UHV) system, as stated in [Alo22]. Such an experiment requires, according to [Sei14], a background pressure of $\leq 5 \times 10^{-10}$ hPa within its vacuum system. A higher background pressure leads to more collisions with the residual gas atoms and lowers the performance of the experiment. To optimize the experiment performance, the UHV system needs to be able to maintain the lowest pressure possible.

Such a vacuum system is further designed to provide a reliable, controllable and reproducible test environment. A pressure in this UHV region is a manageable task for a ground based experiment, using the available techniques and standard components. Once the UHV system is transferred to a spaceborne payload, special environmental conditions need to be taken into account. As

a part of this thesis, chapter 3 discusses the flight environment (mechanical, thermal and magnetic) of the most common microgravity platforms for ultracold atom experiments; sounding rockets, the International Space Station (ISS), or satellites. It also provides the requirements specification for the design and implementation of future spaceborne UHV systems, dedicated to ultracold atom experiments.

Some of the main influences on the UHV system are the mechanical loads during launch, the rocket ascent, stage separation, or in-orbit maneuvers. The vibrations from the rocket motors or their acceleration cause dynamic or static loads, respectively. These loads are applied to the overall payload including the vacuum system. The vacuum system needs to be able to withstand the mechanical loads, while at the same time maintaining the required pressure level to avoid decreased experiment performances. This makes a ground qualification process of the performance of the UHV system mandatory. During the ground qualification of the flight hardware including the vacuum system, vibration tests are used to simulate the applied dynamic loads during the mission. All components used for space missions, commercial or self designed, have to pass the ground qualification.

Throughout this thesis, a primary outcome was to newly design, assemble, integrate and qualify the MAIUS-B UHV system, as shown in detail in chapter 6. In section 6.2, the newly designed and implemented vacuum components of the UHV system are explained in detail. The vibration tests, as a main part of the ground qualification in MAIUS-B, were performed within the scope of this thesis and the test results are discussed in section 6.3.

A widely used design feature for UHV systems on ground and space based experiments are ConFlat (CF) flange connections. They produce a UHV-tight connection, can be immediately integrated, and are available for many applications as standard parts. Although these flanges are commonly used within space missions, no data sets are available on the influence of external mechanical loads. These loads could result in a leakage rate through the CF flange, which will decrease the pressure of the vacuum system and lower the

performance of the experiment. While the overall vacuum system is vibration tested on a shaker, the impact of the static loads on the CF flange connection stays unknown. This data can be used for current and future space missions to improve and optimize the design, as well as for the final assembly process of space suitable UHV systems. To provide the science community with the first data set, chapter 7 reports on the tests conducted as a component of the main outcome of this thesis. The investigations on the influencing parameters of the CF flange connections, such as the tightening torque, the sealing gasket, or the flange material, are further discussed. Section 7.2 starts with the test requirements and introduces the test setup and its methodology. The test setup was newly built and the methodology was specifically created for the purposes of this thesis. The following section 7.3, presents the discussion of the test results and gives a comparison and summary of the findings of the conducted tests.

Another important design driver for spaceborne missions is the compactness and the miniaturization of an experimental setup, which can fill up a whole laboratory in ground based experiments. To fulfill this goal, common commercial components and new technologies need to be optimized and adapted in such a way that they are able to withstand the mechanical loads throughout the launch, and the actual flight mission. For the new scientific payload MAIUS-B, this required an extensive adaption of the payload suspension and the overall mechanical design. The changes of the suspension and its load and safety assessment, which have been performed as a part of this thesis, are shown and discussed in section 5.7.2.

Beside the size constraints, an intensive mass optimization is an essential engineering task for all space missions. The overall mass budget has a high impact throughout the mission, either in a cost perspective or as a direct impact on the mission architecture itself. The reachable apogee of a parabolic flight of a sounding rocket, for example, correlates directly with the obtainable microgravity and experimental time. In this case, the achievable thrust is given by the rocket for a certain motor setup, but a higher weight results in

a lower apogee and therefore in a shorter experimental/microgravity time. In section 5.7.1, the discussed optimizations of the mass and the length budget is one of the outcomes of this thesis. It is one of the main key elements for the successful transition from a single-species experiment in MAIUS-1 (MAIUS-A) to a dual-species experiment for MAIUS-2/3 (MAIUS-B).

Such a dual-species atom interferometer requires a high amount of supply and control electronics for the main experiment, and for the mission essential components, such as the laser system or the overall power supply. Compared to ground based experiments, an autonomous operation of the payload is required throughout main phases of the mission, depending on the chosen microgravity platform. Space stations like the ISS provide the experiment with power for its in-orbit operation. During the direct time before launch, the launch itself, and the transport phase, the experiment has no ground support available. For other microgravity platforms, such as sounding rockets or for a satellite mission, the system needs to sustain itself completely autonomously after launch. Depending on the launcher, up to launch or at least up to a certain point, the ground support equipment (GSE) is used to provide the payload with power, data and cooling abilities for the thermal control system (TCS). The GSE needs to be designed depending on the needs of the payload. For the actual supply or communication with the payload via the GSE, an umbilical and feedthrough concept is required to make critical components accessible if needed, prior to launch. As a lessons learned from the MAIUS-A payload, and to comply with the requirements in MAIUS-B, the umbilical and feedthrough concept was adapted. The new concepts as designed, implemented and tested throughout this thesis (see section 5.7.3), are providing the scientific payload MAIUS-B with the needed power, data, and accessibility for active cooling.

With a multitude of high electrical power components, a TCS concept is an essential part of all payloads and all microgravity platforms. The above mentioned miniaturization results in a dense payload design, with many components producing high heat loads within a small space on the one side, and

temperature critical components on the other side. In the presence of high internal or external heat loads, the TCS design is one of the most crucial elements of such a payload. Operation of critical components outside of their rated temperature range could cause, in a worst case, a failure of major components or even the mission goals. As a contribution to the MAIUS-B payload and an important outcome of this thesis, the necessary design developments of the overall TCS concept throughout all subsystems are shown and discussed in section 5.3 and throughout the different subsystems in chapter 5. In addition, the qualification tests (see section 5.3) of the TCS in combination with the GSE were conducted and passed as an outcome of this thesis and in preparation for the launch.

2 Scientific Background

This chapter will provide the scientific background for the main experiment of the MAIUS-B scientific payload (see chapter 5), and for the investigation of the leakage rate of CF flanges under static loads (see chapter 7). In the first section, the methods and techniques of trapping and cooling atoms towards a dual-species BEC with ^{87}Rb and ^{41}K are discussed. These methods are followed by a description of a matter wave interferometer with ultracold atoms, and the use for testing the UFF. All these concepts, methods and techniques are discussed briefly to provide an overview. For more detailed information in these fields, please refer to the respective work, such as [Alo22; Her12; Ket99; Pie21; Rud10; Sei14]. The actual optimization and implementation of the different steps towards the dual-species experiment for the missions MAIUS-2/3 (MAIUS-B), are not within the scope of this thesis, but are presented in thesis [Pie21].

The second part of this chapter focuses on UHV systems as a key technology for the MAIUS missions. While the scopes in this thesis are on UHV systems and technologies in space, such as the MAIUS UHV system in chapters 5 and 6, the upcoming section provides the necessary scientific background. The principles for the different pumping concepts used within the MAIUS missions are presented, as well as a general definition of a UHV system. In the following sections, the CF flange system and UHV materials are stated, as used in this thesis throughout the leakage rate tests on CF connections under static loads (see chapter 7). The last sections explain the basic principals of leakage detection as a key component for the later tests.

2.1 Ultracold Atoms

2.1.1 General Definition

Based on the work of Satyendra Nath Bose and Albert Einstein, the existence of BECs was proposed in 1924 [Bos24; Ein24]. It was postulated by Einstein, that cooling bosonic gases down to a temperature in the nanokelvin region (close to the absolute zero), will cause the atoms to condensate into their lowest possible quantum state. In this state, quantum effects become apparent on a macroscopic scale and only one single wave function can be used to describe the the atomic ensemble, which are all in the same state. To perform atom interferometry, the low expansion velocity of BECs is an advantage. Delta-kick collimation (DKC) is used to further lower this expansion velocity and makes it possible to perform atom interferometry on longer time scales [Amm97; Dep21].

The critical temperature (in case of a 3D harmonic trap) of a dilute gas of bosons to create a BEC is defined by [Pet02] as

$$T_\mathrm{c} \approx 3.3125 \frac{\hbar^2 n^{2/3}}{m k_\mathrm{B}}\,, \tag{2.1}$$

where n is the particle density, m the mass per boson, $\hbar$ the reduced Planck constant and k_B the Boltzmann constant. T_c is only dependent on the atom species and the particle density n. The particle density is strongly dependent on the configuration of the experiment, such as the trap geometry, the particle number and the temperature. Because of that, T_c is only valid for a specific experiment configuration and cannot be calculated by literature values [Gro16a]. For the MAIUS-B apparatus it was possible to reduce the temperature of both ensembles to a few hundred nanokelvin [Pie21]. In the following sections, the main techniques for cooling and trapping towards a dual-species BEC are addressed and discussed.

2.1.2 Atom Species ^{87}Rb and ^{41}K

For the experiments of the MAIUS-2/3 missions, ^{87}Rb and ^{41}K were chosen as the atomic species. During the MAIUS-1 mission, the MAIUS team was able to gain advanced knowledge and expertise in working with the ^{87}Rb isotope. The lessons learned from the MAIUS-1 mission are included as part of the technology and knowledge transfer in the preparation of the MAIUS-2/3 missions. Since the cooling frequencies of 780 nm (^{87}Rb) and 767 nm (^{41}K) are so close, the same optics can be used. Furthermore, a dual-species BEC with the ^{87}Rb and ^{41}K isotopes is generally possible, with controllable number ratios [Bur18]. Due to their high distinction in the proton/neutron number, the likelihood of a violations of the weak equivalence principle (WEP) is assumed to be high, as stated in [Pie21]. Therefore, these two atom species were chosen throughout the MAIUS missions and within the QUANTUS projects, as a predecessor for future satellite missions.

For a better understanding of the different cooling and trapping techniques used to generate a mixture of BECs with ^{87}Rb and ^{41}K, the level structure for the D2 transition of both isotopes are shown in figure 2.1. The level structure of ^{41}K (figure 2.1a) and the structure of ^{87}Rb (figure 2.1b), with their respective wavelengths, is shown in the D2 line used during the cooling process. The cooling (red) and repumping (blue) transitions are illustrated, which will be further explained in the following sections. As shown in figures 2.1a and 2.1b, both isotopes have two ground hyperfine states (F=1,2) and four excited hyperfine states (F'=0,1,2,3). In the presence of an external static magnetic field, hyperfine states F are split into 2F+1 different sublevels due to the Zeeman effect. This leads to the following sublevels: F'=1,m_F=-1,0,1; F'=2,m_F=-2,-1,0,1,2; F'=3,m_F=-3,-2,-1,0,1,2,3.

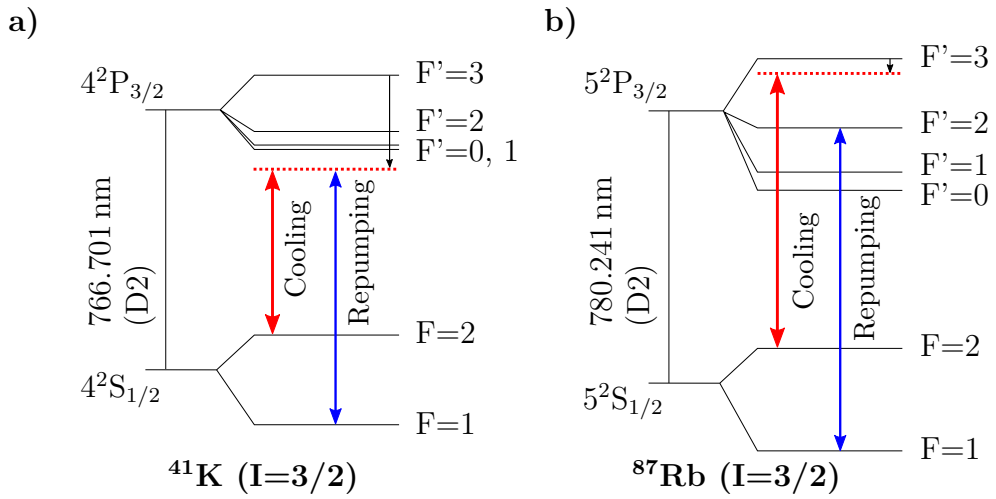

Figure 2.1: Level structure of D2 transitions of ^{41}K a) and ^{87}Rb b) [Ste19; Tie19]. The different transitions involved in the cooling (red) and repumping (blue) process are indicated. The red dotted lines indicate the red-detuning of the cooling/repumping lasers with respect to the atomic state.

2.1.3 Cooling Procedures for a Dual-Species BEC

To create a dual-species BEC, a multiple step process is needed to cool the ^{87}Rb and ^{41}K atoms down to the desired temperature T_c as stated in section 2.1.1. These techniques are explained briefly in the next sections.

2.1.3.1 Magneto-Optical Trap

One widely used procedure for cooling and trapping the atoms is a magneto-optical trap (MOT). For this method, the atoms are cooled via Doppler cooling [Phi98] to a temperature of a few hundred microkelvin as shown in figure 2.2 [Sah19]. The light fields used are counter-propagating, red-detuned laser beams, with opposite circular polarizations employed along the respective axes. In contrast to conventional laser cooling which is only velocity selective, a magnetic quadrupole field is applied. Due to the Zeeman effect, this gradient leads to a spatial dependence of the atomic resonance frequency which can be used for spatial trapping. These quadrupole fields are usually

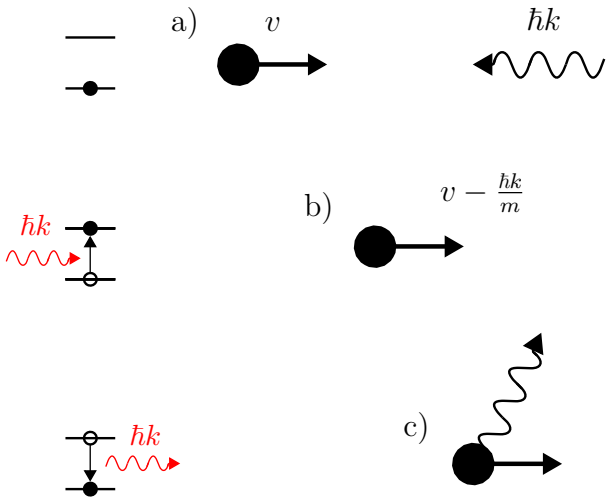

Figure 2.2: a) The atom with velocity v encounters a photon with the momentum $\hbar k = h/\lambda$. b) By absorbing the photon, the atom is slowed down by $\hbar k/m$. This is based on the Doppler-effect. Therefore the light is red-detuned, so that when the atom is moving towards the photon, the Doppler shift causes the frequency of the atom to be shifted to resonance. This increases the likelihood of an absorption of the photon, compared to an atom moving in a different direction. As shown on the left side, the atom gets transferred to a higher state if the laser wavelength equals the transition frequency of the hyperfine structure. c) After a time, the photon is spontaneously emitted in a random direction which transitions the atom back into its initial state. After many of these processes with spontaneous emission in random directions the atom is, on average, slowed down. When completed, the cooling cycle can start again (adapted from [Phi98]).

generated by Anti-Helmholtz coils. The MOT can be realized in three dimensions by adding pairs of counter-propagating laser beams to shine light from all directions [Gro16a; Sah19]. By using an atom chip as in MAIUS-2/3, a Mirror-MOT with different geometries can be realized as described in [Rei99].

For the cooling cycle, the D2 transition (as shown in figure 2.1, in red) from the F=2 $\rightarrow$ F'=3, is used at 780.241 nm and 766.701 nm for ^{87}Rb and ^{41}K, respectively. When the cooling light is red-detuned by a few MHz from a closed atomic transition (red dotted line in figure 2.1 a,b), each absorption of a photon is always followed by a spontaneous emission back to the ground state F=2. The red-detuning is used, so that only atoms which are moving in opposite of the light field are resonant and absorbing photons. This ensures an

optimal cooling process, since the atom stays inside the cooling cycle [Sah19]. There is a non-zero probability for ^{87}Rb and a high probability for ^{41}K due to a comparably small splitting of the $P_{3/2}$-manifold that the atoms unintentionally excite into the F'=2 state [Pie21]. From this state a relaxation into the F=1 ground state is possible. This hyperfine state is dark, since the atoms in this state are not resonant to the cooling light anymore. These atoms are no longer affected by the cooling cycle. To avoid this, a second beam in resonance to the F=1 $\rightarrow$ F'=2 transition (blue line in figure 2.1) is used to optically repump the atoms back into the cooling cycle [Sah19].

In many cases, as well as for the MAIUS experiment (see chapter 5), loading of the three-dimensional MOT (3D-MOT) is assisted by a separated two dimensional (2D-MOT) with two counter-propagating cooling beams and a two-dimensional quadrupole magnetic field added by two pairs of coils in race-track configuration [Die98]. In the actual experimental chamber, a 3D-MOT has been implemented, with a retro reflective atom-chip setup used to simultaneously trap K-41 and Rb-87 [Wil04]. The two chambers are separated via a differential pumping stage (DPS) to allow for a low UHV pressure in the 3D-MOT chamber and allowing for higher UHV level in the 2D-MOT chamber. The 2D-MOT is a preparation to load the 3D-MOT, which aims for the highest possible atomic flux. The atoms are able to pass through the DPS into the 3D-MOT by a small hole in the middle of the DPS (further explained in section 6.2.3). In another step, sub-Doppler cooling is applied to further cool down the atoms towards a BEC, which can be found in detail in the dedicated literature, such as [Lan11].

2.1.3.2 Magnetic Trapping, Evaporative and Sympathetic Cooling

The steps used to generate quantum mixtures of ^{87}Rb and ^{41}K, deviate from the steps used for a single species BEC due to mixture effects. Details of the technical implementation are found in [Bur18; Pie21] and are not in the scope of this thesis. This section aims to give a brief overview of these techniques.

After loading the atoms into the 3D-MOT, they are trapped by a magnetic field generated by a z-shaped structure on the atom chip in combination with a homogeneous bias field in the y-direction. An additional negative x-field would realize an Ioffe-Pritchard-Configuration, which means a harmonic trap ideal for the cooling towards the BEC. In the final step of the BEC generation of ^{87}Rb in combination with ^{41}K, the commonly used approach of evaporative cooling by radio-frequency (RF) cannot be applied in atom chip experiments [Her13; Sei14], as pointed out in [Pie21]. To further reduce the kinetic energy of the ensembles trapped in a magnetic potential, the ^{87}Rb ensemble is evaporated using a microwave and the ^{41}K ensemble is sympathetically cooled. Throughout the sympathetic cooling, the temperature of the ^{41}K atoms are decreased by interspecies elastic collisions with the slower ^{87}Rb atoms acting as a buffer gas. The ^{41}K atoms are sympathetically cooled, while their atom number is kept nearly constant [Bur18]. The microwave evaporation removes the most energetic ^{87}Rb atoms by using the microwave transition at 6.8 GHz between the F=2 and F=1 state. The atoms in F=1 leave the magnetic trap, and the residual atoms in F=2 rethermalize to a lower temperature. Figure 2.3 was produced within this thesis, to show a simplified microwave evaporation scheme, where only F=2, m_F=2 is a trapping state, with the trapped atoms indicated in red.

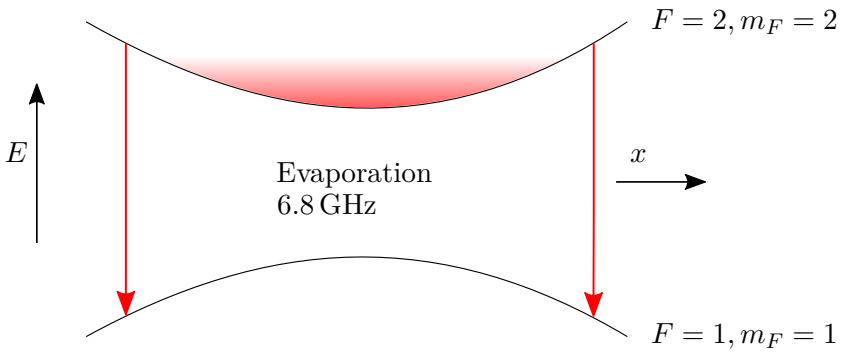

Figure 2.3: Simplified microwave evaporation scheme, where only F=2, m_F=2 is a trapping state. The atoms are indicated in red and the microwave transition is shown by the red arrows.

This procedure is repeated continuously by ramping down the frequency of the microwave. If $T < T_c$, the ensemble undergoes a phase transition and a dual-species BEC of ^{87}Rb and ^{41}K is formed. Detailed information about the procedure of microwave evaporation and sympathetic cooling with both species, is presented for the preparation of the MAIUS-2/3 missions in [Pie21].

2.1.4 Atom Interferometry

Atom interferometry is one of the most promising techniques for ultra-precise and accurate measurements for applications, such as inertial sensing, future detection of gravitational waves, geodesic applications (absolute gravity field mapping), magnetic field detection, or gradiometer (gravity gradients) [Alo22]. For future spaceborne fundamental physics experiments, for example the WEP test [Agu14; Tin13], two BECs of two atom species, such as ^{87}Rb and ^{41}K, can be used as test masses. A major advantage for an atom interferometry with ultracold atoms, is the fact that it is drift free and absolute calibrated, since the atomic properties are not changing. Adding a second species for atom interferometry, such as planned within the MAIUS-2/3 missions [Pie21], paves the way towards future experiments, but also adds a high level of complexity. In this section, the principles of matter wave interferometry will be discussed.

Matter wave interferometry is widely conducted in a configuration similar to an optical Mach-Zehnder interferometer. As used in MAIUS-2/3, a schematic overview of a general process for matter wave interferometry (using Raman double diffraction) can be seen in figure 2.4. It is achieved with a sequence of three Raman double diffraction pulses ($\pi/2$ - π - $\pi/2$), starting with a beam splitter $\pi/2$-pulse. This transfers the atoms from their initially prepared state $|\mathrm{F{=}2,p{=}0}\rangle$ (green lines in figure 2.4) symmetrically into the states $|\mathrm{F{=}1,p{=}}\pm 2\hbar K\rangle$ (red lines in figure 2.4) [Lév09]. The two wavepackets drift apart for an interrogation time T, until each wavepacket will be redirected by a π-pulse. After another free evolution time T, a second $\pi/2$-pulse causes the

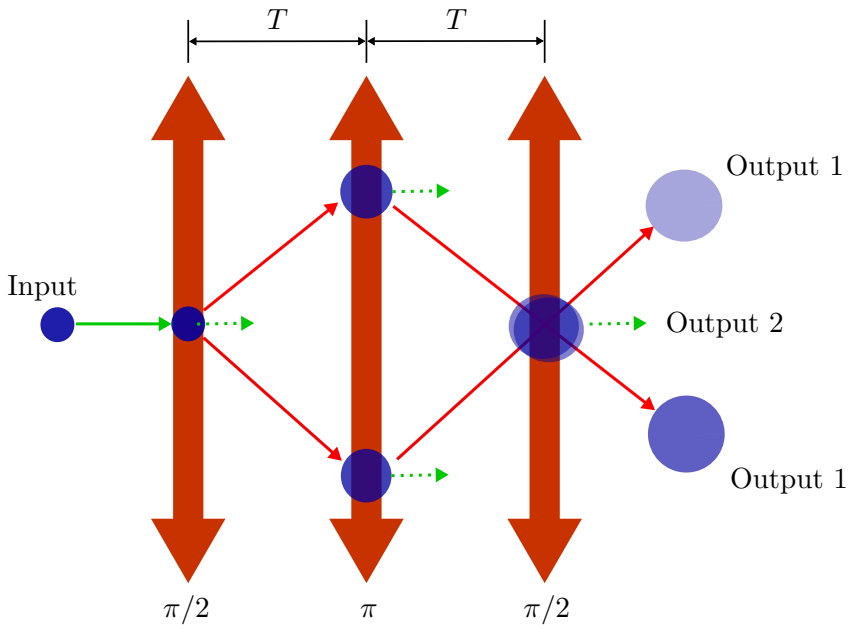

Figure 2.4: The Mach-Zehnder atom interferometer is schematically shown above. T is the interrogation time between two Raman pulses with $2T$ as the interferometry time. This three-Raman-pulse atom interferometer ($\pi/2$ - π - $\pi/2$) results in two output ports. Their population distribution depends on the relative phase in one of the two interferometer paths. The dotted arrows indicate an imperfect beam splitter or mirror for Raman double diffraction. These non-diffracted atoms can be blown away, because they have another internal energy state than the diffracted atoms. The red and green lines indicate the two states $|\mathrm{F{=}1,p{=}\pm 2\hbar k}\rangle$ and $|\mathrm{F{=}2,p{=}0}\rangle$, respectively [Lév09].

wavepackets to recombine and interfere [Bar13]. External accelerations and rotations can be measured based on the phase difference they cause in the two interferometer paths. This phase difference can be determined by detecting the relative proportion of atoms in the outputs (see figure 2.4) after the final beam splitter.

Bragg double diffraction [Ahl16] and Raman double diffraction [Lév09] are two possible approaches for the laser beam splitter. From a technical point of view, Raman double diffraction offers certain advantages, compared to Bragg double diffraction. The use of Raman double diffraction allows to track and compensate imperfections of the beam splitter, which can cause

non-diffracted atoms as indicated by the dotted arrow in figure 2.4 [Lév09]. These non-diffracted atoms can be blown away between the Raman laser pulses. This simplifies the later analysis of the interferometer outputs, since the non-diffracted atoms do not enter the detection zone. Additionally, by using a Raman beam splitter, the distinction of the different output ports can be realized by state selective detection [Her12].

The sensitivity of an interferometer is proportional to the square of the time T^2 an atom spends in the interferometer [Bar13; Rud10]. For atom interferometry, the atoms need to be released from the magnetic trap, which leads to an acceleration towards the bottom of the vacuum chamber in the presence of gravity. Since the vacuum chamber can only be increased to a certain level, spaceborne experiments, such as sounding rockets, the ISS or satellites, are desirable platforms for current and future experiments. Performing such an experiment on a microgravity platform is a challenging task and several techniques are still under investigation as stated in [Pie21]. One of the long-term goals of these experiments is to test the WEP or UFF, which is one of the assumptions of Einstein's general relativity [Ein07]. Einstein stated that, in absence of disturbances such as air friction, two bodies with the masses m_1 and m_2 are accelerated equally by a gravitational field, regardless of their mass or internal structure [Her12]. The difference between the acceleration of the two masses can be defined by the Eötvös factor

$$\nu = 2\frac{a_{\mathrm{m1}} - a_{\mathrm{m2}}}{a_{\mathrm{m1}} + a_{\mathrm{m2}}}\,, \tag{2.2}$$

with a_{m1} and a_{m2} being the accelerations of m_1 and m_2, respectively [Bar13]. With the experiments of the MICROSCOPE (Micro-Satellite à traînée Compensée pour l'Observation du Principe d'Equivalence) mission [Tou17], this factor was already measured to be smaller than 1.3×10^{-14}. For future satellite missions, as proposed in STE-QUEST [Agu14], an even higher accuracy of 10^{-15} is proposed. The sounding rocket missions MAIUS-2/3, with its scientific payload MAIUS-B as presented throughout this thesis in chapters 5 and 6, are important milestones and pave the way for future missions.

2.2 Ultra-High Vacuum

Throughout this thesis, the main focus is on UHV systems for space missions. The scientific background for the later presented UHV system (chapter 6) of the MAIUS-2/3 scientific payload (chapter 5) and the investigations of the leakage rate of CF connections under mechanical loads (7) are discussed in the following sections.

2.2.1 General Definitions & Vaccum Levels

In this section, the general definition and theoretical background of vacuum systems and different vacuum levels will be presented. If the pressure of a gas inside a chamber/vessel is below the outside pressure, or the pressure of a gas is lower than 300 hPa, then the state of this gas is defined by [DIN90] as vacuum. 300 hPa is considered by this definition as the lowest atmospheric pressure occurring on the earths surface. Whereas the pressure p is defined as $p{=}F/A$, where the force F is applied equally and vertically to an area A. Throughout this thesis, hPa is used as the pressure unit, which correlates to other commonly used units by $1\,\mathrm{hPa}{=}1\,\mathrm{mbar}{=}10^2\,\mathrm{Pa}{=}10^2\,\mathrm{N/m^2}$. In case of a non-pure gas, the pressure of a gas mixture is defined by Dalton's law as the sum of the partial pressure of each component, which results in a total pressure [Pfe13b].

For a better understanding of vacuum systems, we can use the ideal gas law as stated in [Jou12]

$$pV = mR_\mathrm{s}\vartheta\,, \tag{2.3}$$

where p is the pressure, V the volume, m the mass, R_s the specific gas constant of the gas or mixture and ϑ the temperature. The Boltzmann constant $k_\mathrm{B}{=}1.380\,649 \times 10^{-23}\,\mathrm{J\,K^{-1}}$ and the number of particles N equation 2.3

[Jou12] can also be written as

$$pV = Nk_{\mathrm{B}}\vartheta\,. \tag{2.4}$$

Equations 2.3 and 2.4 show the dependencies of the pressure by the different values, such as the mass or the number of particles, as a first approximation within its assumptions and limitations. As derived from [DIN90], the

Table 2.1: Vacuum levels with their respective pressure and particle density [DIN90].

Pressure Level	Pressure in hPa	Particles per cm^3
Atmospheric Pressure	1 013.25	2.7×10^{19}
Low Vacuum (LV)	300 - 1	10^{19} - 10^{16}
Medium Vacuum (MV)	1 - 10^{-3}	10^{16} - 10^{13}
High Vacuum (HV)	10^{-3} - 10^{-7}	10^{13} - 10^{9}
Ultra-High Vacuum (UHV)	10^{-7} - 10^{-12}	10^{9} - 10^{4}
Extreme-High Vacuum (XHV)	$<10^{-12}$	$<10^{4}$

different vacuum levels are defined as shown in table 2.1. The vacuum level, and thereby the pressure, correlates with the number of particles. The required pressure for the experiment of the MAIUS-2/3 missions is less than 5×10^{-10} hPa, which is in the UHV level.

2.2.1.1 Type of Flow

To define the type of flow which takes place in the different vacuum levels, the dimensionless Knudsen number characterizes the type of flows in respect to the pressure or vacuum level as shown in figure 2.5. In a tube/channel, the Knudsen number is defined by [Jou12], as the ratio between the mean free path $\bar{l}$ and the diameter d as

$$K_n = \frac{\bar{l}}{d}\,. \tag{2.5}$$

The mean free path is the average distance between particles or the distance until a particle would have another collision with the next particle. If the

Knudsen number is below 0.01, the flow type is called viscous or continuous flow, which is the case for the low vacuum regime. In this case the particles have more frequent collisions with each other than with the wall. The mean free path is significantly smaller than the dimension of the flow channel. In a medium vacuum having a Knudsen number between 0.01 and 0.5, the flow is called Knudsen flow. In this regime, the particles have collisions with each other and the wall in an equal ratio. In the case of very low pressures in the HV or UHV regime, the free mean path is much larger compared to the channel size, such that particle collisions with each other are not frequently occurring. There are still frequent collisions between the particles and the wall. This flow type has a Knudsen number above 0.5 and is called molecular flow [Jou12; Pfe13b].

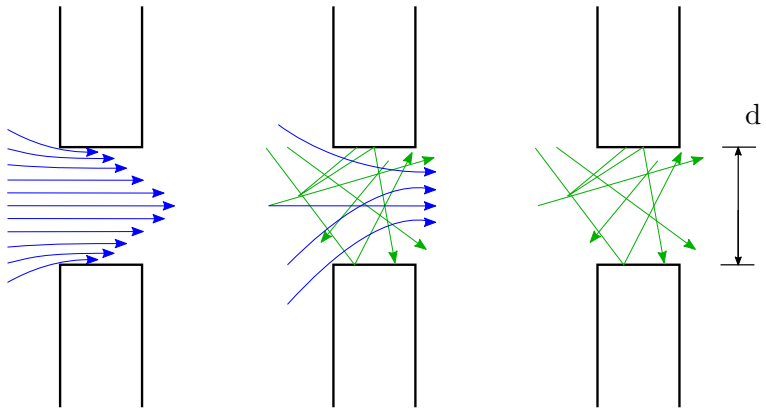

Continuous flow	**Knudsen flow**	**Molecular flow**
$K_n < 0.01$	$0.01 < K_n < 0.5$	$K_n > 0.5$
Low vacuum	Medium vacuum	High/Ultra-high vacuum

Figure 2.5: Types of flow in respect to the pressure or vacuum level. (adapted from [Pfe13b])

2.2.1.2 Reachable End Pressure

The final end pressure p_{end} of a vacuum system, is defined in [Pfe13b] as

$$p_{\mathrm{end}}(t) = \frac{Q_{\mathrm{des}}(t) + Q_{\mathrm{diff}}(t) + Q_{\mathrm{perm}} + Q_{\mathrm{leak}}(t)}{S_{\mathrm{eff}}} \,. \tag{2.6}$$

where Q_{des} is the desorption rate, Q_{diff} the diffusion rate, Q_{derm} the permeation/diffusion rate and Q_{leak} the leakage rate. All therms are divided by the effective pumping speed S_{eff} which is achieved by the vacuum pumps connected to the vacuum system (reduced by the conductive pipes). Figure 2.6 was produced throughout this thesis, to show a simplified vacuum chamber with the different terms which are influencing the end pressure.

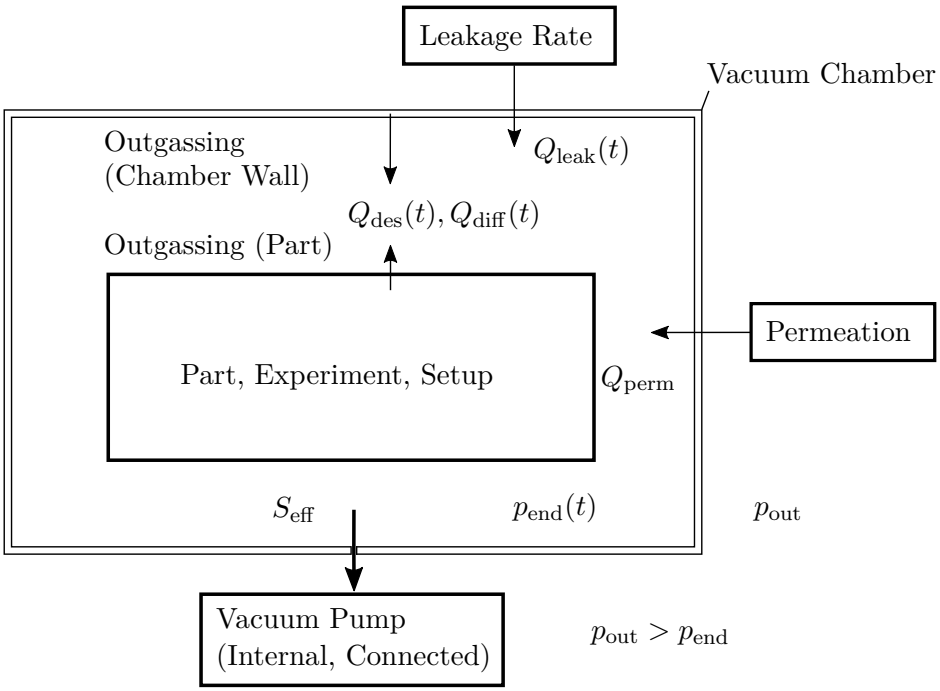

Figure 2.6: Schematic overview of a simplified vacuum system. The different terms which influence the end pressure p_{end} are shown as well as the pumping speed S_{eff}.

The different mechanisms including outgassing, leakages, and the pumping speed, are discussed and further explained in the following sections.

2.2.2 Outgassing

In this section, the focus is on outgassing of technical surfaces, such as the UHV system of the MAIUS-B payload (6.2). The mechanisms involved in the outgassing process will be explained briefly, but for more detailed theoretical background, please refer to the dedicated literature [Jou12]. As stated in equation 2.6 and in figure 2.6, outgassing influences the pressure of the vacuum system. It defines the gas flow from a material or surface into the vacuum system, and is the sum of gas released due to diffusion, desorption and permeation. High outgassing rates increase the pressure and the pump down time towards the required end pressure of the vacuum system, for a fixed pump speed.

Contamination of a material or surface inside the vacuum increases these effects. Contaminants, such as waste lubricants from the production, dust or particles from the assembly, and environmental related contamination such as water vapor adsorbed on the surfaces, are typical challenges for vacuum systems [Pfe13b]. Therefore, parts with surfaces facing into the vacuum need to be cleaned and assembled in a clean environment (i.e. clean room). This reduces contamination to a minimum, as shown for the MAIUS-B vacuum system in section 6.2.1. Waste lubricants from manufacturing or dust particles are reduced by such a cleaning process. However, water vapor adsorbed on the surfaces can only be reduced by higher temperatures (back out). Condensed water vapor is pronounced adsorbed on all surfaces due to a high polarity of the water molecules and a comparatively high existence (10 g per m^3) in normal air [Pfe13b].

Under vacuum, gas molecules (mostly water) which are adsorbed or absorbed in the interior surfaces/walls of the vacuum system, are gradually desorbed into the vacuum [Pfe13b]. This desorption takes place when the kinetic energy of the particles bound on the wall, with a temperature ϑ_w, that is higher than the desorption energy E_{des} [Jou12]. For metal surfaces, the desorption rate and the gas flow into the vacuum system decrease over

time. After a certain time $t > t_0$, with t_0 typically assumed one hour, the desorption rate can be stated in a good approximation as linear by [Pfe13b] as

$$Q_{\mathrm{des}}(t) = q_{\mathrm{des}} A \frac{t_0}{t} \,. \tag{2.7}$$

where Q_{des} is the desorption rate, q_{des} the area specific desorption flow rate, A the area, t the time, and t_0 the time of measurement.

It is also possible that gas molecules bound inside the material exit the material by diffusion and in a second process desorb from the surface. Diffusion is especially dominant for polymers and the time dependency can be approximated from [Pfe13b] as

$$Q_{\mathrm{diff}}(t) = q_{\mathrm{diff}} A \sqrt{\frac{t_0}{t}} \,, \tag{2.8}$$

where Q_{diff} is the diffusion rate and q_{diff} the area specific diffusion flow rate.

Permeation is a combination of mechanisms including diffusion and desorption. Adsorbed molecules on the outside of the wall are diffusing through the material and desorb on the inner wall surface into the vacuum system. The flow of gas molecules through the wall, as shown in figure 2.6, depends on the pressure difference from the outside (p_{out}) to the vacuum/pressure (p_{end}) inside the chamber. According to [Jou12], the gas flow by permeation is three orders of magnitude lower than the diffusion. This applies to small stainless steel walls (wall thickness 2 mm). Therefore, the permeation for a vacuum chamber as in MAIUS-B, with a significantly higher thickness, can be neglected.

2.2.2.1 Outgassing Measurement

The outgassing rate for a certain material, or for the overall chamber including vacuum parts, highly depends on the material, the geometry, and the treatment before it was used. Although this data exists for certain materials,

for example in [Mos82], the actual outgassing rate can, for most cases, only be derived experimentally. The outgassing rate for assemblies or function groups of different materials are, in many cases, not able to be calculated by existing literature values. For experimental measurements of the outgassing rate, different methods exist as stated in [Els75]. The throughput method [War22] or the pressure-rise method [Els75] are widely used methods, amongst many others.

For the pressure-rise method, a part/material to be measured is kept at a constant pumping speed for a certain time under vacuum. Once the pump is closed off (for example by a valve), the pressure rise Δp of the now isolated vacuum system is measured for a time t. To receive sufficient results, a gauge with a low pumping rate needs to be used and the outgassing rate q can be calculated from [Els75] as

$$\frac{Q}{A} = q = \frac{\Delta p V}{t A}\,, \tag{2.9}$$

where V is the volume of the test chamber and A the area of the tested probe facing into the vacuum. If only desorption is assumed to participate in the process of outgassing, and if diffusion and permeation are neglected, $q = q_{\mathrm{des}}$ is the area of specific flow density (outgassing rate) with the unit $\mathrm{Pa\,m^3\,s^{-1}\,m^{-2}}$ ($\mathrm{Pa\,m\,s^{-1}}$).

In the throughput method [Zab33], with a given conductance C between two vacuum systems, the pressure readings of both chambers p_1 (inheriting the tested probe) and p_2 and the outgassing rate Q (not area specific), can be calculated from [Els75] as

$$qA = Q = C(p_1 - p_2)\,. \tag{2.10}$$

This equation also indicates the influence of the area A for the outgassing rate. The unit for the outgassing rate Q, which is not area specific, is $\mathrm{Pa\,m^3\,s^{-1}}$.

2.2.3 Leakage

Equation 2.6 shows that the leakage rate influences the pressure. A leakage can be internal (virtual leak) or external, but both result in a gas input/flow into the vacuum system and lead to a pressure rise. Internal or virtual leakages are due to gas trapped in small volumes with a very low conductance. This leads to a small gas flow over a longer time and effects the vacuum and pressure level. A good example for virtual leakages are threads of screws or trapped air in the thread hole, covered by the screw. With slits in the threads and sufficiently sized venting holes, virtual leakages can be avoided.

The second case for leakages is driven by an external gas input into the system. Especially for UHV systems, such as MAIUS where the required pressure is low, leakages are significant and can have a high impact. These external leakages can be caused by different effects as further discussed in chapter 6. Although structural flaws within the metal parts are possible, one can assume that these are avoided by the right choice of the materials and components.

For the connection of the different parts of the UHV systems, standard vacuum connections (such as CF flanges [VAC20a]) are widely used, with leakage rates less than $1 \times 10^{-12}\,\mathrm{Pa\,m^3\,s^{-1}}$. Indium wire is another commonly used material for sealing components, such as view ports (see section 6.2.2). An indium sealed connection has similar leakage rates as a CF connection below $1.97 \times 10^{-12}\,\mathrm{Pa\,m^3\,s^{-1}}$ [Kup13]. These connections are used due to their neglectable low leakage rate in UHV systems and the vacuum system is considered to be ultra-high vacuum-tight.

For spaceborne experiments, external mechanical loads have a significant impact on CF connections. External mechanical loads, as presented in section 6.3 or in former projects [Gro16a], indicate a high effect on the pressure. This is also stated in equation 2.6, where a rise in the leakage rate is proportional to a higher pressure in the system. A theoretical quantification of the leakage rate of CF connections in the presence of mechanical loads is almost impos-

sible due to the highly dynamic mechanical behavior of a complex system. However, the leakage rate affected by external loads can be determined experimentally. Although UHV systems with CF connections are widely used for space missions, reliable experimental data under mechanical does not exist. As such, this thesis aims to fill this lack of experimental data and investigate the influence of external loads on CF connections as presented in chapter 7.

2.2.4 Flange Systems

In this section, the CF connection will be presented and the sealing principle will be explained. A general overview of commonly used materials for UHV systems is given, with a focus on the ones used in CF flanges.

2.2.4.1 CF

CF connections are commonly used for vacuum systems for ground and space-borne experiments. With very low leakage rates of less than $1 \times 10^{-12}\,\mathrm{Pa\,m^3\,s^{-1}}$ and bake out temperatures up to 450 °C (723.15 K) [VAC20a], these flange systems are suitable for UHV systems up to 1×10^{-12} hPa. A wide range of parts are available as commerial off-the-shelf (COTS) components and can be immediately integrated, which is a big advantage. Defined by ISO/TS 3669-2 [ISO07], CF connections are available for nominal diameters from DN10 to DN400.

Since the CF connections play a major role within this thesis and in the later experimental investigation on the leakage rate under mechanical loads (see chapter 7), a CAD model in figure 2.7 was produced within this thesis (according to ISO/TS 3669-2 [ISO07]) to further explain the basic CF sealing principle. The sealing is done by a pair of two symmetrical knife-edges on each flange and a flat copper gasket. For the gasket, OFHC copper is generally used due to its low outgassing rate and its high bake out temperature of around 300 °C [Jou12]. In addition, OFHC copper is a much softer material

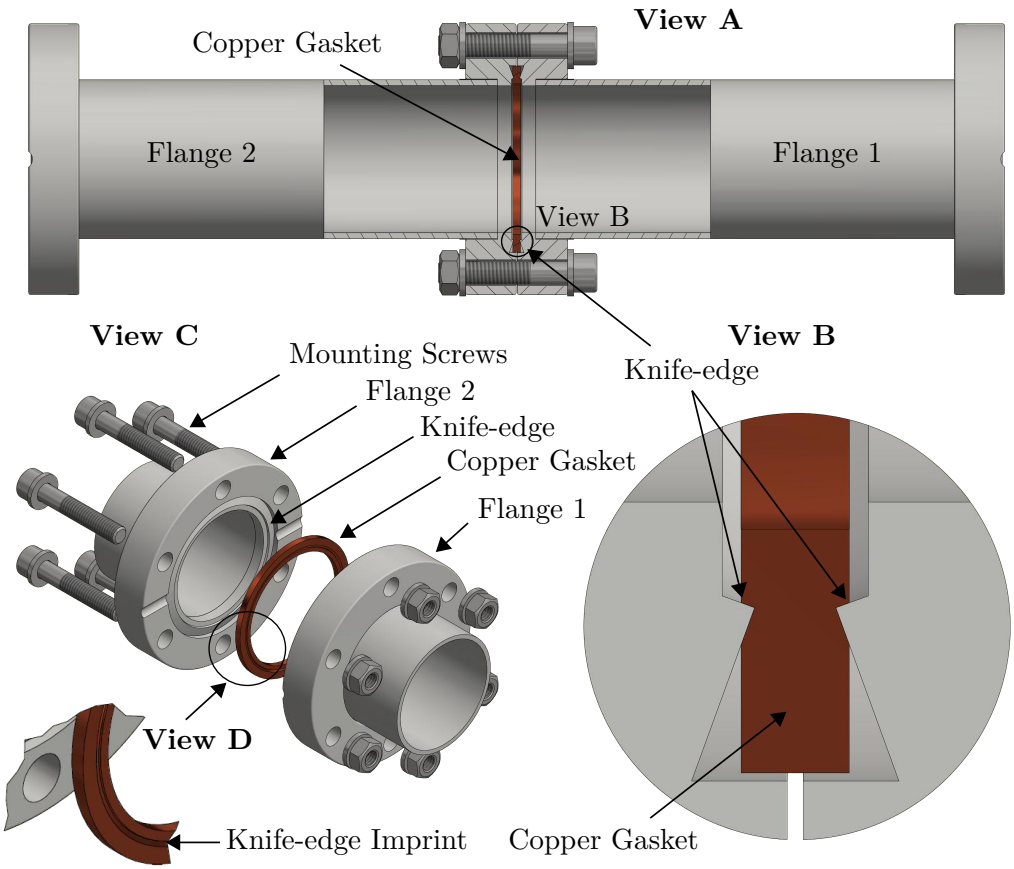

Figure 2.7: The CF sealing principle is shown for a connection between two standard CF DN40 tubes (view A) with a cutout at the connection area. View B shows a detailed view of the two knife-edges pressed into the oxygen free high conductivity (OFHC) copper gasket by the bolt pretension force of the mounting screws. In view C, the schematic explosion view of the CF flange connection is shown with all parts included. The knife-edge imprinted on the copper gasket after mounting the screws is shown in detailed view D.

than the materials (stainless steel, titanium) used for the flanges and the knife-edge itself. For the connection, the two flanges and their knife-edges, with the copper gasket in between, are pressed together by screws, and radially orientated around the flange (see view C in figure 2.7). By the bolt pretension force of the screws, the knife-edge of both flanges is pressed into the softer copper gasket from both sides (see view B and D). Due to this force, and the combination of a harder flange material, and softer gasket materials the

copper adjusts to the microscopic surface structure of the knife-edge and fills the small surface irregularities and defects [Pfe13b]. This enables the above mentioned UHV-tight connection.

2.2.4.2 UHV Materials

The material used within a vacuum system, and especially for a UHV system, depends on the pressure requirements of the experiment or application. Several materials, such as ceramics, crystals or glass, are used for certain applications, but will not be further explained in this section. The focus is on common metal based materials, such as stainless steel, aluminum and titanium, in respect to the requirements later discussed in the following chapters.

In sections 3.2 and 6.1, the requirements and the materials further used throughout this thesis are stated and will be discussed. Stainless steel is a widely used standard material for vacuum components, because of its strength, corrosion resistance, machinability and availability. Standard COTS vacuum components are made of several types of stainless steel with different characteristics as shown in data sheet [VAC20b]. Stainless steel 304 (1.4301), 316L (1.4404) or 316LN-ESR (1.4429-ESU) are available for most standard UHV components and stated in table 2.2.

Although many stainless steel components are available, certain requirements, such as a low magnetic permeability (susceptibility) (see section 6.1), require the use of different materials. Titanium grade 5 (Ti6Al4V) is used because of its lower mass, lower magnetic permeability and higher strength compared to stainless steel. However, due to longer machinability times, the costs of titanium grade 5 parts are several times higher than for stainless steel as shown in table 2.2. Cost-efficient alternatives are components made of aluminum, such as the AluVaC® [VAC16] components from the company *Vacom*. These components are made of aluminum (similar to akuminum 6068 AW), which provides a low magnetic permeability, a lightweight design due to a lower density (factor of 3 lower than stainless steel), low outgassing rates, and

Table 2.2: Comparison the characteristics of UHV materials of stainless steel (304 (1.4301), 316L (1.4404), or 316LN-ESR (1.4429-ESU)), aluminum (6068 AW), and titanium grade 5 (Ti6Al4V). The costs are stated for one CF DN40 standard tube [VAC16; VAC20b].

Material	Ultimate Strength R_{m} in MPa	Yield Strength $R_{\mathrm{p0.2}}$ in MPa	Hardness (Brinell) H in HB	Density ρ in $\mathrm{g\,cm^{-3}}$	Magnetic Perm. μ_{r}	Costs in Euro
1.4301	500-700	≥190	≤190	7.98	1.3	81.75
1.4404	500-700	≥200	≤215	8.0	1.1	148.75
1.4429-ESU	500-800	≥280	≤250	8.0	1.005	232.05
6068 AW	270-310	252	95	2.7	1.000 02	73.78
Ti6Al4V	≥895	≥830	≤310	4.43	1.000 05	898.45

Note: AluVaC® components use aluminum similar to aluminum 6068 AW.

a sufficient strength for most applications (table 2.2). This makes aluminum a good choice for UHV systems of space applications, where mass budgets are a driving design factor. Although current missions such as MAIUS-2/3 are using stainless steel and titanium grade 5, aluminum is a promising material for future UHV systems for space missions and is therefore of high interest. Nevertheless, further investigations and tests are needed to prove the usability in spaceborne experiments in the presence of external loads as described in section 6.3.

2.2.5 Pumping Systems

The throughput q of a gas through a system is the ratio between the amount of gas flowing over a time. The amount can be given in several ways, such as the volume or the mass. A common way is the pV-throughput which can be derived by dividing the ideal gas flow (see equation 2.3) by time. The pV-throughput in $\mathrm{Pa\,m^3\,s^{-1}}$ from [Jou12] is calculated as

$$q_{pV} = p\dot{V} = \frac{pV}{t} = \frac{mR_{\mathrm{s}}\vartheta}{t}\,. \tag{2.11}$$

For a constant temperature, the equation shows a constant volume flow which can then also be described as the throughput of a connected vacuum pump by [Jou12] as

$$q_{pV} = pS = p\frac{\mathrm{d}V}{\mathrm{d}t}\,, \tag{2.12}$$

where S is the volume flow rate or pumping speed in $\mathrm{dm^3\,s^{-1}}$=$\mathrm{L\,s^{-1}}$ and p is the inlet pressure of the vacuum pump. The pumping speed in this case is defined as the volume throughput with a certain volume flow over time as

$$S = q_V = \dot{V} = \frac{\mathrm{d}V}{\mathrm{d}t}\,. \tag{2.13}$$

Since vacuum systems are mostly connected to the pump via piping, this needs to be taken into account. A flow, through a pipe, results in a resistance W of the flow, due to the external friction between the gas molecules and the pipe/chamber wall, and internal friction between the gas molecules themselves (viscosity) [Pfe13b]. This results in a pressure difference and thereby a decrease of the pumping speed. The pressure difference is derived either by taking the flow resistance W or its reciprocal, the conductance C, into account and can be written from [Jou12] as

$$C = \frac{1}{W} = \frac{q_{pV}}{\Delta p}\,. \tag{2.14}$$

However, the conductance chances for different flow types and geometries need to be considered for their calculation. To determine the overall conductance of a system, the different geometries of the piping needs to be considered and can be brought together either in series or parallel, similarly to the resistances of an electrical circuit. For more detailed information, and the necessary equations to calculate the conductance of different geometries and flow types, please refer to the dedicated literature [Jou12; Pfe13b].

To define the effective pumping speed S_{eff}, the pressure at a certain point of the vacuum system p_{vac}, and the pressure at the pump outlet p_{pump}, can be

considered. They result in a constant pV-throughput in

$$q_{pV} = p_{\text{vac}}\dot{V}_{\text{vac}} = p_{\text{pump}}\dot{V}_{\text{pump}}\,, \tag{2.15}$$

which gives an effective pumping speed

$$S_{\text{eff}} = \frac{p_{\text{pump}}}{p_{\text{vac}}}S < S\,. \tag{2.16}$$

As an example, one could assume a vessel which is pumped down by a pump with a constant pumping speed. If p_{vac} is the inlet of the vessel, and p_{pump} the outlet of the pump, and the pipe in between has a conductance C, the effective pumping speed of the vessel can be calculated as

$$S_{\text{eff}} = \frac{S}{1+\frac{S}{C}}\,, \tag{2.17}$$

with

$$C = \frac{q_{pV}}{p_{\text{vac}} - p_{\text{pump}}} = \frac{p_{\text{pump}}S}{p_{\text{vac}} - p_{\text{pump}}} = \frac{p_{\text{vac}}S_{\text{eff}}}{p_{\text{vac}} - p_{\text{pump}}}\,. \tag{2.18}$$

There are a multitude of different pumps and concepts (see [Jou12; Pfe13b]), but in the next sections, only the roughening pump, ion getter pump (IGP), and titanium sublimation pump (TSP) will be discussed, as they are used in the later chapters.

2.2.5.1 Roughening Pump

A roughening pump is used to initially evacuate a vacuum system from atmospheric pressure down to a pressure region (for example HV or UHV), where other pumps can maintain, or even lower, the vacuum level further. Since all vacuum pumps have their efficient working pressure range, certain pumps are used for low or medium vacuum, while other pumps, such as the later discussed IGP or TSP, are used in the UHV region.

A common concept for a roughening pump is a combination of a backing pump (e.g. a rotary vane or diaphragm pump) combined with a turbopump [Pfe13b]. In the beginning, the backing pump runs until it reaches the necessary fore-vacuum for the turbopump to start accelerating up to its nominal speed. From that point on, the turbopump continues to pump down the system, with a lowest possible pressure range of around 10^{-10} hPa [Pfe13b]. Once the roughening pump has reached this pressure range, other UHV pumps such as an IGP or TSP can be used to maintain and lower the pressure. Roughening pumps are in many cases used during the initiation process of the vacuum evacuation and the bake out of the vacuum system. They can be detached afterwards and do not need to be considered during space missions. This makes a roughening pump a very useful device for the preparation of UHV systems of spaceborne experiments, as the mostly bulky and heavy backing pump and turbopump are not part of the payload.

2.2.5.2 Ion Getter Pump

IGPs are used for vacuum systems in the UHV region, because of their ability to create and maintain a pressure down to 10^{-12} hPa. However, the IGP requires a roughening pump (e.g. turbopump) as discussed above, since it is unable to be started at atmospheric pressure [Mac20]. It is able to pump the chemically reactive hydrogen and the chemically active (getterable) gases such as nitrogen or oxygen. As a main advantage compared to other pumps, the IGP is capable of pumping noble gases such as argon, helium or neon.

Although there are different versions of IGPs available (see [Mac20; Tec15]), this section will focus on noble diode pumps and specifically on the *VacIon Plus 20* from *Agilent* [Tec15; Tec19], which was used in MAIUS. A noble diode pump was chosen because of its ability and stability to pump noble gases at a consisting pump speed. All IGPs are based on the operational principal of a penning cell [Wel01], by the ionization of the residual gas molecules. Figure 2.8 shows the schematic structure of an IGP cell, with its anode and cathode.

The anode is a tube usually made of stainless steel. The noble diode pump has one cathode made of titanium and one made of tantalum. In contrast, both cathodes of a diode pump are made of titanium, which can lead to noble gas instability and lower performance of the pumping speed for noble gases. As shown in figure 2.8, a strong electrical potential between 3 to 7 kV is applied while permanent magnets generate a magnetic field along the center axis of the anode tube. These two fields make the electrons move on an oscillating cylindrical path inside the anode element. This increases the probability of electrons colliding with a molecule of the residual gas.

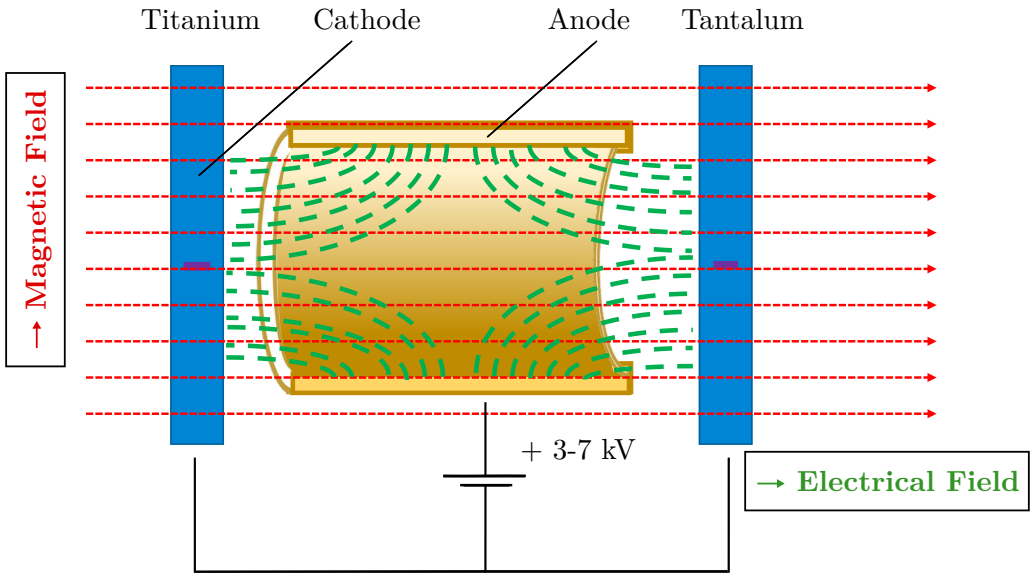

Figure 2.8: Schematic overview of a noble diode pump (such as the *VacIon Plus 20*). It also indicates the working principal of a penning cell of an IGP. (adapted from [Mac20])

Once a collision occurs, the collided molecule loses one or more electrons and transfers into a positive ion. At this point the ion will be accelerated towards one of the cathodes and removes material due to the impact, which will then build a (sputtered) atom layer on the surface of the anode. The layer of sputtered atoms from the impact at the cathode, adsorbs active gas molecules and chemically traps (getter) these background gas molecules.

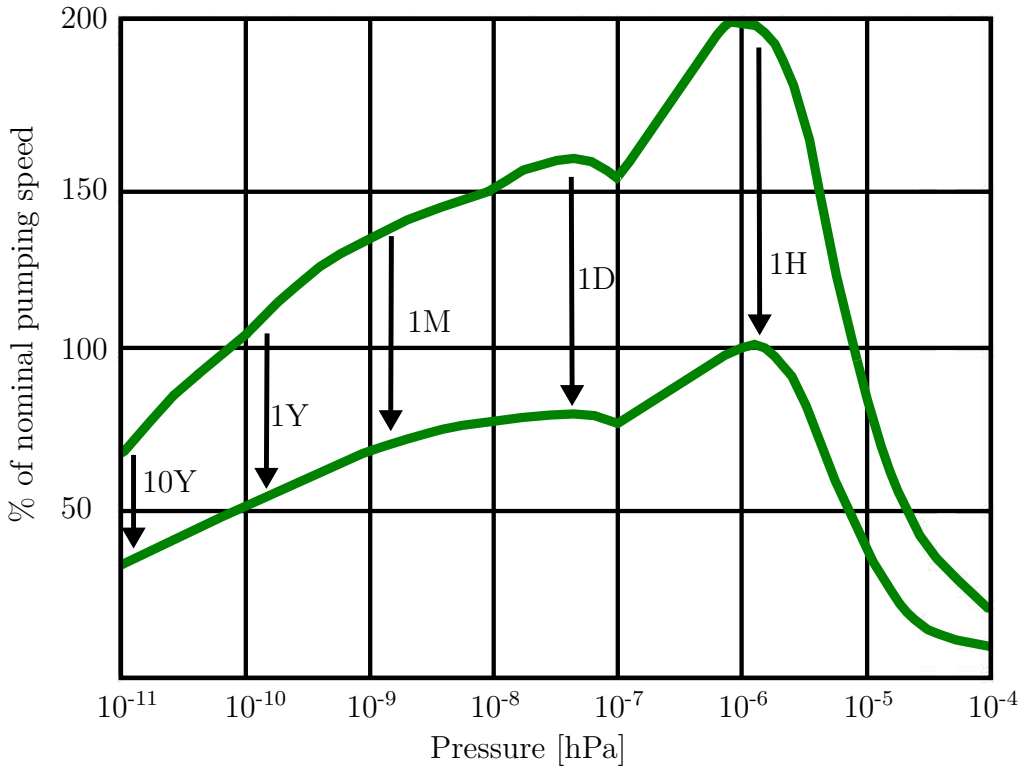

Figure 2.9: Time until saturation of the IGP (*VacIon Plus 20*) depending on the operation pressure (adapted from [Tec15]).

As mentioned above, a noble diode pump, such as the *VacIon Plus 20*, consists of one cathode made of titanium and one made of tantalum. The tantalum cathode prevents noble gas instability, which occurs for the chemically not reactive noble gases. The high-inertia crystal lattice structure of the tantalum cathode increases the probability of reflecting neutral ions and buries especially the chemically not reactive noble gases. This results in an increased pumping rate for noble gases compared to diode pumps [Mac20; Wel93].

Once the IGP is working, the permanent impact and sputtering at the cathode can erode the cathode and already bound atoms can be released.

This effect will decrease the pumping speed until an equilibrium state between ion implantation and gas re-emission is reached. At this point, the ion pump is saturated and the pumping speed is reduced to approximately half the pumping speed of an unsaturated state. Since the saturation of the IGP depends on the amount of gas inserted into the cathode, the saturation time is higher the lower the operation pressure is. This is shown in figure 2.9, which indicates after what time the IGP is saturated, depending on the pressure level [Tec15]. For the different pressure levels, the plot shows the percentage of the nominal pumping speed of the IGP, before and after saturation.

2.2.5.3 Titanium Sublimation Pump

All TSPs are equipped with one or more elements/filaments made of titanium (alloy of Molybdenum and Titanium). The TSP used for the MAIUS missions has three titanium-molybdenum filaments and is shown in detail in the later section 6.2.3. For the activation, only one filament is used at a time and the remaining filaments are spares in case one breaks. To activate the TSP, a high current (around 48 A) is applied on one filament. The titanium filament heats up to around 1 200 °C (1 473.15 K) and the sublimate titanium will then condensate on the colder outer walls of the vacuum chamber. The titanium layer pumps (getters) all gases, besides non-getterable gases such as argon and methane, by chemical absorption [Tec15]. Due to the saturation/degradation effects of the titanium layer over time, the TSP needs to be re-activated to renew the titanium layer. These effects depend on the residual pressure and the type of molecules, which define how many titanium atoms are needed to absorb the gas molecules. Figure 2.10 shows the degradation of the titanium layer over time and indicates in which intervals the TSP needs to be activated depending on its operation pressure. In the pressure range of 10^{-9} hPa for example, the maximum pumping speed for nitrogen is at 100 % after the activation. The percentage of the maximum pumping speed for nitrogen decreases over time along the line as shown in figure 2.10. If the design of the vacuum system requires a minimum of 50 % pumping speed, the plot indicates that

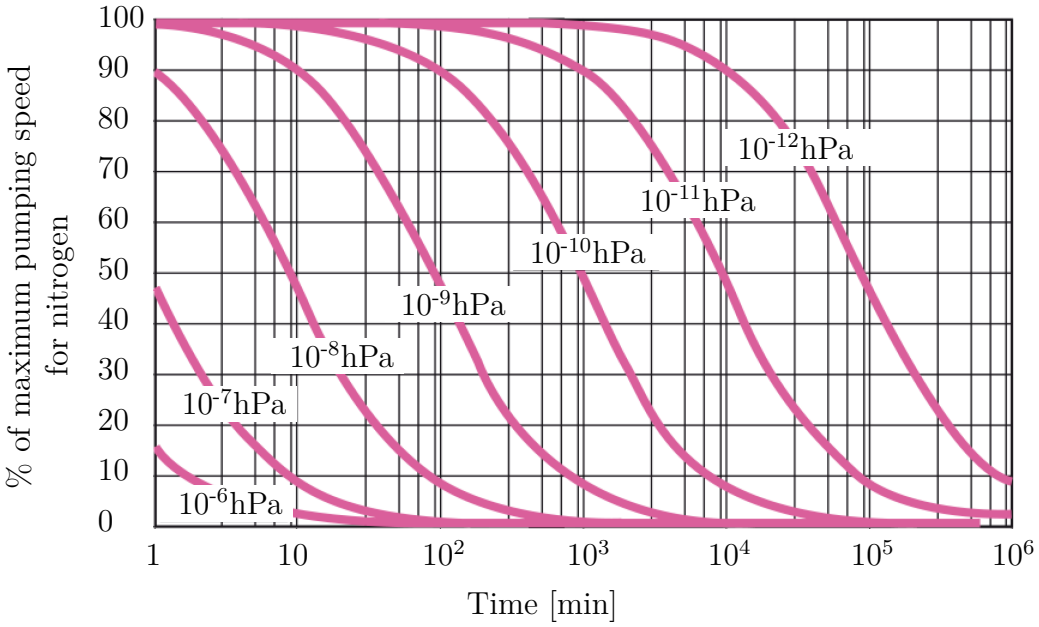

Figure 2.10: Degradation of the TSP depending on the operation pressure for nitrogen [Tec15].

every 10^2 min a re-activation of the TSP would be needed. A higher operation pressure will increase the time for a re-activation. In contrast, it is shown that for a lower pressure, the 100 % of maximum pumping speed for nitrogen is not possible anymore. After 1 min the degradation effects are dominant. It shows that the TSP is a very effective pump with low re-activation rates, especially at lower operation pressures. Additionally, a power supply is only needed during the activation. This makes a TSP a widely used component for vacuum systems on space missions.

2.2.6 Leakage Detection

For the leakage detection, the helium leak detector *ASM 340* by *Pfeiffer Vacuum* is used. Throughout the tests presented in this thesis, the most abundant tracer gas helium-4 (^{4}He) was used, with a mass of 4 u. Alternatively, this analyzer is also able to be set to detect helium-3 (^{3}He) or hydrogen [Pfe13a].

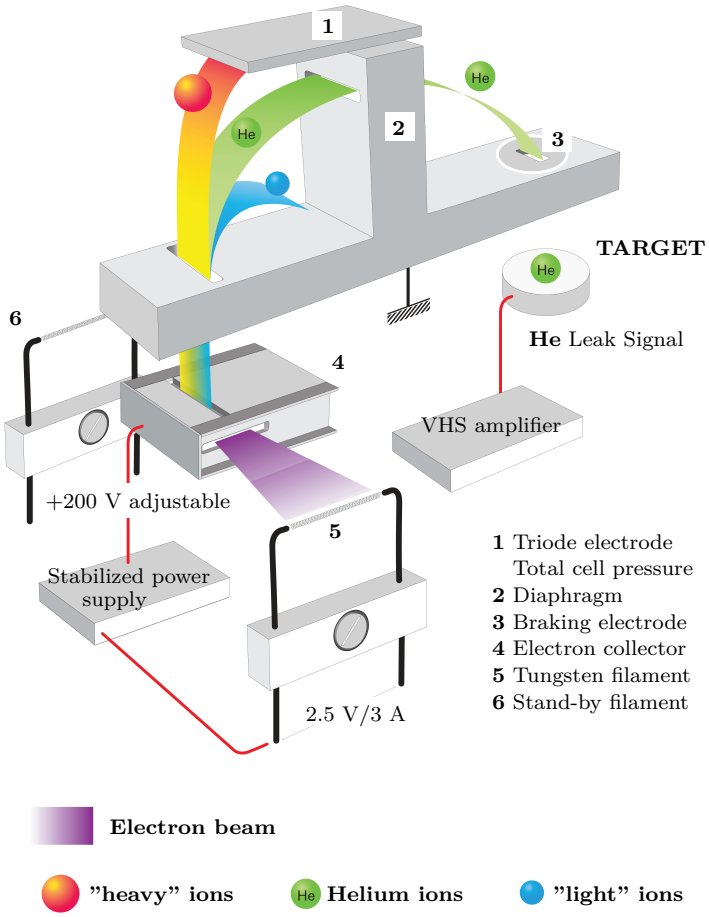

Figure 2.11: Working principle of a sector mass spectrometer [Pfe13a].

The *ASM 340* uses a magnetic sector field mass spectrometer for the leak detection and the measurement of the leakage rate. In figure 2.11, the main parts and the working principal of the mass spectrometer cell is shown. Within the first steps, the tungsten filament (figure 2.11, Pos. 5) and the ionization chamber (figure 2.11, Pos. 4) produce positively charged ions and accelerate them into a zone subjected to a magnetic field. This constant magnetic field is produced by an external permanent magnet. To get an indication of the total cell pressure, the triode electrode (figure 2.11, Pos. 1) collects the ions with a higher mass than the tracer gas. The acceleration of the ions is adjusted so that only the tracer gas is guided through a diaphragm/orifice (figure 2.11, Pos. 2) and lands at the target (figure 2.11, Pos. 3). At the target, the

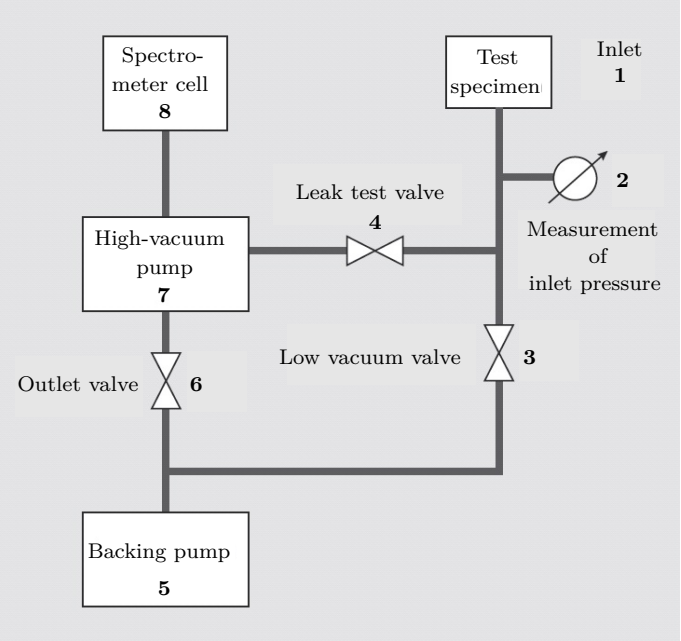

Figure 2.12: Flow chart of the Leakage detector (*Model ASM 340* by *Pfeiffer Vacuum*) [Pfe13b].

leakage rate signal is processed by the electrical current, which is converted from the ion current of the tracer gas [Pfe13a].

In figure 2.12, a general pumping and vacuum circuit of the *ASM 340* is shown. The above explained mass spectrometer cell (figure 2.12, Pos. 8) is connected to a high-vacuum turbopump (figure 2.12, Pos. 7). The roughing pump (figure 2.12, Pos. 5) can be switched on and off via the outlet valve (figure 2.12, Pos. 6) for baking of the turbopump. For the initial evacuation of the test specimen at the start of the measurement, the low vacuum valve (figure 2.12, Pos. 3) is open and the outlet valve is closed. Once the crossover pressure, which is measured at the inlet, is reached, the outlet valve is opened and the tracer gas leaking through the test specimen reaches the backing line between the turbopump and the roughing pump. At this point, the limited compression ratio of the turbopump allows the lighter tracer gas to diffuse backwards through the turbopump into the spectrometer cell where it will be detected. In this “counter flow” or “gross leak” mode, the leakage

detector is not able to reach its full sensitivity, but it prevents the analyzing cell from high contamination due to big leakages. For the measurement of small leakage rates, the detector is operated in the “direct flow” or “fine leak” mode which provides higher sensitivities. This operation mode is achieved by a lower pressure at which the low vacuum valve is closed and the leak test valve (figure 2.12, Pos. 4) is opened [Pfe13a].

3 Flight Environment and Requirements

This chapter presents the flight environment for common microgravity platforms used in space missions with ultracold atom experiments. Therefore, sounding rockets, the ISS and satellites will be discussed. Additionally, the requirements on UHV systems derived from ultracold atom experiments are explained.

As a general remark throughout this thesis and in the space community, g_0 (gravitational acceleration), is the relation commonly used for accelerations, although g_0 is not a SI-unit. While g_0 is in many cases defined as $1\,g_0 = 9.81\,\mathrm{m\,s^{-2}}$, g_0 is not a constant value and therefore only an approximation. For an accurate calculation of g_0, one would also need to take the altitude and the latitude and longitude into account. To be compliant with the given values in g_0 from the used references, the acceleration in these cases is also added in multiples of g_0, although all accelerations are generally given in the SI-unit $\mathrm{m\,s^{-2}}$.

3.1 Flight Environment

3.1.1 Sounding Rocket

Sounding rockets are used for several microgravity experiments for in-situ measurements and operation in space for several minutes. They provide a cheap, ready-to-use and unmanned microgravity platform, compared to the ISS or satellite missions [Kir18]. As part of the German Aerospace Center (DLR), the Mobile Rocket Base (MORABA) operates multiple sounding rockets and offers launches from Esrange in northern Sweden in cooperation with the Swedish Space Corporation (SSC). Although there are worldwide multiple sounding rockets, the focus in this section is on the vehicles from MORABA, as shown in figure 3.1 [MOR21].

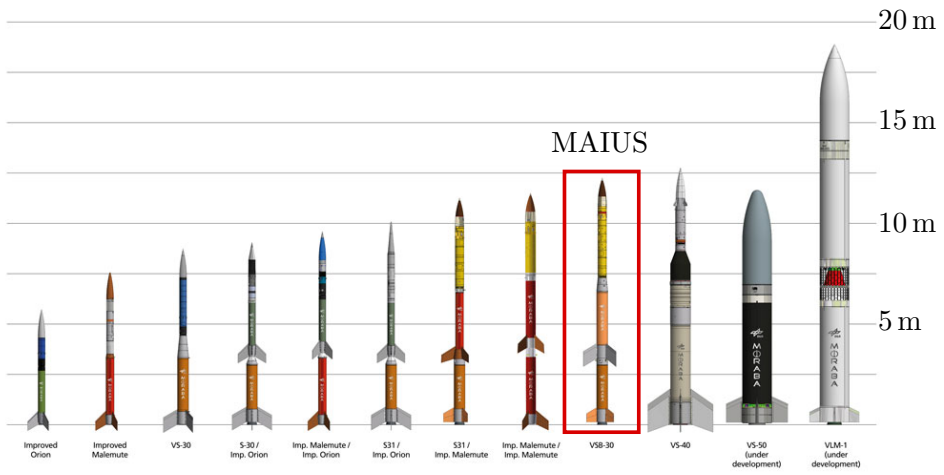

Figure 3.1: Overview of the MORABA sounding rockets vehicles [MOR21] for research under microgravity. The VSB-30 rocket as used within the MAIUS missions is highlighted in the red block.

Throughout the MAIUS-1/2/3 missions, the two-stage VSB-30 sounding rocket is used, as highlighted in the red block in figure 3.1. A typical sounding rocket mission as described in the proceedings [Kir18] is performed in a

parabolic trajectory. After the stage burns, the motors are separated and the payload is stabilized by the attitude control system. As the microgravity time begins, the experiments are performed under weightlessness, until the re-entry starts. This is followed by a parachute mode to decelerate the payload and safely land it back on the ground.

The apogee of the parabolic trajectory is at around 260 km, depending on the final mass of the scientific payload. This flight profile provides an approximate microgravity and experimental time of 300 to 360 s with a residual acceleration of $10^{-5}\,\mathrm{m\,s^{-2}}$ in all axis [Sta13]. After landing, the payload is recovered from the landing zone by a helicopter.

For a flight on a VSB-30 sounding rocket, a variation of mechanical loads occur within the different stages of the flight as described in [Gro16a]. During the ascent of the rocket, the motors are vibrating longitudinally and laterally with $17.7\,\mathrm{m\,s^{-2}_{RMS}}$ ($1.8\,\mathrm{g_{0RMS}}$) (Root-Mean-Square (RMS)) in both directions, in a frequency range of 20 Hz to 2 000 Hz [Gro16a]. Accelerations in this flight stage of $121.6\,\mathrm{m\,s^{-2}}$ ($12.4\,\mathrm{g_0}$) have been measured throughout the MAIUS-A flight, while the deceleration caused by the atmospheric friction during re-entry goes up to $147\,\mathrm{m\,s^{-2}}$ ($15\,\mathrm{g_0}$) [Gro17b]. Additional shocks from the motor ignition ($196\,\mathrm{m\,s^{-2}}$ ($20\,\mathrm{g_0}$) for 15 ms), and higher shocks for 15 ms at $491\,\mathrm{m\,s^{-2}}$ ($50\,\mathrm{g_0}$) to $981\,\mathrm{m\,s^{-2}}$ ($100\,\mathrm{g_0}$) can appear during landing. With a spin rate of 2.71 Hz and a given radius of 0.245 m, a maximum centrifugal acceleration of $71.02\,\mathrm{m\,s^{-2}}$ ($7.24\,\mathrm{g_0}$) is calculated [Gro16a].

The thermal environment of the sounding rocket depends on the time of the year the rocket is launched. During the winter, at the launch site in Kiruna, outside temperatures can drop down to −40 °C (233.15 K). These rough ambient temperatures need to be considered not only for the launch, but also for the time after the landing until recovery. While the payload is finally integrated at room temperature of 20±5 °C (293.15±5 K), the payload is transported and prepared for launch in the Skylark launch tower with a controlled temperature of 17±7 °C (290.15±7 K) [Gro16a].

Due to aerodynamic friction during the ascent of the rocket, the temperatures on the inside of the hulls segments go (depending on the hull thickness) up to around 120 °C (393.15 K). The temperature decreases within the microgravity phase because of radiation into space and convection into the payload. During re-entry, the payload (hull segments) is heated up caused by aerodynamic friction.

For atom-optical experiments, changing magnetic fields yields to potential problems on the atom interferometer and the BEC creation [Kub16]. Although thesis [Gro16a] showed minor deviations on the launch side of 3.5 mG, the magnetic fields measured during TEXUS-42 in [Ett06] shows field variations of around 750 mG (from 300 mG to -450 mG).

It is important to note that supply for power/data or cooling is only provided up to lift-off Therefore, the scientific payload and the experiment itself have to perform autonomously during flight.

3.1.2 International Space Station

The ISS is a unique microgravity platform for a wide range of experimental applications and offers a permanent microgravity environment. To install, maintain, or perform the experiments, a crew of three to six astronauts are onboard the ISS. For the supply from earth and the transport of astronauts to and from the ISS, the Soyuz launch vehicle from Roscosmos, the Cygnus cargo spacecraft by *Northrop Grumman*, and the Dragon capsule with its launcher Falcon 9 from *SpaceX*, are currently used. The ISS offers 33 International Standard Payload Racks (ISPR) inside and 18 Multi-user External Payload Sites on a truss outside of the ISS [Sab14]. For detailed information on the interfaces and the supply via the ISS, an overview can be seen in [Sab14].

The environment can be divided into the launch and flight to the ISS, and the actual operation on the ISS. For the mechanical loads during launch and flight, the load profile depends on the actual launcher which is used.

In this section, an overview on the environment for a Falcon 9 launch from *SpaceX* will serve as an example. The data is derived and presented here from the interface definition document of the company *Nanoracks* [Gre20]. The acceleration during the launch is stated to be up to $69\,\mathrm{m\,s^{-2}}$ ($7\,\mathrm{g_0}$). According to [Gre20], the random vibrations for the Falcon launcher are at $86.3\,\mathrm{m\,s^{-2}_{RMS}}$ ($8.8\,\mathrm{g_{0RMS}}$) in a frequency range of 20 Hz to 2 000 Hz.

An environmental compatibility verification as described in [Spa20] is requested from *SpaceX* prior to launch. Additionally, the payload might not be accessed and connected to any ground support equipment during certain steps of the launcher preparation which requires an autonomous power supply.

According to [Sab14], the microgravity level onboard the ISS is influenced by three principal classes of residual accelerations: quasi-steady acceleration, vibratory acceleration, and transient acceleration. The acceleration is considered quasi-steady if over a measured time for one orbit of 5 400 s at least 95 % of their power lies under 0.01 Hz [Sab14]. In the Active Rack Isolation System (ARIS), the vibrations in the frequency range of 0.01 Hz to 300 Hz are damped. Although the isolation methods have been improved, during crew activities the acceleration level can be higher by orders of magnitudes and should be taken into account. As stated in [Ceg05], the microgravity level onboard the ISS is at $1 \times 10^{-5}\,\mathrm{m\,s^{-2}}$, limited by the aerodynamic drag slowing down the station. Furthermore, the microgravity level depends on the location of the payload in respect to the station's center of mass. A gravitation gradient due to offsets of the payload from the station's center of mass, reduces the microgravity level to a maximum of $3 \times 10^{-5}\,\mathrm{m\,s^{-2}}$ [Ceg05]. During the docking maneuvers and the boost to raise the altitude of the ISS, which is necessary to compensate for altitude loses caused by the aerodynamic drag slowing down the station, a non-microgravity environment occurs.

The Environmental Control and Life Support System (ECLSS) provides an ambient pressure similar to the composition on earth with an air temperature between 17 °C (290.15 K) to 28 °C (301.15 K). In addition, EXPRESS (Expedite the Processing of Experiments to the Space

Station) racks providing water and air cooling, as well as for the possibility of crew interference [Sab14]. By orbiting the earth once every 90 min, the ISS has a constantly changing magnetic field which is important for ultracold atom experiments due to negative effects, and has to be considered within the design.

3.1.3 Satellite Missions

Satellite missions offer microgravity platforms with common operation times of five to ten years. The platforms as discussed in the sections above, are often used as technology demonstrators for future satellite missions, especially for key technologies under development. These platforms, and in particular the sounding rockets, are often used to improve the technology readiness level (TRL) of new technologies. Beside the payload costs, the launch and the in-orbit placement are cost-intensive parts of a satellite mission. As an example, one Falcon 9 launch from *SpaceX* costs around 52 million Euro, which results in an approximate cost per kilogram (into low earth orbit (LEO)) of 2300 Euro. The Falcon 9 rocket is able to carry around 22.8 t into LEO, but higher orbits would lower the capability [Spa21].

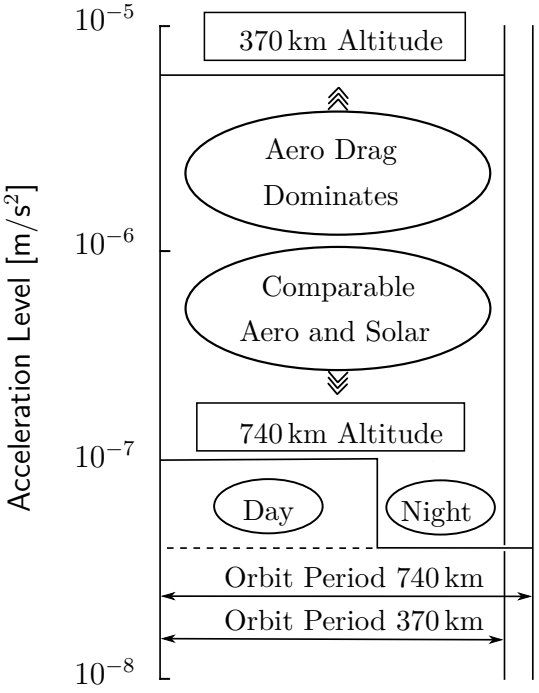

Figure 3.2: Dominating environmental effects depending on the altitude. (Adapted from [Ols81])

Since the mechanical and thermal loads on the payload are strongly dependent on the launcher, the Falcon 9 as discussed in the section above can be taken as a first assumption. Nevertheless, a multitude of launch vehicles with different load profiles are available and need to be defined based on the mission requirements.

The choice of the orbit depends on the mission goals and requirements, and will result in different residual accelerations. Figure 3.2 shows, that for a spacecraft ($60\,\mathrm{m}^2$ and $3\,270\,\mathrm{kg}$), the aerodynamic drag of the remaining earth atmosphere at 370 km dominates with a residual acceleration of $5 \times 10^{-6}\,\mathrm{m\,s^{-2}}$. In contrast to that, at around 740 km the solar pressure dominates. Additionally, figure 3.2 shows an impact of day and night time in this altitude. This results in a cycling effect over one orbit and changes the residual acceleration in the range from $1 \times 10^{-7}\,\mathrm{m\,s^{-2}}$ (day) and $3 \times 10^{-8}\,\mathrm{m\,s^{-2}}$ (night) [Ols81]. Misalignment from the center of gravity along the orbit path will reduce the microgravity level. With a well aligned detection zone of the experiment in orders of centimeter, the achievable microgravity levels can be better than $10^{-7}\,\mathrm{m\,s^{-2}}$ for an orbit altitude of 740 km [Ols81].

The thermal environment depends on the orbit and has a direct influence on the design of the TCS of the satellite. For near earth orbits, direct sunlight, the earth infrared heat flux, earth albedo, and the internal instruments need to be considered. These effects have an influence on the residual acceleration as shown in figure 3.2 for both day and night, and additionally on the TCS.

For an earth orbiting satellite, the magnetic field changes during flight, same as the gravitational gradient, due to the non-spherical shaped of the earth. For a satellite mission in the range of five to ten years, an additional environmental effect on the spacecraft is radiation. An exposure to radiation for a longer time, especially for electronic components, could lead to malfunction or a complete failure of components. Therefore, qualification of the radiation hardness and/or redundancies for key components is mandatory for a successful and reliable mission.

3.2 Requirements of Ultracold Atom Experiments on a UHV System

A main requirement for an ultracold atom experiment is the vacuum itself. While space offers vacuum conditions, the experiment needs to be reproducible and controllable, and therefore requires a vacuum system. The general requirements, such as sealing technologies, the pumping concept, assembly and production procedure, are explained in detail in section 6.1.

For experiments with ultracold atoms, a low background pressure is important to create, observe, and use BECs for atom interferometry. A higher background pressure leads to more collisions with the remaining gas atoms and lowers the performance of the experiment. The goal must be a pressure of $\leq 5 \times 10^{-10}$ hPa to ensure a high lifetime of the magnetically trapped atoms and the BEC, as stated in [Gro16a; Sei14] for MAIUS-A. To further investigate the influence of the background collisions on the trap lifetime, the pressure over lifetime was calculated and plotted in figure 3.3. The calculation is based on publication [Fol02] where the loss rate per atoms γ is stated as

$$\gamma = n_{\mathrm{bg}} \bar{v}_{\mathrm{bg}} \sigma = 3.8 \times 10^{-3} s^{-1} \frac{p_{\mathrm{bg}}}{10^{-10} hPa} \frac{\sigma}{1 nm^2} , \tag{3.1}$$

where n_{bg} is the background number of atoms, $\bar{v}_{\mathrm{bg}}$ the mean velocity of the background atoms, σ the collision cross section, and p_{bg} the background pressure. It is further assumed that the dominant background gases are hydrogen molecules at room temperature. Equation 3.1 can be combined and rearranged to p_{bg} as

$$p_{\mathrm{bg}} = \gamma \frac{10^7}{3.8 s^{-1}} \frac{1 nm^2}{\sigma} , \tag{3.2}$$

from which the background pressure can be calculated as a function of the lifetime. According to [Bal99], the collision cross section σ for Rb-H_2 collisions is 295 Å and for K-H_2 in the same range at 286 Å ($1\,\mathrm{nm}^2$=$100\,\mathrm{Å}^2$). There is a similar progression for both curves in figure 3.3. The green dashed line indicates the above mentioned literature value of 5×10^{-10} hPa from [Gro16a], as

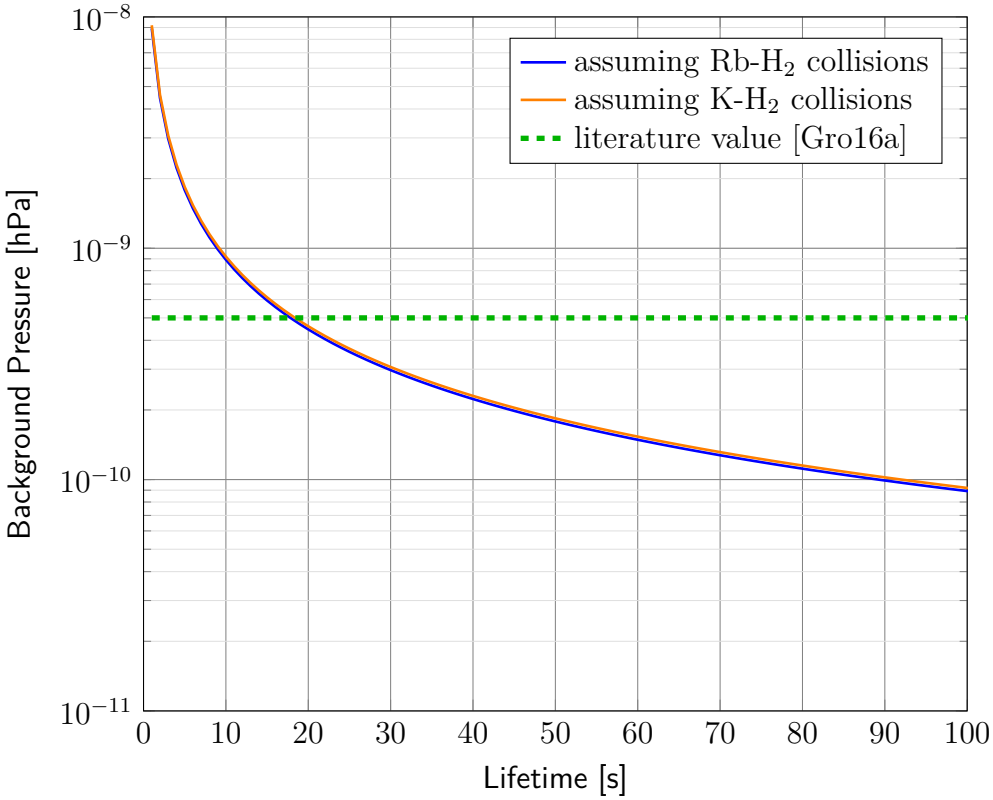

Figure 3.3: The plot shows the calculated background pressure over the trap lifetime of the atoms. The blue line assumes collisions of Rb-H_2 and the orange line of K-H_2 as the H_2 atoms are dominating in the remaining background gas. The green dashed line indicates the literature value from [Gro16a] of 5×10^{-10} hPa.

a comparison. The calculation shows that this value fits for atom interferometry times ($2T$) (see section 2.1.4) of a few seconds with aimed trap lifetimes of around 20 s. This is a reasonable assumption for an experiment sequence including the preparations steps of the BEC. To ensure a low loss rate and a high atom number during the experiment, the goal for a UHV system for ultracold atom experiments should remain as mentioned at $\leq 5 \times 10^{-10}$ hPa. A pressure level in the region of 10^{-11} hPa is advisable to ensure lower atom losses and better performance of the experiment. It is important to note that the results presented in figure 3.3 should only be taken as a first reference point, but is not a substitute for the actual tests of the lifetime on the experiment.

From a mechanical and thermal point of view, the UHV system needs to withstand the loads depending on the microgravity platform as discussed in the section 3.1. A qualification process for the system is mandatory to show the performance under mechanical loads. This process points out possible design adjustments on the vacuum system to maintain the required pressure.

Another requirement is the accessibility for laser light, as well as for optical instruments and the optical detection systems. Optical viewports are a fundamental design feature for ultracold atom experiments. Additionally, an atom source (see section 6.2.3) for the species used within the experiment, such as ^{41}K and ^{87}Rb for MAIUS, are required.

As discussed in section 3.1 above, magnetic fields are applied on the payload. It is required that the chosen materials for the chamber or vacuum parts are made of materials with a low magnetic susceptibility. The magnetic susceptibility indicates the magnetizability of materials within an outer magnetic field. A magnetization could lead to deformations of the magnetic fields of the experiment and interference in these fields due to hysteresis effects [Sei14].

Another design requirement on the scientific payload for microgravity platforms, is to miniaturize a test setup which can encompass a whole laboratory on the ground. The design has to be miniaturized, compact, and at the same time stable, sustainable and autonomously operated. A constant mass optimization is required to fit into the mass limits and lower the launch or in-orbit placement costs. As briefly discussed in section 3.1.3, each kilogram brought into LEO costs approximately 2300 Euro. This shows that a trade-off between mass, size, cost factors, as well as the experimental requirements, are important for a successful mission, independent from the used microgravity platform.

4 State of the Art of UHV Systems for Experiments with Cold Atoms

In this chapter, the state of the art for ultracold atom experiments on microgravity platforms will be presented with a focus on their UHV systems. Ultracold atoms are used in several space missions for a multitude of fundamental physics experiments. These microgravity platforms, such as sounding rockets or earth-orbiting multi-user platforms like the ISS or Tiangong-2, have great advantages and offer experimental time scales under microgravity conditions not possible on earth. As presented in the following chapter, such experiments are extremely challenging with stringent requirements on the UHV system.

4.1 MAIUS-1

The MAIUS-1 mission is the first of three MAIUS missions within the QUANTUS consortium. It is led by the University of Hanover in cooperation with the University of Bremen, University of Hamburg, Humboldt-University Berlin, Ferdinand-Braun Institute Berlin (FBH), the University of Darmstadt and the University of Ulm. Additional universities and institutes are involved as subcontractors, one of which is the DLR Institute of Space Systems in Bremen [Gro16a]. MAIUS-1 was successfully launched in January 2017 on a VSB-30 sounding rocket from Esrange in Sweden, operated by MORABA. During the

6 min microgravity time, the scientific payload MAIUS-A was able to create a ^{87}Rb BEC and conducted around 110 experiments central to matter-wave interferometry [Bec18]. It demonstrated successfully several technologies essential for future spaceborne ultracold atoms experiments on longer time scales such as the ISS or onboard a satellite.

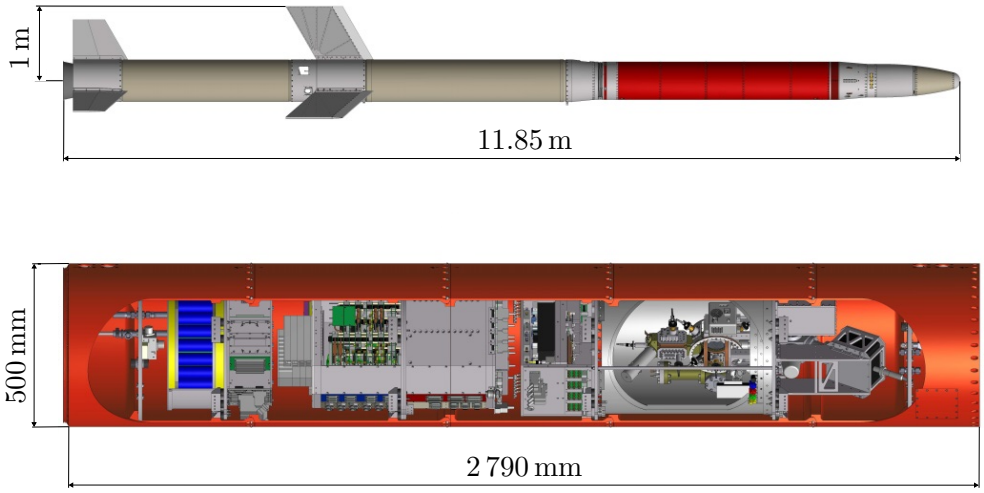

Figure 4.1: Overview of the scientific payload (MAIUS-A) of the MAIUS-1 sounding rocket mission [Gro16a].

The scientific payload as described in [Gro16a; Gro17a; Sei14] has a total length of 2 790 mm with a mass of 309.2 kg. Figure 4.1 shows an overview of the scientific payload (in red) on top of the two-stage VSB-30 sounding rocket. The pumping concept of the UHV system is equipped with two TSPs and one IGP, as explained in detail in [Gro16a; Gro16b]. A *IKR270* cold cathode gauge by *Pfeiffer Vacuum* is integrated into the vacuum system for the pressure measurement. As stated in section 3.2, a pressure of $\leq 5 \times 10^{-10}$ hPa is required by the experiment. Prior to the launch, an initial pressure of 8.5×10^{-11} hPa was measured, which was rising up to 4×10^{-10} hPa during the rocket ascent. Such a pressure rise was already observed during the qualification of the vacuum system. The increased pressure is caused by micro leakages of the CF flange connections, used throughout the UHV design. They are created by the applied mechanical loads within the burn phase of

the two-stage motor. After the stage burn out, the pressure stabilized at 7.2×10^{-11} hPa within 24 s and throughout the experimental phase [Gro17b].

This proved the capability of operating and maintaining a UHV system below the required threshold of 5×10^{-10} hPa onboard a sounding rocket. MAIUS-1 paved the way and improved the TRL of key technologies necessary for its successor missions MAIUS-2/3.

4.2 CAL

The Cold Atom Lab (CAL), from the National Aeronautics and Space Administration (NASA), was launched in June 2018 as the first earth-orbiting research laboratory for cold atom experiments to the ISS. The instrument has been developed and built, and is now remotely operated by NASAs Jet Propulsion Laboratory (JPL) [Ave20; Ell18]. It is a multi-user facility designed to study ultracold degenerate quantum gases of ^{87}Rb, ^{39}K, and ^{41}K [Ell18]. By providing a reliable BEC production, continuing operations could support long-term investigations of trap topologies. These trap topologies are unique to microgravity, few-body physics, pathfinding techniques for atom-wave interferometry, and atom-laser sources. CAL is located in an EXPRESS rack within the US Lab Module Destiny. It is divided into three main subsystems; the laser and optics system, the science module, and the electronics system. The subsystems are supported by thermal, mechanical and software control [Ave20].

The CAL vacuum system (as shown in figure 4.2) is based on a commercially available *ReBECi* vacuum chamber by *ColdQuanta*, which is CAL-specific modified. It is designed with two chambers made of glass and a silicon chip with a 0.75 mm diameter pinhole for differential pumping. The source cell (2D+ MOT chamber) is equipped with a non-evaporable getter (NEG), while the science cell (3D MOT chamber) maintains a pressure of $<1 \times 10^{-10}$ hPa with an IGP and a second NEG according to [Ell18]. The IGP and the

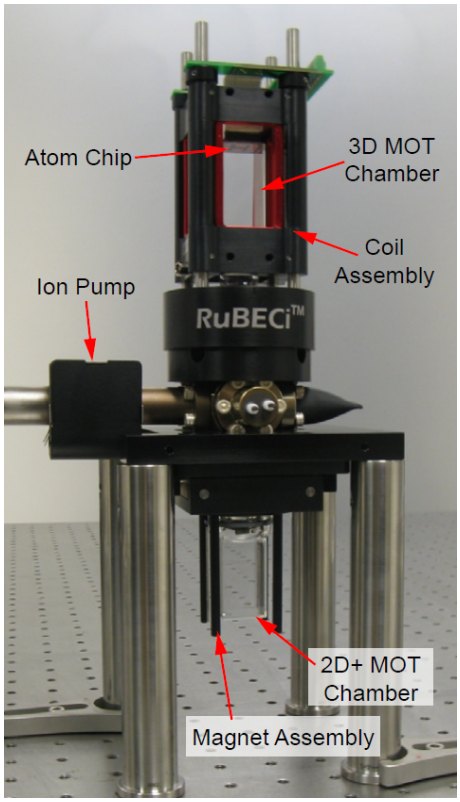

Figure 4.2: ColdQuanta RuBECi vacuum chamber used within the CAL project, which was modified for CAL-specific scientific objectives [Far14].

second NEG is integrated into a six flange stainless steel vacuum intersection. However, for the UHV, during flight or in operation, no further information is published.

4.3 BECCAL

The next generation of ultracold atom experiments on the ISS is called BECCAL (Bose-Einstein Condensate and Cold Atom Laboratory), which is a NASA-DLR collaboration. BECCAL will offer a versatile microgravity platform for a wide variety of experiments using ultracold rubidium and potassium atoms. It will be designed and built based on the knowledge gained

throughout the QUANTUS, MAIUS and the CAL project. An overview of the ongoing activities and the status is given in the publication [Fry21].

Similar to its previous missions, the payload consists of three subsystems; the laser system, the control electronics, and the physics package housing the main experiment (science chamber). For the performance of the experiments, the science chamber is kept under UHV. As stated in [Fry21], the vacuum level is maintained by an IGP and a TSP. While the IGP is operated continuously, the TSP is activated on regular intervals or when the vacuum quality needs to be increased. During the operation of BECCAL, a pressure range of 1×10^{-10} hPa is expected [Fry21].

No electrical power is provided for the integration into the launcher, the launch, and the flight to the ISS. Therefore at this time no pump is actively running, which results in a pressure rise. The BECCAL UHV system needs to be able to survive this time without power and at the same time keep the pressure below 1×10^{-5} hPa to re-activate the IGP in orbit [Fry21]. There is currently no data published on the detailed UHV system in BECCAL or its qualification process.

4.4 ACES

Atomic Clock Ensemble in Space (ACES) is an European Space Agency (ESA) mission which is scheduled to be launched on a Falcon 9 to the ISS [CNE21]. The ACES payload is located outside the European Columbus module at the Columbus External Payload Facility (CEPF). It aims to enable a multitude of advanced tests in fundamental physics, time keeping, and applications in different areas of research [Cac09; Lau15]. The key elements of the payload are two atomic clocks, PHARAO (Horloge Atomique par Refroidissement d'Atomes de
Césium) as a caesium cold atom clock developed by CNES (Centre National d'Etudes Spatiales), and the SHM (Space Hydrogen Maser) developed by

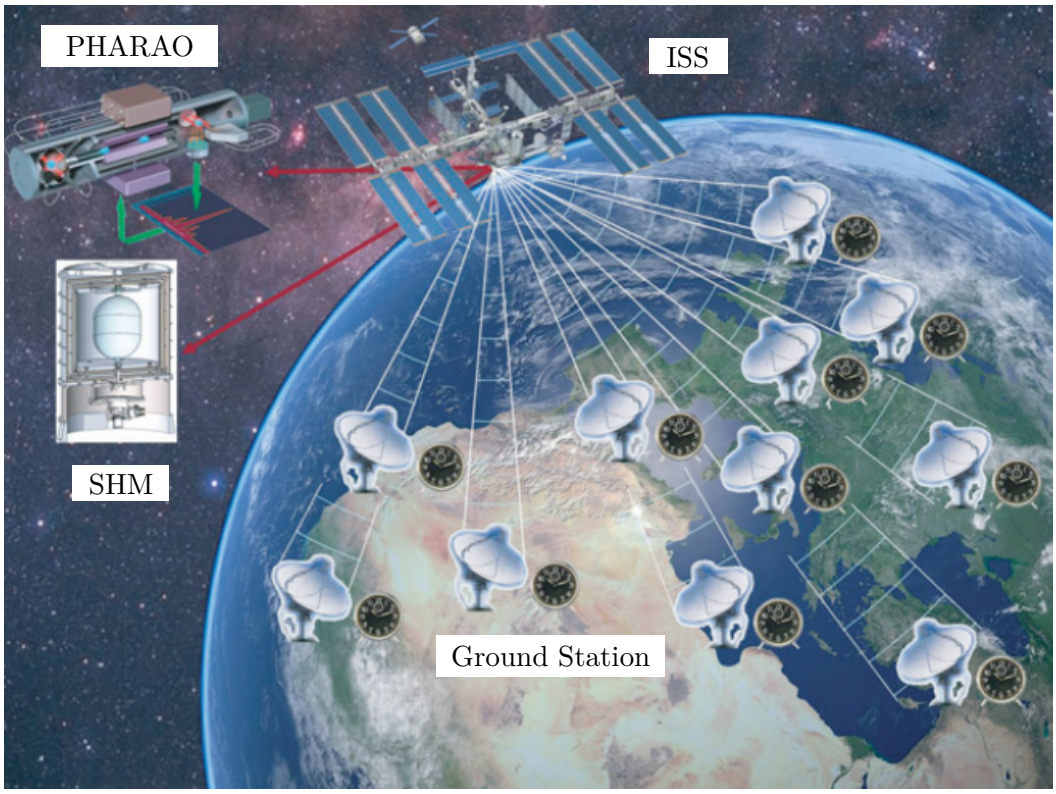

Figure 4.3: ACES mission concept overview [Cac09].

Spectra Time in Switzerland [Cac09; CNE21]. PHARAO ensures long-term frequency stability ($\tau \leq 3\,000\,\mathrm{s}$) and accuracy, while SHM is mandatory for frequency stability in the short and mid-term range ($3\,\mathrm{s} \geq \tau \geq 3\,000\,\mathrm{s}$) [Gou10]. The Frequency Comparison and Distribution Package (FCDP) distributes and compares the ACES clock signal between both systems. Via the Microwave Time-Transfer System (MWL), the onboard clock signal is compared with a ground based network of ultra-stable clocks on earth as shown in the mission concept in figure 4.3 [Cac09].

Both systems (PHARAO and SHM) require vacuum conditions for their instruments. The SHM requires a high vacuum system, within its physics package as described in [Ziv07]. The passive pumping of hydrogen (working gas inside the physics package) relies on 30 *ST-172 (Zr-Va-Fe)* [SAE12] non-evaporable bulk getters, each with a weight of 11 g. This getter array provides

a vacuum autonomy of 10 days without electrical power. The internal vacuum is additionally supported by two miniature ion pumps, each with a pump rate of $2\,\mathrm{L\,s^{-1}}$, in order to absorb the other background gases [Ziv07].

The core of the PHARAO system is the caesium tube with its UHV chamber developed by *Sodern Arianegroup*. To meet the requirement of $2.6 \times 10^{-10}\,\mathrm{hPa}$ [Gra04], the UHV system is integrated into the caesium tube. The cold caesium atoms are manipulated inside the UHV chamber, which is made of non-magnetic titanium. Equipped with a self designed ion pump and a set of five getters, it produces a pressure of $1.3 \times 10^{-10}\,\mathrm{hPa}$ [Gra04; Lau15].

4.5 SCAC

In September 2016, the Space Cold Atom Clock (SCAC) was launched with the Space Lab Tiangong-2 and was tested in orbit for almost three years until July 2019 when Tiangong-2 was deorbited [Ren20]. Under guidance of the China Manned Space Program (CMSP), the aims were to test and validate key technologies like laser cooling, the UHV system, the interrogation of cold atoms via Ramsey microwave fields in microgravity, and to accumulate data on the orbital environment for cold atom physics. The results of the mission are discussed along with the payload design in [Ren20].

According to [Ren15], the UHV system was designed to be kept below $5 \times 10^{-10}\,\mathrm{hPa}$. The physics package is the primary subject of the experiment with a ring cavity for the Ramsey interrogation of cold ^{87}Rb atoms by the microwave field inside a UHV chamber. The chamber within the magnetic shield is made of Titanium Grade 5. A dual-pump system was designed for this mission, as the UHV system was required to maintain the pressure for more than two months without a power supply [Ren15]. Two ion pumps are used for the main pumping system and additionally eight getters in two groups are kept in standby as a passive device. The getters can be activated if needed, but otherwise do not require power. Delta seals from *Garlock* with indium

were chosen for the sealing technology of the four flanges. The fluctuation of the magnetization induced by the Delta seals was $\leq \pm 1\,\mathrm{nT}$ [Ren15]. In [Liu18; Ren20] it is stated that the pressure of the SCAC in orbit was $<1 \times 10^{-9}\,\mathrm{hPa}$ without a constant power supply.

4.6 CAPR

As a successor of the SCAC mission, the Cold Atom Physics Rack (CAPR) is planned to fly on the Chinese Space Station. It will provide a multi-user apparatus for cold atom experiments with ^{87}Rb and ^{40}K [Liu21]. The goal of the vacuum system of the CAPR mission, is a pressure of $\leq 4.2 \times 10^{-10}\,\mathrm{hPa}$ [Liu21]. Additionally, the UHV system is required to maintain UHV conditions for more than one month without a power supply. Figure 4.4 shows an overview of the CAPR vacuum system with its main features. A two chamber system was designed, with a science chamber, a 2D-MOT chamber, and a DPS in between. The science chamber is connected to the main pumping system via a CF flange. Two dispensers, one for each species, are mounted as an atom source with a CF DN16 flange to the 2D-MOT chamber, as well as a small sputter ion pump (SIP) [Liu21].

For the connections throughout the vacuum system, standardized CF flanges are used. There are a total of twelve windows for optical access within the science and the 2D-MOT chamber, which are made of BK7 glass. They are pressed onto the chamber, and thereby sealed, with a 99.995 % pure indium wire [Liu21].

The pump system of the CAPR payload is realized in a dual-pump system with a SIP and an ion combination pump [Liu21]. Inside the main pump system, as shown in figure 4.4, a SIP with a pumping rate of $20\,\mathrm{L\,s^{-1}}$ (*Agilent VacIon Plus 20 StarCell*) is used. The ion combination pump is realized with the *NexTorr D500-5* from *SAES* combined with the getters *ST-172*. Eight additional getters *St171-16/10-NP* from *SAES* are designed in a flange

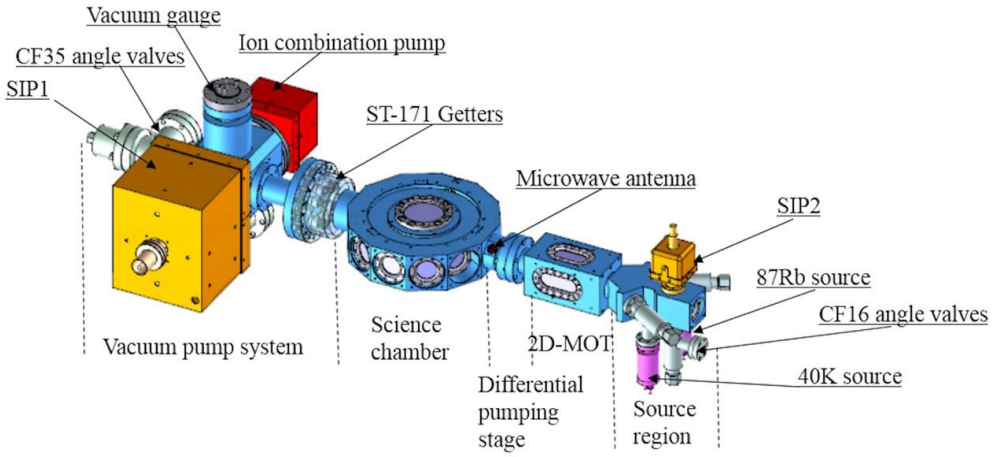

Figure 4.4: Overview of the UHV system of the CAPR mission [Liu21]

.

close to the science chamber, providing an overall pump rate of $96\,\mathrm{L\,s^{-1}}$. To comply with the power requirement of the UHV system, these getters are indispensable. The additional SIP at the 2D-MOT chamber is a *Gamma 3SCV1VOVNN* with a pump rate of $3\,\mathrm{L\,s^{-1}}$ [Liu21].

According to tests performed in [Liu21], the CAPR UHV system is capable of providing a pressure of $3.4 \times 10^{-11}\,\mathrm{hPa}$ measured on the vacuum gauge. Tests to investigate the performance of the vacuum system show that the pressure stabilizes at $1.5 \times 10^{-9}\,\mathrm{hPa}$ in power-off mode for one month. However, after switching on the power, the system recovered in less than ten minutes by reaching $3.4 \times 10^{-11}\,\mathrm{hPa}$.

5 Design of the Scientific Payload MAIUS-B

The design of the scientific payload MAIUS-B is presented in this chapter. In the first section, the mission overview is given with the general steps during the flight from launch to landing. This is followed by an overview of the overall scientific payload MAIUS-B, which successfully passed its payload critical design review (CDR) in October 2018. Section 5.3 introduces the within this thesis newly developed and implemented thermal design, including the TCS and the GSE concepts. The results of the conducted verification tests of the flow rate measurement for the cooling cycles are also discussed. In the next sections, the five subsystems of MAIUS-B are described and the implementation of the new TCS concept is highlighted, as it is one of the outcomes of this thesis.

To perform the major step from a single-species experiment (MAIUS-A) towards the dual-species experiment (MAIUS-B), the last section presents the realization and the implementation of the overall mechanical payload design. The contribution within this thesis includes the optimization of the mass and length budget, the implementation and safety assessment of the suspension design, and the newly implemented umbilical and sealing concept.

5.1 General Mission Overview

In January 2017, the MAIUS-1 mission successfully launched and was able to create a ^{87}Rb BEC, as well as conduct around 110 experiments central to matter-wave interferometry [Bec18]. With heritage and lessons learned [Gro17a] from its predecessor, the two missions, MAIUS-2 and MAIUS-3, plan to take the next steps towards future ISS or satellite missions. Both missions are flying the MAIUS-B payload. The MAIUS missions aim to set up an atom interferometer capable of performing a test of the UFF in space using two atom species, ^{41}K and ^{87}Rb [Pie21]. The UFF test is one of the main objectives for future satellite missions as proposed in STE-QUEST [Agu14; Tin13]. MAIUS-B aims to demonstrate key technologies crucial to fulfill the task of operating such an experiment on a future mission. In this context, this thesis provides new developments and optimizations necessary for the overall payload design, including the TCS and the mechanical design. Another contribution of this thesis is on the UHV technology and design developments, as well as the ground qualification of the MAIUS-B UHV system, as explained in detail in chapter 6.

Additional scientific objectives of the MAIUS missions are the generation of tunable ratios of BEC mixtures with ^{87}Rb and ^{41}K, and further studies on atom interferometry including the miscibility for both species. The experiment will make use of sympathetic cooling for the first time in microgravity. To experimentally investigate the applicability of ^{87}Rb and ^{41}K mixtures for a UFF test, a two-species DKC and magnetic transport protocols are implemented [Pie21].

The MAIUS-2/3 missions are both launched on a VSB-30 two-stage sounding rocket from Esrange in north Sweden, operated by MORABA. During the parabolic flight, similar as discussed in 3.1.1, the sounding rocket provides a microgravity and experimental time of around 330 s with an approximate apogee of 260 km. The final altitude and corresponding microgravity time depends on the final mass. Figure 5.1 shows the major events of the flight,

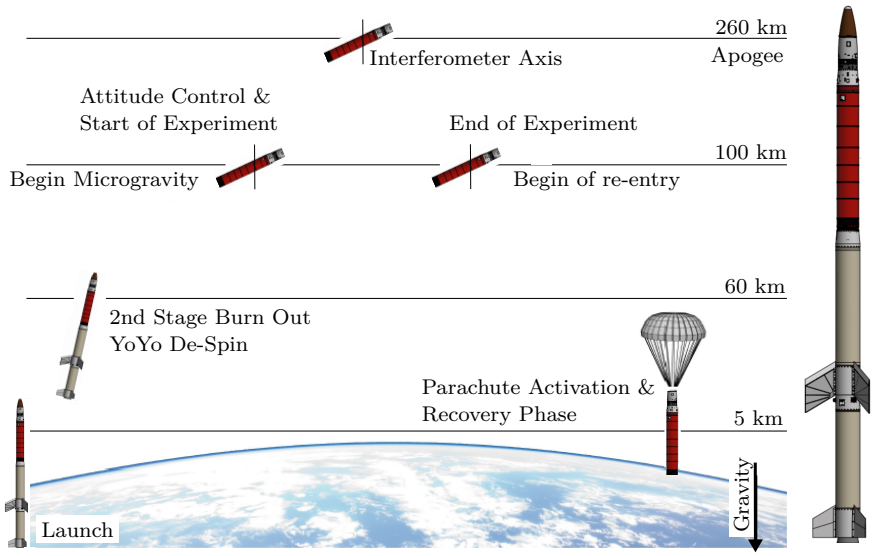

Figure 5.1: Flight and mission overview of MAIUS-B sounding rocket (adapted from [Gro16a]).

although for more detailed information please refer to [Gro16a]. After the launch and the burn out of the two stages, a yoyo de-spin reduces the rotation and the angular rates down to $0.03\,^{\circ}\,\mathrm{s}^{-1}$. The next step is the stage separation followed by the attitude control maneuver to align the interferometer axis with the gravity vector. Subsequently, the experimental sequences of the scientific program start with the beginning of the microgravity time around the Kármán line (100 km). The experiment time ends with the reentry phase followed by the activation of the parachute at an altitude of about 5 km. After the recovery, the payload will be inspected and the flight data investigated. The payload will then be prepared for the upcoming MAIUS-3 launch campaign.

5.2 Scientific Payload Overview

An overview of the scientific payload is shown in figure 5.2, with the two-stage VSB-30 sounding rocket (left) and the scientific payload (in red). As described in section 3.1.1, a sounding rocket offers a microgravity platform with residual accelerations in the range of 10^{-4} to $10^{-5}\,\mathrm{m\,s^{-2}}$ for around 300 to 360 s during the parabolic flight [Sta13]. The scientific payload is divided into five subsystems (from top to bottom); electronics (EL), physics package (PP), laser system (LS), laser electronics (LE), and batteries (BA), which will be described in the following sections.

The scientific payload houses a full setup to perform atom interferometry, using BEC mixtures of ^{41}K and ^{87}Rb, and provides the necessary electric currents for atom manipulation, laser frequencies, monitoring, and housekeeping for the overall system. The order of the five subsystems were chosen to place the atoms as close as possible to the center of mass. This placement helps to counteract any negative effects on the performance of the atom interferometer due to residual rotations of the payload.

The outer structure of the scientific payload is divided into seven Radial-Axial (RADAX) hull segments with a diameter of 500 mm and a wall thickness of 4 mm. All components of the different subsystems are mounted to an instrument platform (base plate) which is suspended to the hull segments with a total of six brackets. Each bracket is equipped with two passive rubber vibration dampers and a safety bolt. The safety bolt limits the stretch of the dampers to 2 mm to prevent them from damage and serves as a safety measure in case of damper failure.

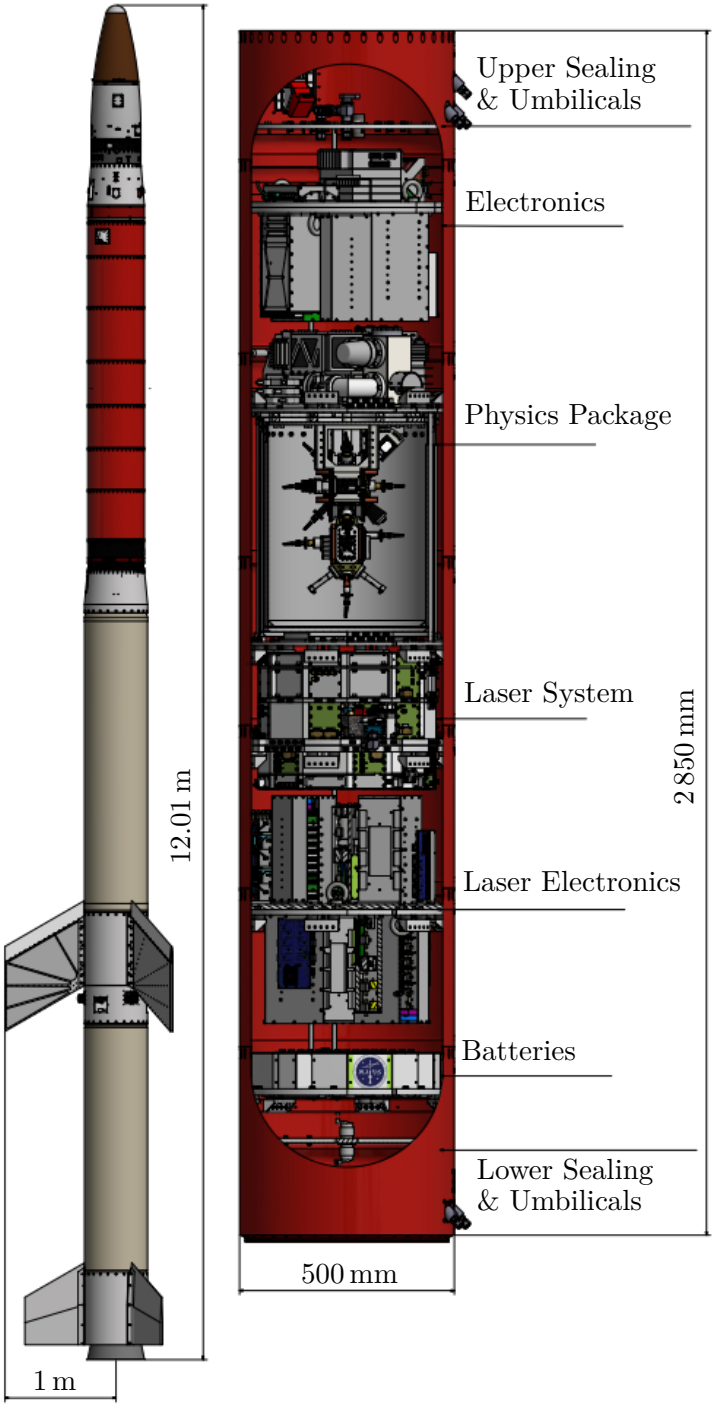

Figure 5.2: This CAD model was produced within this thesis, as an overview of the scientific payload (in red) on top of the two stages of a VSB-30 sounding rocket (left) with a detailed view of the scientific payload (right).

5.3 Thermal Control System and Ground Support Equipment

To fulfill the transition from a single-species experiment as in MAIUS-A, to a dual-species experiment in MAIUS-B, the TCS is one of the main key components for a successful operation, and is one of the tasks realized within this thesis.

A spaceborne dual-species ultracold atoms experiment, such as the MAIUS-B payload, requires a large amount of supply and control electronic and laser power to fulfill the scientific objectives. All these components produce a high internal heat load, with additional external heat loads by aerodynamic drag, during the ascent of the rocket. With the overall payload design being as compact and miniaturized as possible to fit into the size and mass limits, the heat is produced on a very dense space. This makes a TCS concept essential for the success of such a mission to protect and operate the temperature sensitive components within their recommended temperature ranges. While most of the components can be operated in a wider temperature range, certain components, such as the laser modules, require a well-defined and controllable operation temperature.

Furthermore, ii is necessary to identify the operation scenarios, not only throughout the flight, but also for the laboratory operation time. A complex experiment, such as MAIUS-B requires intensive ground operations, testing and experiments to set up the optimized flight system. For the MAIUS-B TCS concept as designed and implemented within this thesis, two operation modes (laboratory and fight mode) are considered. During the laboratory mode, active liquid cooling is provided by the GSE via the coolant umbilicals. This ensures a safe ground operation and the possibility of multiple subsequent tests over a longer period of time.

In flight mode and throughout the launch, active cooling is only supplied by the GSE via the umbilicals up to lift-off. For the flight, the TCS concept

relies on the thermal mass of the system. The thermal design of the payload needs to be designed in such a way that all temperature sensitive systems are still operated within their required temperature ranges.

The heat loads considered within the TCS design are primarily produced internally by the high power electronic components, as well as the lasers as stated above. In table 5.1, the estimated internal produced heat loads are showing a summarized load of around 707.6 W. In addition, a hull temperature up to 120 °C (393.15 K), caused by aerodynamic drag during ascent of the rocket, is taken into account.

Table 5.1: Internal heat loads of the MAIUS-B scientific payload

System	Heat load in W
Electronics	174.0
Physics Package	63.9
Laser System	100.0
Laser Electronics	340.9
Batteries	28.8
SUM	707.6

The following section describes the newly developed and implemented TCS and GSE concepts, as one of the outcomes of this thesis. As a baseline for the new TCS design of the payload MAIUS-B, the instrument platforms (base plates) of the different systems are serving as the heatsink. An exception is the PP, where only the pump stack for the IGP supply with additional high power amplifiers is equipped with a heatsink. In case of the EL, LE and the LS, two plates are screwed together and in between, a groove is milled and a stainless steel tube (meander) is placed. The heatsink, as shown in the CAD drawing in figure 5.3, was produced within this thesis. To take the manufacturing tolerances of the tubes into account, the groove is milled in such a way that these tolerances can be compensated. This results in free space which would decrease the heat transfer and lower the performance of the heatsink. Therefore, the free space is filled with heat paste before the two

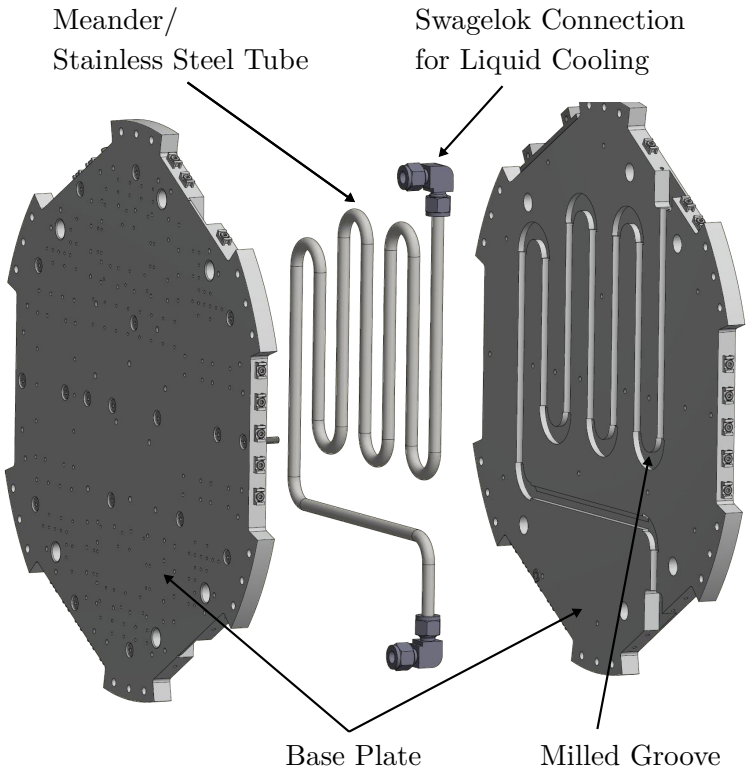

Figure 5.3: The LS heatsink is shown as an example for the basic heatsink concept as developed throughout this thesis, with two base plates and the stainless steel meander mounted in between. Both plates have milled grooves to place the meander. To connect the meander to the cooling cycles of the TCS, 90 degree swagelok connectors are used for the inlet and the outlet.

plates are mounted together. The inlet and outlet of the meander is connected via *Swagelok* connectors to be implemented into the cooling cycles.

For liquid cooling the TCS is divided into two cooling cycles, as shown in figure 5.4. One for the electronics BA, LE, EL (in blue) and one for the LS and the PP (in green). These cycles are connected via the umbilicals to the GSE, where a *Huber Unichiller 007* feeds the laser cycle and a *Huber Unichiller 010* feeds the electronics cycle. Since the chillers (GSE) are placed at the launch tower, they are mounted into an aluminum case. To withstand the rough conditions, like the exhaust gas of the rocket during launch, the cases are additionally covered with fire resistant pyroblankets. The GSE connects the liquid cooling cycles via hoses and the umbilicals payload TCS. The umbilicals

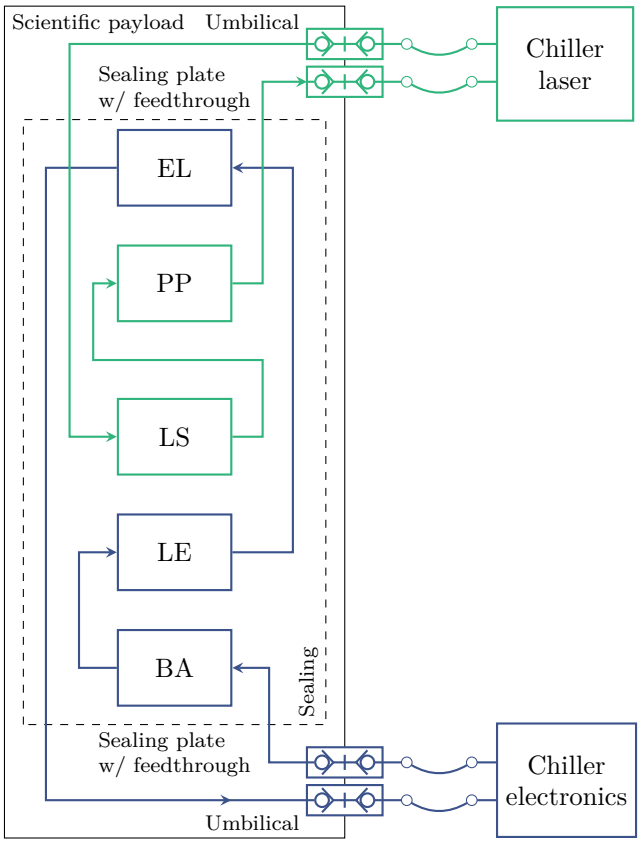

Figure 5.4: Schematic overview of the (two cycle) cooling concept of the TCS. The electronics cycle (in blue) feed the subsystems BA, LE and EL and the laser cycle (in green) the LS and PP.

are attached via lanyard steel cables to the launch rail, which will unlock the liquid cooling cycles automatically during the rocket lift-off.

The chillers provide a flow rate up to $25\,\mathrm{L\,min^{-1}}$ ($\mathrm{L\,min^{-1}}$=$\mathrm{dm^3\,min^{-1}}$) and allow for pressure loss compensation of up to 2.5 bar (2.5×10^5 Pa). A thermofluid (glycol/water mixture) is used to withstand the low ambient temperatures at the launch site/landing area, and to avoid any damage caused by freezing of the remaining cooling liquid inside the payload. This leads to a higher viscosity and a lower flow rate, which has to be taken into account in the TCS design. A test of the flow rate was performed within the scope of this thesis in order to quantify the actual flow rates and avoid thermal problems. To prevent freezing, two glycol-water mixtures are tested, one with 44 % of

glycol which prevents freezing down to -30 °C (243.15 K), and one mixture with 52 % glycol which prevents freezing down to -40 °C (233.15 K).

A pretest with two short hoses (0.8 m each) and a flow rate sensor, with a mixture of 52 % glycol, showed a flow rate of 6.4 L min^{-1}. For the final test, a realistic cooling cycle including the GSE but without the subsystems, was set up as shown in figure 5.5. This includes a total hose length of 21 m, which includes similar fittings, the actual hoses to and from the chiller, the umbilicals, and the feedthroughs. Similar to the pretest, the flow rate sensor has two short hoses (0.8 m each), and is directly connected to the lower umbilicals. During the test, the hull segments are mounted together and placed in flight configuration standing up (shown in figure 5.5) to account for the pressure drop due to the 2.8 m height difference to the chiller.

The results of the two tests show a flow rate up to 5.2 L min^{-1} for 44 % glycol and 4.8 L min^{-1} for 52 % glycol. These results state the impact of the glycol mixture which was taken into account within the TCS design. For the MAIUS missions, the mixture with 52 % glycol is used to prevent freezing down to -40 °C (233.15 K), and to be safe for all eventualities during and after a winter launch.

Figure 5.5: Flow rate test of the cooling cycles of MAIUS-B, as performed within this thesis. The GSE case, housing the chiller, is shown right next to the payload (red hull segments). The orange hoses are equipped with fire protection to avoid damage during launch.

5.4 Physics Package (PP)

In this section, a general overview of the MAIUS-B PP from an engineering point of view is given. The general PP design is divided into two main sections as shown in figure 5.6; the experiment chamber (EC) where the experiments are performed, and the pumping system (PS), which generates and maintains the vacuum. As one of the outcomes of this thesis, the implemented suspension is shown in detail and the heatsink concept is introduced. Since the focus in this thesis is on the MAIUS-B UHV system, the EC and PS are only briefly shown in this section, but will be explained separately in more detail in chapter 6. For more detailed information on the experimental setup, including the performance and the optimization steps on the experiment towards the launch, please refer to thesis [Pie21].

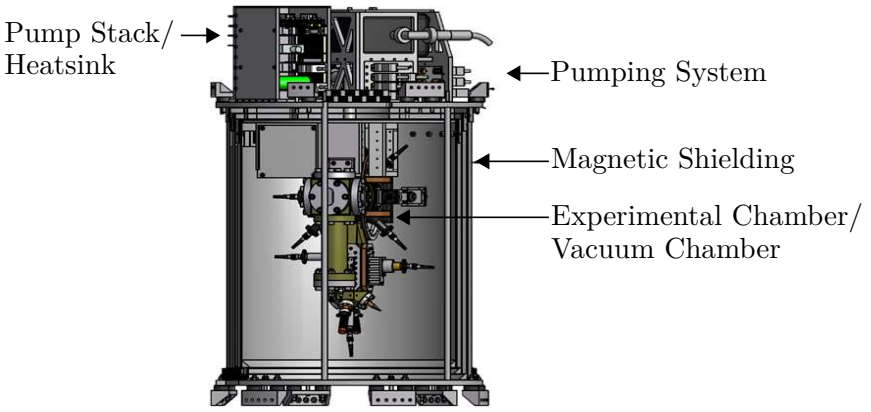

Figure 5.6: Overview of the MAIUS-B physics package.

As described in thesis [Sei14], a UHV chamber within a pressure regime of $\leq 5 \times 10^{-10}$ hPa is required to perform the experiments within the MAIUS missions. To achieve and maintain this pressure, the EC is connected to the PS. As one of the requirements for a cold atom experiment as stated in chapter 3, the PS has been separated from the EC to avoid negative impacts by the electronic components and the magnetic stray fields originated by the IGP. Additionally, a three-layer Mu-metal shield as shown in figure 5.6, is designed around the EC to reduce negative effects on the atoms by external magnetic

fields. The Mu-metal shield has a shielding factor of 10000 in a lateral and 2000 in a longitudinal direction [Kub16]. As in MAIUS-A [Gro16a], only Titanium Grade 5 and Aluminum 7075 are used inside the magnetic shield, to account for the requirements on the magnetic properties.

For the EC a two chamber design has been chosen. The preparation chamber, which has a comparatively high partial pressure, is separated from the science chamber, which requires a lower partial pressure. The pressure difference between these chambers is maintained by a DPS (see section 6.2.3). This ensures a sufficient atom flux from the preparation chamber, while the lower pressure in the science chamber increases the lifetime of the atomic ensembles due to less collisions with the background gas. The K and Rb atoms are confined in a 2D-MOT inside the preparation chamber. From here, the atoms are directed via laser light through the DPS into the center of the science chamber. As an atom source, two newly designed ovens are mounted via a CF DN16 flange to the preparation chamber. Each oven carries 1 g of K and Rb, respectively. The Rb oven is unheated at room temperature, while the K oven is kept at 46 °C (319.15 K). Compared to MAIUS-A, a new oven design was developed as a part of the scope of this thesis. The oven design as carried out within this thesis, is described in detail in section 6.2.3.

The science chamber is equipped with an atom chip, which has a low current consumption and fast switching times, while being able to create high magnetic field gradients for atom trapping. Additional coils around the preparation chamber are producing a quadrupole field in a racetrack configuration. Separate coils around the science chamber provide the offset fields.

The EC, as well as the coils, are mounted to the base plate with a ring structure which provides stability and mounting points for additional components, such as the optical detection systems. The mounting concept conducted within this thesis, as part of the UHV system design, will be explained in detail in section 6.2.2. The experiment requires absorption imaging, as well as fluorescence imaging, and are perpendicularly aligned and attached to the EC. For cooling and manipulating the atoms, several collimators preparing

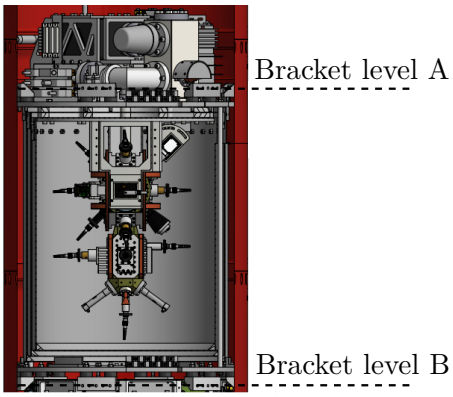

Figure 5.7: The PP is mounted with six brackets each, on two mounting levels A and B.

the light fields for the experiments are mounted to the EC. The light from the collimator for the matter wave interferometer is retro-reflected from a mirror on the opposite side of the vacuum chamber while passing twice through a quarter-wave plate. The residual accelerations of the interferometry mirror are measured by an accelerometer mounted behind the mirror.

The PP at 73.8 kg is the heaviest subsystem and has a total length of 745.5 mm due to the magnetic shielding. This could result in a damaging side movement, as a result of the external loads. An additional problem is that the magnetic shielding, which can be seen in simplified terms as a cylindrical tube, has an outer diameter of 420 mm. With an inner diameter of 492 mm inside the hull segment, this only gives a space of 36 mm on each side before the shielding hits the hull. To avoid damage, the PP is mounted on two levels as shown in figure 5.7. A total of twelve brackets, one at the actual instrument platform (level A) and one on the lower end of the system (level B) are implemented. This prevents movements which could possibly damage the system, as one fixing position could cause failure of the brackets due to a high momentum caused by a long lever arm combined with a high mass during static and dynamic loads.

As mentioned in section 5.3, the instrument platform of the PP is in contrast to all other subsystems and not equipped with an active liquid cooling.

The heat load of approximately 63.9 W is produced at the high power amplifiers which are placed on the back wall of the pump stack (see figure 5.6). Therefore, only the back wall is equipped with active liquid cooling, following the same heatsink concept as presented in section 5.3.

5.5 Laser System (LS)

The LS was designed and built within the MAIUS team by the Humboldt-University Berlin, the Ferdinand-Braun Institute Berlin, the University of Hamburg, and the University of Mainz. Within the scope of this thesis, a new heatsink (base plate) design was developed and built to account for the temperature sensitive components, such as the laser modules.

The LS is controlled and powered by the LE subsystem (section 5.6.2) and provides light fields for cooling and manipulating ^{41}K and ^{87}Rb atoms. All components are placed inside one of the five functional modules as shown in the CAD drawing in the upper view in figure 5.8. These modules are mounted equally on both sides of the base plate (heatsink) (figure 5.8, Pos. C). The layout of the heatsink was designed in such a way that the temperature control of the temperature sensitive components, including the laser modules, is optimized. Additionally, the temperature sensitive components are individually equipped with Peltier elements for a more advanced temperature control. All lasers are directly mounted to the heatsink, since they are the highest power consuming components with around 10 W each. The LS heatsink, as already shown in figure 5.3, follows the baseline concept of the TCS as introduced in section 5.3.

Within the LS, a total of ten micro-integrated lasers are used, five for ^{41}K, four for ^{87}Rb and one for the dipole trap. For each atomic species, a distributed feedback (DFB) laser, one at 780 nm (^{87}Rb) and one at 767 nm (^{41}K), serves as a reference laser, stabilized to a spectroscopy module. The seven science lasers for ^{87}Rb and ^{41}K are based on a master-oscillator-power-amplifier

(MOPA) concept, where an extended cavity diode laser (ECDL) serves as the master oscillator. For the optical dipole trap an ECDL-MOPA laser at 1 064 nm is used [Kür20; Wic17]. As shown in sections A-F of the schematic overview in figure 5.8, the seven science lasers (ECDL-MOPA) are placed in the laser module (figure 5.8, Pos. B). The other three reference (DFB) and dipole (ECDL-MOPA) lasers are placed within the reference module (5.8, Pos. D).

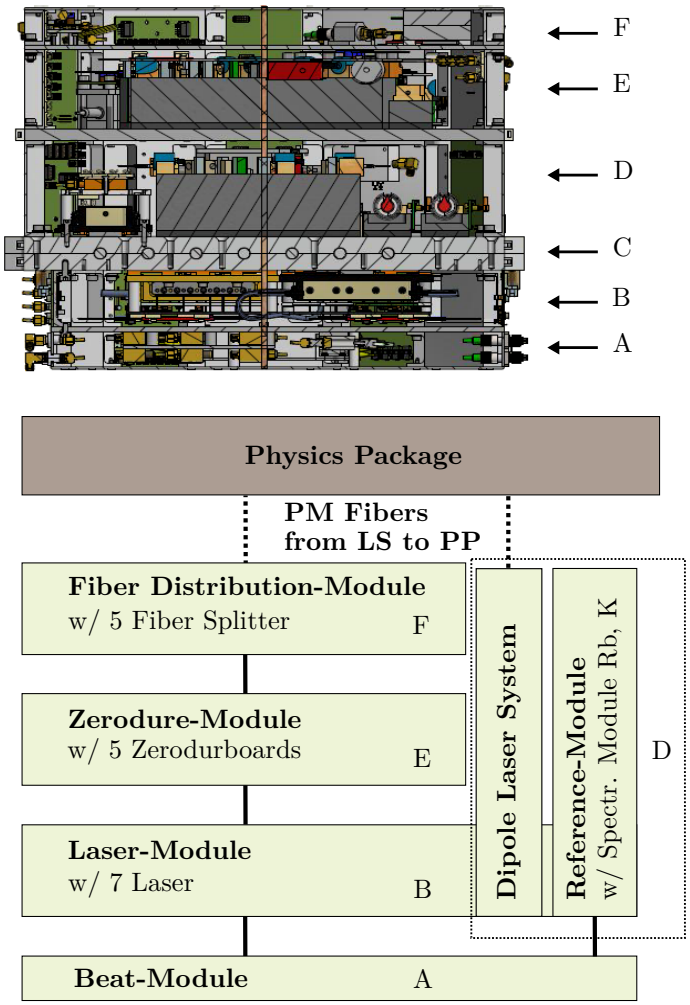

Figure 5.8: CAD-Model (upper view) and schematic overview (lower view) of the MAIUS-B laser system (from bottom to top): A) Beat-module, B) Laser-module, C) Heatsink, D) Reference-modele, E) Zerodure-module, f) Distribution-module.

The light from the science lasers is fiber coupled to the five zerodurboards inside the zerodure module (figure 5.8, Pos. E). On these zerodurboards, the distribution and switching is realized with glued-on optics for low-loss beam manipulation in a free space design [Dun14; Mih19]. The light pulses generated via acousto-optic modulators (AOMs) on the zerodurboards are guided via polarization maintaining (PM) fibers to the distribution module (figure 5.8, Pos. F) where the light fields are overlapped and combined in fiber splitters. The light from the dipole laser system and from the distribution module is guided via eleven PM optical fibers to the PP. The LS is designed in a modular way and the five compact integrated functional modules are accessible via hinges, which allows for access to the components inside in case of necessary maintenance or repairs.

5.6 Electronic System

The electronic system of the MAIUS-B scientific payload, as described in the following sections, is designed and built at the Leibniz University Hanover within the MAIUS team. As shown above in section 5.2, the overall electronic system is divided into three subsystems; batteries, laser electronics, and general electronics. Since all electronic subsystems are housing high power components on a very compact and dense design, a new heatsink concept was developed and implemented within the scope of this research. The heatsink design of the different electronic subsystems are discussed in the following sections below.

Throughout the electronic system of the MAIUS-B payload, the communication between the different subsystems and stacks is based on a network made of polymer optical fibers. Polymer optical fibers prevent ground loops between the connected components and use only one fiber. This reduces the overall mass and complexity of the cable routing.

5.6.1 Batteries (BA)

To connect all components, including the battery packs, communication boards, power switches and the overload protection, the BA is built on a motherboard. With a total of 24 output channels, each providing 6.6 V and 20 V, the BA distributes the necessary voltages throughout the scientific payload. All channels are separately controlled via the software and all output currents and voltages are monitored.

Eight $LiFePO_4$ 15 A h batteries, in a two-cell and six-cell configuration, deliver the power and can be charged with up to 20 A charging current. Based on calculations, this allows for an autonomous system operation time of 40 min, which is sufficient for the MAIUS flight with an additional margin. The temperature within the module is monitored, and in case of overheating, the

charging current is regulated by the firmware. A safe operation is guaranteed by a 30 A fuse to protect the charging currents and a 10 A fuse for the individual outputs to the experiment.

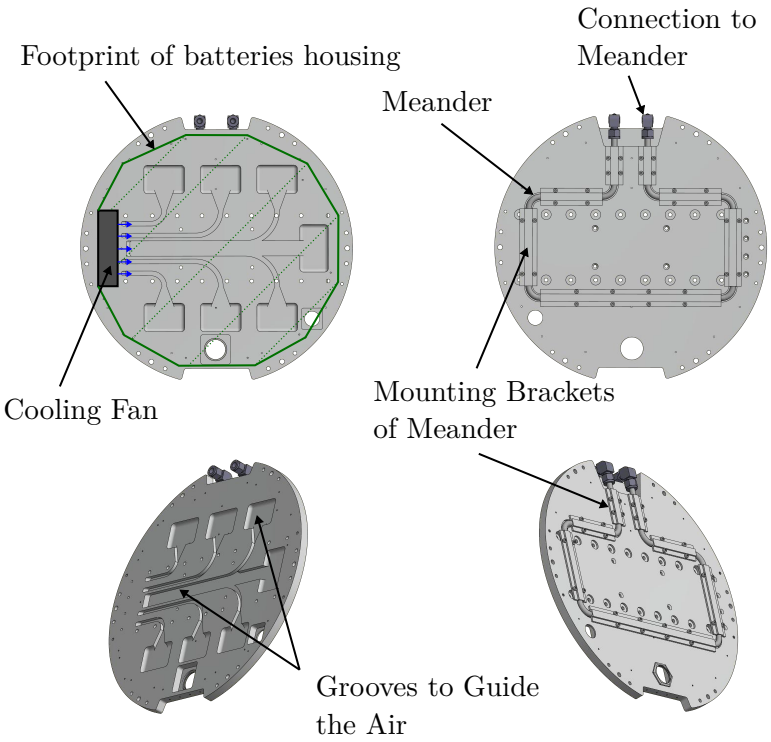

Figure 5.9: New heatsink concept of the batteries module, as carried out within this thesis, including the meander and their mounting brackets. The green line and the dotted area shows the footprint of the metal housing where all components of the battery module are sheltered. For the cooling concept, a fan is placed and the air is guided via milled grooves under the components with a high heat load.

The BA system is sheltered in a metal housing (footprint and area shown CAD model in figure 5.9, produced within this thesis) on one side of the base plate (heatsink). In deviation to the LE and EL, the BA heatsink is only made of one plate since the heat load compared to the other electronic subsystems (see table 5.1) at 28.8 W is significantly lower. With only one plate, the mass of the BA system could be reduced substantially without risking any thermal problems. As indicated in figure 5.9, a fan is used to circulate the air throughout the housing and milled grooves in the base plate are used to guide the air for cooling to high power components.

5.6.2 Laser Electronics (LE)

The LE subsystem consists of two similar submodules, one for ^{87}Rb and one for the ^{41}K section of the LS, mounted on the base plate (heatsink). Each submodule generates the control loops for the laser frequency stabilization, monitors the laser frequencies, and delivers the currents for the lasers. In addition, RF to drive the AOMs are synthesized and amplified. A dedicated temperature control system is included to stabilize the temperatures of the lasers.

As a baseline concept throughout the scientific electronics of LE and EL, all components are in a modular design for the different functional groups. Each side of the LE contains two main modules (stacks) formed by several stacked cards, similar to the PC/104 format. In order to operate an ECDL-MOPA laser, two current drivers are necessary, one delivering up to 400 mA for the master laser oscillator and one variant delivering up to 2.5 A for the power amplifiers. The current driver cards are divided into the two main stacks. One of the stacks houses the current driver cards for the power amplifier lasers, which are designed to provide a low-noise current output. The second stack delivers the currents for the scientific lasers and their respective frequency controller. In addition, it offers frequency stabilization of the reference lasers, control of frequency offsets between lasers and allows for a phase lock loop (PLL) between two lasers.

The high power components of the laser current driver circuits are mounted on the back wall of the main stacks. This back wall is designed to allow for a better heat transfer to the heatsink (base plate). For a better connection area, the back wall and the base plate was optimized within this thesis to avoid overheating the components inside the stacks during operation. The meander of the heatsink is guided under this area for an optimal heat transport and cooling of the stacks. Inside the stacks, fans and cooling fins mounted directly on the base plate, are used to circulate and at the same time cool the air and the components. All stacks and components are placed to keep the center of

mass close to the rotation axis in the middle of the system and have been optimized regarding mass.

5.6.3 General Electronics (EL)

Similarly to the LE and LS, the EL subsystem is divided in two submodules and the base plate of the subsystem serves as the heatsink within the TCS.

One side supplies currents for the coils and for the atom chip structures of the PP configured together in one stack. The current drivers deliver up to 10 A, while the low-noise current source aims to minimize heating and losses of the magnetically trapped atoms [Fol02]. It houses the associated stacks for the RF electronics, and for the generation of microwave and RF signals used for the evaporation and state preparation of the atoms. Beside further auxiliary electronics and a six cell battery pack for the coil current driver, it includes a stack with eight *MEERSTETTER* temperature controllers for the Peltier elements of the lasers in the LS. A separated module for the atom chip protection contains fuses, switching capabilities, and additionally monitors the currents delivered to the chip structures.

On the other side of the EL subsystem, a two cell galvanically-isolated battery stack supplies the chip current driver and parts of the microwave evaporation system. The extra batteries need to be galvanically isolated to avoid noise on the outputs of the current drivers from the rest of the system, via the power supply. Such a noise would lead to atom losses and a lower performance of the experiment. Furthermore, an isolated supply helps with the identification of error states since the atom chip wires are short-circuited. The battery pack is charged via the umbilicals by a galvanically-isolated power supply within the GSE. This side additionally houses the main computer, responsible for housekeeping and telemetry data processing, and provides the predefined experimental sequences.

5.7 Mechanical Design

In this section, the mechanical design of the MAIUS-B payload is presented. As a part of this thesis, the necessary mass and size optimizations of the overall mass and length budget and the investigations on the suspension of the subsystems are presented. The sealing and umbilicals concept, developed for the MAIUS-B payload within this thesis, are introduced.

5.7.1 Mass and Length Budget

The final payload mass of MAIUS-A was 309.2 kg with a length of 2 790 mm [Gro17a]. While MAIUS-A only used one atom species (^{87}Rb), MAIUS-B provides the scientific payload for a two-species experiment (^{41}K and ^{87}Rb). For this reason, a significant amount of new hardware had to be included within the payload design in MAIUS-B. First design iterations performed throughout this thesis have shown that this would lead to an extra mass of approximately 90 kg and length of 930 mm [Els18]. This would exceed the limits for the MAIUS-B payload, which are at 340 kg and 3 000 mm. The mass limit is important to ensure a safe landing with the parachute system provided by MORABA. In addition, the stress on the manacle-ring, which connects the payload with the rocket motor of the sounding rocket, rises during flight with a higher mass. The maximum stress level of the ring must not be exceeded for a safe flight.

The experimental time under microgravity conditions correlates with the final payload mass. As a first approximation, the investigations performed by MORABA show a decrease in microgravity time of around 0.55 s per additional kg payload mass. It is important to mention that this approximation is only valid in the MAIUS-B used two-stage VSB-30 sounding rocket and the used rocket nose cone design. During the MAIUS-1 flight a total of around 110 experiments were conducted within the 6 min. As such, a lower microgravity time will unavoidably lower the amount of feasible experiments. This high-

lights the importance of an intensive mass optimization process throughout all design steps which have been conducted within the scope of this thesis.

During this mass and size optimization process, several iteration steps and design optimizations have been done. One of the main design changes of the overall payload design, is the reduction of the wall thickness of the hull segments (from 5 to 4 mm). Based on the RADAX hull design in MAIUS-A, hull segments were redesigned with the reduced wall thickness. This results in a mass reduction of around 10 kg.

All structural components, such as the instrument platforms of the subsystems or the sealing of the payload, were optimized in a trade-off between mass and structural stability. As one of the scopes of this thesis, major parts of the PP were redesigned or newly developed as shown in detail in section 6.2. This includes the PS design and the concept of the EC mounting system, which are both explained in detail in the following chapter. By the redesign of the PS, the height was reduced from 420.5 mm in MAIUS-A, down to 187 mm in MAIUS-B.

With a final length of 2.8 m (see figure 5.2) and a mass of 335.3 kg, as presented in the mass budget in table 5.2, the MAIUS-B payload is below the set mass and size limits.

Table 5.2: Mass budget of the MAIUS-B payload

System	Mass in kg
Electronics	31.0
Physics Package	73.8
Laser System	53.5
Laser Electronics	35.2
Batteries	17.9
Cables & Cooling cycle	35.7
Sealing	8.1
Hull segments	80.1
SUM	335.3

5.7.2 Suspension

As stated in section 5.2, the instrument platforms are mounted to the hull segments with a total of six brackets. To avoid damage and failure of the brackets at the main instrument platform, the PP is additionally mounted with a second plate and six brackets below the magnetic shield. All platforms have in common, that the six brackets are placed with a 60° angle spacing around the rotation axis. The brackets have five holes for the mounting to the hull segment and three M6 threaded holes for the mounting to the platform. All brackets are manufactured from aluminum EN AW 7075, with a typical yield strength of $462\,\mathrm{N\,mm^{-2}}$ and a tensile strength of $533\,\mathrm{N\,mm^{-2}}$ [Gro16a]. For the connection to the platform, the suspension is equipped with two vibration dampers and one safety pin in the middle. The PP has two smaller brackets on the upper instrument platform (see figure 5.7 level A) with only one damper and the safety pin to be able to fit all components onto the upper platform. The general mounting concept is that the two passive vibration dampers and the safety pin are screwed into the bracket through the holes in the base plate, and mounted on the other end by M6 nuts. The safety pins allow a maximum deformation of 2 mm on the vibration dampers. This avoids damper failure in case of high loads, which could lead to major damage throughout the payload.

For the final integration, the brackets are first mounted on the hull segments, which are already equipped with the dampers and the safety pin, and after lifting the system in place, the M6 nuts are torqued. Since the PP is sheltered in two hull segments due to manufacturing reasons, the upper mounting level A (see figure 5.7) is designed in such a way that the dampers and pins are screwed into the base plate. The bracket has through holes and will be mounted with the M6 nut at this end. All threads are reinforced with Helicoils to strengthen the thread flanks in each connection, and to withstand high loads.

Table 5.3: Loads per brackets with the safety factor S_B and the safety against slipping S_S for all subsystems are shown. ($1\,g_0$=$9.81\,m\,s^{-2}$)

	Accel. in $m\,s^{-2}$ (g_0)	Load in N	Load/bracket in N	S_S	S_B
Electronics	127.5 (13.0)	3 953.4	658.9		
(31.0 kg/6 brackets)	245.3 (25.0)	7 602.8	1 267.1		
	490.6 (50.0)	15 205.5	2 534.3		
	981.0 (100.0)	30 411.0	5 068.5	13.2	1.7
Physics Package	127.5 (13.0)	9 411.7	1 568.6		
(73.8 kg/6 brackets)	245.3 (25.0)	18 099.5	3 016.6		
	490.6 (50.0)	36 198.9	6 033.2		
	981.0 (100.0)	72 397.8	12 066.3	5.6	1.4
Laser System	127.5 (13.0)	6 822.9	1 137.1		
(53.5 kg/6 brackets)	245.3 (25.0)	13 120.9	2 186.8		
	490.6 (50.0)	26 241.8	4 373.6		
	981.0 (100.0)	52 483.5	8 747.3	7.7	1.5
Laser Electronics	127.5 (13.0)	4 489.1	748.2		
(35.2 kg/6 brackets)	245.3 (25.0)	8 632.8	1 438.8		
	490.6 (50.0)	17 265.6	2 877.6		
	981.0 (100.0)	34 531.2	5 755.2	11.6	1.6
Batteries	127.5 (13.0)	2 282.8	380.5		
(17.9 kg/6 brackets)	245.3 (25.0)	4 390.0	731.7		
	490.6 (50.0)	8 780.0	1 463.3		
	981.0 (100.0)	17 559.9	2 926.7	22.9	1.8

The used brackets are based on the general design for the MAIUS-1 mission [Gro16a]. The layout of the payload and the mass of each subsystem was changed for the MAIUS-B payload, as such the load and safety assessment of the suspension and the brackets were renewed as a part of this thesis. For the calculations, the accelerations of around $127.5\,m\,s^{-2}$ ($13.0\,g_0$) during rocket ascent and up to $245.3\,m\,s^{-2}$ ($25.0\,g_0$) for the re-entry are considered. During the maximum load, shocks between $490.6\,m\,s^{-2}$ ($50.0\,g_0$) and $981.0\,m\,s^{-2}$ ($100.0\,g_0$) during the landing and the motor ignition can appear and need to be taken into account.

The load per bracket is shown in table 5.3 where the mass and the accelerations are considered. Although the PP is mounted with a total of twelve brackets, the worst case was assumed with only one suspension level of six brackets. The PP is the heaviest subsystem, which results in the highest loads per bracket as indicated in table 5.3. The safety factor S_B for different loads per bracket was simulated with a FEM simulation during the MAIUS-1 mission and can be used here as well, since the design of the brackets stayed the same. In figure 5.10, the safety factor is plotted over the applied load, with the safety factor of the bracket defined as the quotient of the yield strength and the maximum van-Miese comparison stress [Gro16a].

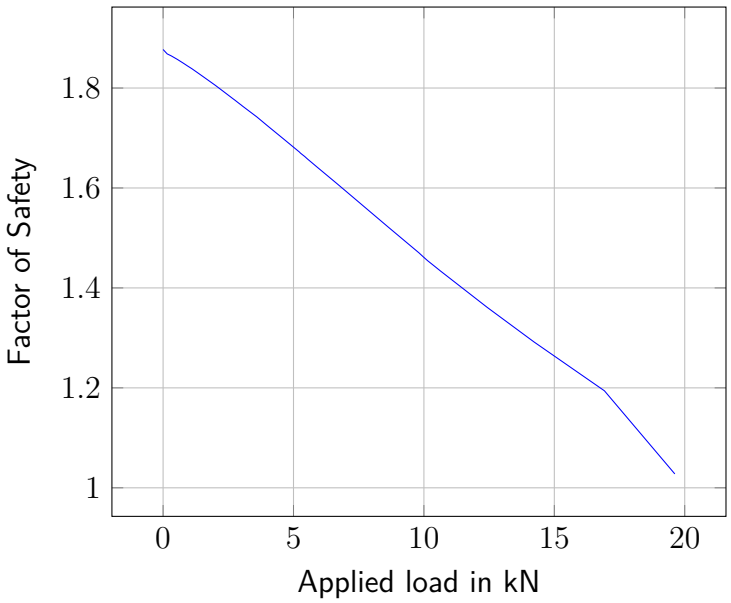

Figure 5.10: Minimum factor of safety per brackets for different applied loads [Gro16a].

The minimum safety factor S_B of the bracket for the maximal load case of 100 g is stated in table 5.3 for all subsystems. For the highest load per bracket of 12 066.3 N at the PP, this results in a minimum safety factor of 1.4.

The brackets are mounted with five M5 x 12 mm stainless steel (class 10.9) screws to the hull segment as mentioned above. In addition to the safety factor of the bracket itself, the safety against slipping for the connection between

the bracket and the hull was investigated. The safety factor against slipping S_S is given by formula 5.1 as

$$S_S = \frac{F_p \mu n}{F}\,, \tag{5.1}$$

where F_p is the pretension force of the screw, F the load per bracket, μ the friction coefficient between the bracket and the hull, and n the number of screws per bracket [Eng19]. The pretension force F_p for a class 10.9 M5 screw with an friction coefficient of 0.14 is 10 300 N and the friction coefficient μ between the bracket and the hull is 1.3 for a aluminum-to-aluminum connection [Muh03]. The results are presented in table 5.3 which show a minimum safety factor against slipping of 5.6 for the heaviest subsystem (PP) and the highest load per bracket. This shows that the brackets and the mounting of the MAIUS-B payload are capable of carrying the subsystems for acceleration loads up to 981.0 $\mathrm{m\,s^{-2}}$ (100.0 $\mathrm{g_0}$) with a reasonable safety margin.

5.7.3 Umbilicals and Sealing

As mentioned in beginning of section 5.2, the scientific payload is sheltered in seven RADAX hull segments. RADAX is a standardized flange system, which is used in several sounding rocket missions, as well as for the MAIUS missions. To ensure a constant and reproducible environment inside the payload, it is pressurized with artificial air (80 % nitrogen and 20 % oxygen). The RADAX hull segments are manufactured with a lining groove and sealed with a rubber o-ring made of HNBR (hydrogenated nitrile rubber) which has a hardness of 70 Shore. The payload is sealed on both ends with a sealing plate, which is sealed with an o-ring in the upper and lower hull segment. These sealing plates are each equipped with *Swagelok* bulkhead fittings, feedthroughs for liquid cooling and a ball tap for pressurization and flushing of the payload. Additionally, feedthroughs for data and power are placed in the sealing plates. As a lessons learned from the MAIUS-1 mission, as stated in [Gro17b], the formerly used hermetically DSUB connectors showed leakages during testing,

especially for the high-current feedthroughs. For the MAIUS-B payload hermetic military grade connectors and feedthroughs are used throughout the entire umbilical concept.

The sealing concept was also tested within the scope of this thesis, to quantify the pressure loss over time. For the test, the hull segments including the sealing plates are prepared in a flight configuration. Prior to the main test with all seven segments, a pretest was performed to detect possible leakages in the sealing plates, and the cooling and data/power feedthroughs. Therefore, only the two outer hull segments housing the sealing plates are mounted to each other. Both sealing plates are equipped with a valve to flush and pressurize the payload. For the two tests, one valve is connected to a pressure sensor from *B+B Thermo-Technik (DRTR-ED-10V-A5B)* to read out the pressure over time. The other valve is connected with a gas bottle to pressurize the hull segments with artificial air.

To simulate the conditions during the flight, the pressure difference between the outside (vacuum) and the inside of the payload (atmospheric pressure) will be around 1000 - 1 100 hPa. The hull segments in both tests were pressurized to an absolute pressure of around 2 100 hPa. During the pretest, the pressure was monitored and logged for 48 h with a total pressure loss of 6 hPa. For the same test during the MAIUS-1 mission, a pressure loss of 55 hPa over 40 h was seen. The differences can be explained by the military grade connectors used in MAIUS-B, compared to the DSUB connectors as used in MAIUS-A. This showed that the use of the military grade connectors significantly improved the sealing concept.

For the test with all seven hull segments in flight configuration, but without the subsystems inside, the conducted test was performed for 90 h with a total pressure loss of 40 hPa. This shows no significant leakages are expected before and during the flight by the overall sealing concept.

After the final integration of the payload and during the integrated operation in the laboratory, the payload needs to be further accessible for liquid

cooling, data, and a power connection. Therefore, the payload is designed with umbilicals for a connection to the respective GSE until launch. These eight umbilicals (four on each side) for cooling, data and power are equipped with push-and-pull quick connectors. The connectors are attached via a lanyard steel cable to the launch rail and unlock automatically by the pull of the rocket as it lifts off. To ensure a reliable connection and avoid any leakages, all electronic connections are using military grade connectors. The hoses and cables from the umbilicals to the GSE are isolated with a fire protection and rated up to 200 °C (473.15 K), to withstand the high temperatures during the rocket lift-off.

6 UHV System Design of MAIUS-B

For a successful mission with cold atoms, the UHV system plays a major role. As stated in section 3.2, the vacuum conditions have a direct impact on the performance of the experiment. As a primary outcome of this dissertation, this chapter shows the design, assembly and qualification of the new UHV system of the MAIUS-B sounding rocket mission as carried out within this thesis. In addition to section 3, the specific requirements on the vacuum system and the environmental conditions in MAIUS are discussed. The mechanical design developed throughout this thesis is explained, as well as the implemented UHV system design for the MAIUS-2/3 mission. In the first section, the cleaning and vacuum preparation is introduced as it was done within the MAIUS-B assembly. Section 6.2.2 shows the EC and the PS, which was designed and flight-ready assembled within the scope of this thesis. The next section includes the designs of the pumps, the DPS, and the new oven, all of which were designed within this dissertation. Section 6.3 gives a detailed overview about the qualification process of the MAIUS-B PP, including the UHV system. These vibration tests, as performed throughout this thesis, show the successful qualification process undertaken as a final step towards the MAIUS launch. The lessons learned are given in the last section, as derived from the qualification and the general design process. These lessons point out necessary steps which need to be investigated to improve the design of UHV systems for future space missions.

6.1 Requirements and Environmental Conditions

A sounding rocket mission is an extremely challenging environment for a UHV system, since it is very sensitive to environmental influences. The UHV system needs to be reliable, mechanically stable, and autonomously able to maintain UHV conditions. It is mandatory that the residual pressure within the vacuum system is less than 5×10^{-10} hPa. Also, to provide the experiment with laser light, optical ports are required, as well as an atom source of both species ^{87}Rb and ^{41}K.

The scientific payload, as well as the vacuum system, needs to be miniaturized and as light as possible. These physical requirements are given by the limits in length (3 m) and mass (340 kg) as derived from the launcher. The vacuum system as well needs to be able to withstand the mechanical loads throughout the whole mission and comply to the requirements considering the magnetic properties, which are further described below.

The flange and sealing connections are a crucial part of the vacuum system, since static and dynamic loads applied from the sounding rocket during flight could lead to leakages. Having a gas input into the vacuum system would increase the background pressure, which would lower the performance of the experiment due to more collisions with the residual gas. The MAIUS experiment sequences starts after the second stage burn out (T+44 s), and required a pressure level below 5×10^{-10} hPa within 19 s. During the launch and the two-stage burns of the rocket, vibrations of up to $17.7\,\mathrm{m\,s^{-2}_{RMS}}$ ($1.8\,\mathrm{g_{0RMS}}$) occur in a frequency range of 20 Hz to 2 000 Hz.

The choice of the material, as discussed in section 3.2, is another requirement which is derived from the experiment. The vacuum chamber where the experiment is performed, is located inside the Mu-metal shield of the PP subsystem (see section 5.4). To minimize the negative effects on the performance of the experiment, all vacuum parts inside the shield have to be made

of materials with low susceptibility. As stated in thesis [Gro16a], three main materials have been chosen; titanium (Ti6Al4V), aluminum (EN AW 7075) and OFHC copper. Although stainless steel is a commonly used material for vacuum parts, it should not be used inside the magnetic shield. For the PS which is outside of the shield, stainless steel (316L, 1.4404) is allowed.

It is also required that all vacuum components are cleaned in a defined procedure as explained in section 6.2 and assembled in an ISO 5 (RK100/RK1000) clean room to avoid contamination of the vacuum surfaces.

6.2 Design of the UHV System

In this section, the newly developed UHV system design of the MAIUS-B payload will be shown in detail, including the cleaning process and the vacuum preparation. The design overview will explain the new UHV design as well as the new vacuum components, as they were carried out throughout this dissertation. Additionally, the performed qualification tests of the PP including the UHV system will be discussed. In the last section, the lessons learned and observations from the MAIUS-B UHV system are stated and further discussed in respect to chapter 7.

6.2.1 Cleaning and Vacuum Preparation

All parts with surfaces facing into the vacuum need to be cleaned, in order to provide a sufficient pressure level and keep the contamination as low as possible. The cleaning procedure in MAIUS is defined into these five main steps:

- Step 1: General cleaning with Isopropyl and Acetone
- Step 2: Ultrasonic bath with water for 10 min at 80 °C

- Step 3: Ultrasonic bath with Isopropyl for 10 min at 40-50 °C
- Step 4: Ultrasonic bath with Acetone for 10 min at room temperature
- Step 5: Bake out in vacuum oven for 24 h at 200 °C

Following this procedure, contaminates such as waste lubricants can be significantly reduced, as well as high gas inputs due to outgassing effects into the vacuum chamber. The cleaning process decreases the gas input due to these effects, which increases the pump down speed and results in a better vacuum level.

The vacuum system is subsequently assembled inside an ISO 5 clean room (RK100/RK1000) to avoid recontamination of the vacuum surfaces. This was done for the MAIUS vacuum system (including the atom chip) in the clean room at the Laboratory of Nano and Quantum Engineering in Hannover.

Finally, the vacuum preparation starts with a combination of pumping down the system with a roughening pump, while baking out the system at the same time. By heating the system to a temperature of 80-100 °C, the amount of gas and water bound in the surfaces can be reduced. Although a higher temperature would further decrease the pumping and baking out time, the temperature maximum was limited by the atom chip. Nevertheless, the temperature ensures a fast removal of water from the walls inside the chamber.

As described in section 5.4, a two chamber design with a DPS in between is used for the experimental chamber. Since the effective cross section of the DPS is too small to provide any pumping through it, the roughening pump is connected to both ends of the system (pumping system and preparation chamber). The pump is connected to the system via two copper pinch-off tubes (CPOTs) which are pinched-off and thereby hermetically sealed by hydraulic jaws with 300 bar (30 MPa), which detaches the roughening pumps once the final pressure level is reached. During mechanical loads, valves have shown leakages, while the CPOTs have been proven to withstand vibration tests, as well as the MAIUS-1 flight. The process of detaching the pumps

is done once the roughening pump has reached its lowest pressure point at around 5×10^{-9} hPa, which takes 3-4 weeks. From this point on, the pressure is maintained and further reduced by the activation of two TSPs and one IGP. The IGP maintains this pressure and the TSPs are activated around four times a year until the launch campaign.

6.2.2 Design Overview

Although the design of the UHV system of the MAIUS-B payload is based on the heritage from its predecessor MAIUS-A, a major redesign was necessary in MAIUS-B. The redesign needed to combine all the features from MAIUS-A, but in a more compact way, which made essential design changes and developments needed. The new design and its implementation is shown in the following section, and is a main outcome of this thesis.

As described in section 5.4, the PP is divided into the EC, which is surrounded by the magnetic shielding (see figure 5.6), and the PS mounted on top of the base plate outside of the shielding. The PS has been separated from the EC to avoid negative impacts by electronic and magnetic stray fields originated by the IGP. The vacuum parts throughout the PS and EC are connected via a CF flange system as introduced in section 2.2.4. The general pumping concept to maintain the pressure, is realized by two TSPs and one IGP. One TSP and the IGP is located at the PS and functions as the main pumping system. Similar to MAIUS-A, the other TSP is directly placed on the mounting cube of the atom chip, as the amount of Teflon cables and materials used during the atom chip production have a high outgassing rate. As a countermeasure to the high outgassing rates as described in [Gro16a], the second TSP can be activated if needed to enhance the vacuum condition in the proximity of the experiment and the cold atoms.

Figure 6.1 shows the generated CAD model of the PS, as designed and implemented throughout this dissertation. It points out its main features and indicates the connection to the vacuum/experimental chamber. A newly

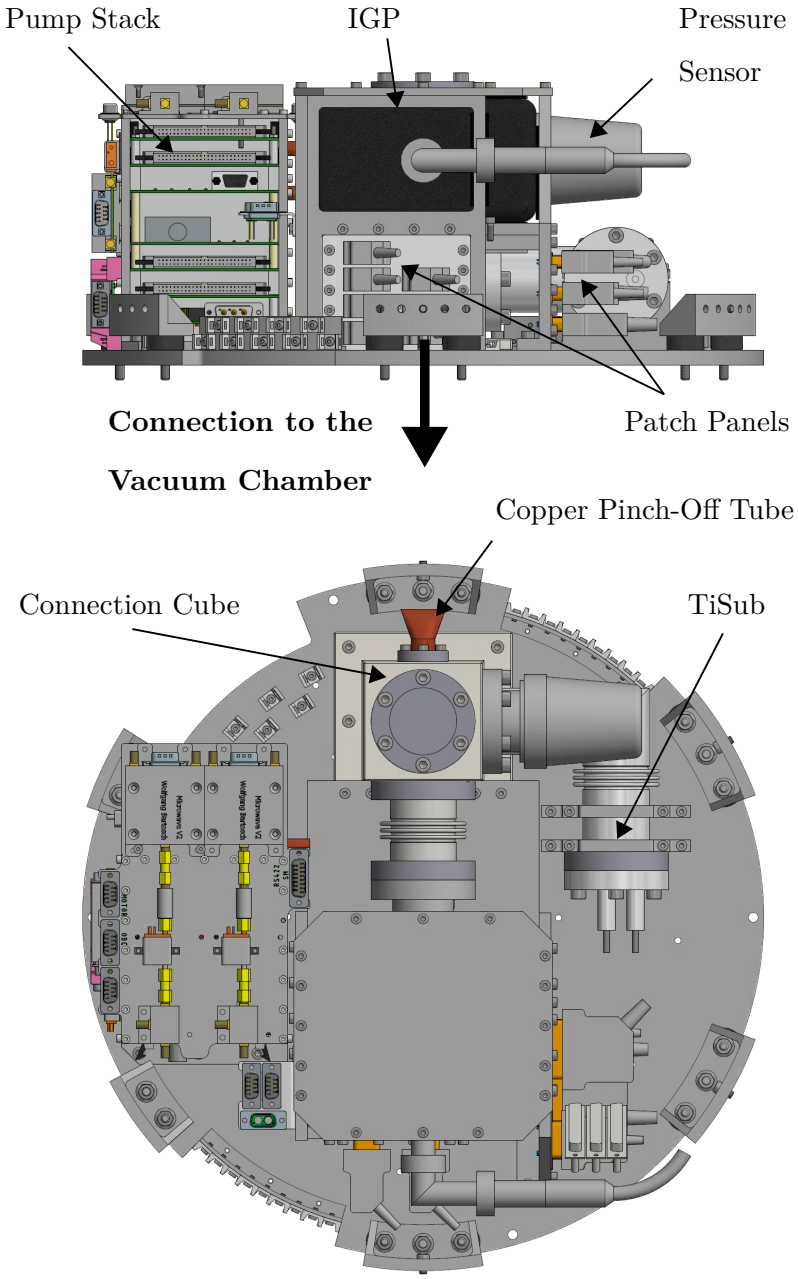

Figure 6.1: CAD-Model of the PS of the MAIUS-B PP, as designed and implemented within this thesis. For a better overview, certain connectors have been suppressed.

designed connection cube with several CF ports connects the TSP, the IGP, a cold-cathode pressure sensor (IKR270), the CPOT, and the connection to the vacuum chamber. The pump stack is equipped with the control electronics and the power supply of the IGP. It houses additional high power components and is therefore equipped with a heatsink in the back plate.

In MAIUS-A, the connection cube was placed in the middle of the base plate and the IGP was mounted in a 45° angle [Gro16b]. Within MAIUS-B, the connection cube was moved out of the center and the IGP was placed horizontally inside a newly designed mounting concept, which was an outcome of this thesis as described below. Due to this design change, the total height of the PS was reduced by 233.5 mm. With a mass of around 6 kg, the IGP is a comparatively heavy part which could lead to a high momentum on the CF connection. Therefore, a corrugated bellow is mounted between the IGP and the cube. This allows for minor movements during the load phase and reduces the leakage rate into the vacuum system. The IGP is placed on a mounting plate which is mounted on the one side to the cube. On the opposite side it is kept in place with a frame of side, top, and back parts mounted to the base plate. To fit in the power and data connections to and from the PP, the patch panels were designed within the mounting structure of the IGP. With rubber pads between the pump and the mounting parts, the IGP is pressed by the lid. An additional stringer under the pump strengthens the mounting plate. These modifications limit any significant movement of the IGP to avoid major leakages due to a high momentum on the CF connection during mechanical high loads.

All vacuum components of the PS, beside the connection cube, are made of stainless steel 316L (1.4404). To reduce the mass and ensure high stability, specifically on the CF knife-edges, the cube is manufactured of titanium grade 5 (Ti6Al4V). The TSP is connected via a CF DN40 flange and is designed in a 90° angle, mounted with two brackets to the base plate (explained in detail in section 6.2.3 and shown in figure 6.4). To avoid over-determination, the tube is equipped with a bellow to allow movement during mechanical loads and

to lower stress on the knife-edge and avoid leakages. The connection to the vacuum chamber is made by a CF DN16 tube, connected to the cube below the IGP base plate. It also has a 90° angle and is designed with a bellow to reduce the stress during loads on the connection to the vacuum chamber, and therefore to the chamber itself.

To comply with the requirement to use materials with a low susceptibility inside the magnetic shielding, the connection tube to the experimental chamber is manufactured of titanium grade 5. The chamber itself is designed in a two chamber design (see view A in figure 6.2), with the preparation chamber and the science chamber both manufactured of titanium grade 5. Since the chamber design is challenging from a manufacturing point of view, the two chambers had to be made separately. In the next step, the two chambers were brazed with a 100 µm thick foil made of pure silver. The EC was designed and tested in MAIUS-A, and the same chamber model has successfully flown during the MAIUS-A campaign. To fulfill the requirement of the accessibility for laser light, the same concept of the optical ports are used. For a full description on the design process, the qualification and the overall design, please refer to thesis [Gro16a].

Figure 6.2 shows the two chamber design with the preparation and science chamber, and the integrated DPS (see also section 6.2.3). View A in figure 6.2 shows the atom chip and the newly designed Rb and K oven, which are mounted with a CF flange to the preparation chamber. The mounting of the EC (see figure 6.2) was newly developed and implemented within this thesis, and thereby optimized compared to MAIUS-A to enhance the accessibility and improve the mounting concept for the optical detection systems. The chamber is mounted with a bracket to the base structure and to the atom chip cube. The cube houses the chip and several CF DN40 flange feedthroughs to supply and control the atom chip. A second TSP is mounted with a CF DN40 flange to the chip cube as mentioned above. The viewports of both chambers are made of BK7 glass which is sealed with a 1 mm indium wire as shown in figure 6.3. This allows the accessibility for the laser light and the

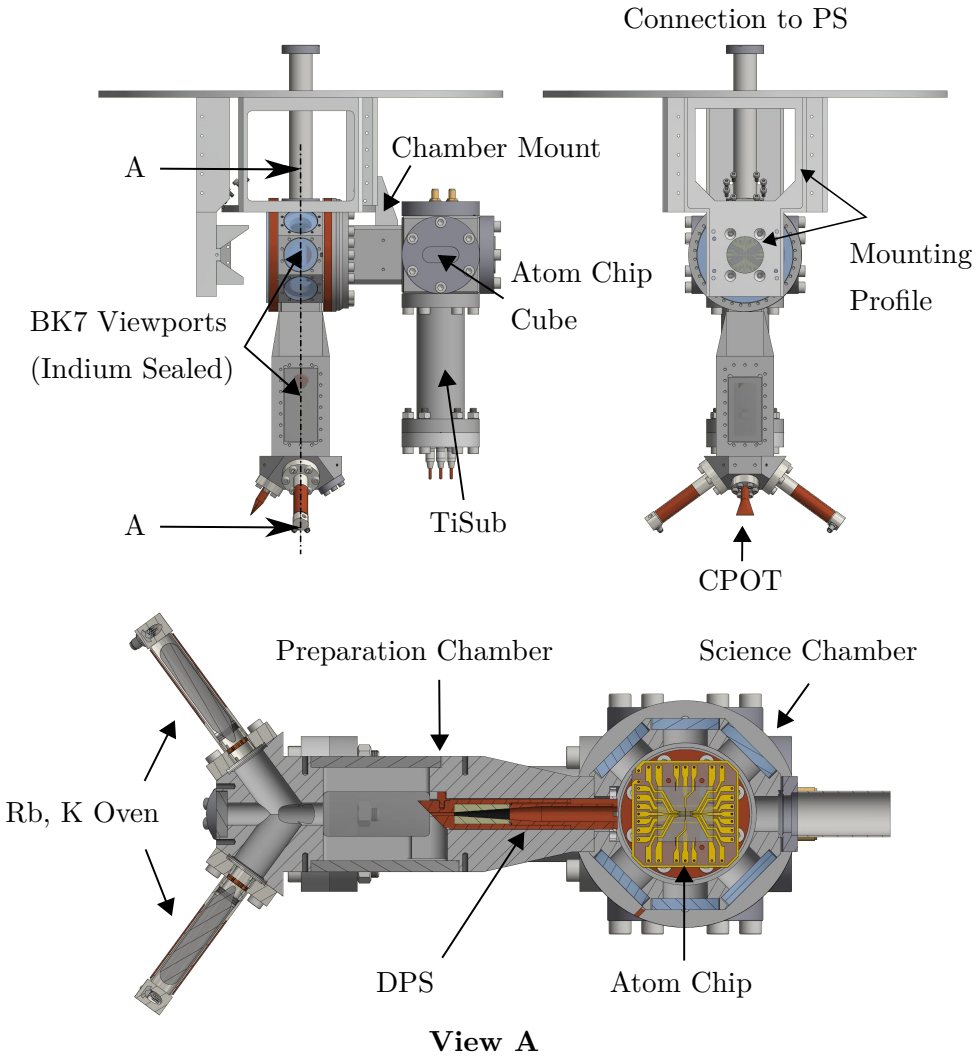

Figure 6.2: CAD-Model of the experimental chamber of the MAIUS-B PP. The detail view A shows the two chamber concept and the atom chip. The new oven and DPS are also shown, which were designed within this dissertation. For a better overview, certain connectors have been suppressed.

optical detection. The indium sealing concept with the BK7 windows allows a significantly smaller design of the overall chamber compared to standard CF flanges, and has been successfully tested and was flown in MAIUS-A.

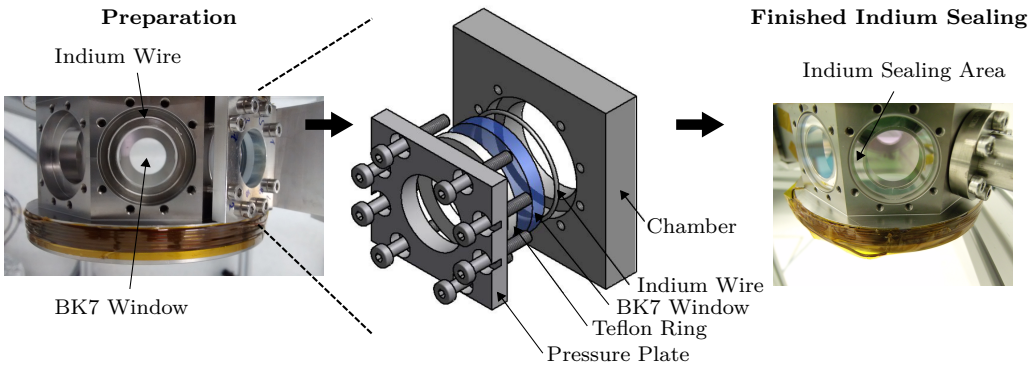

Figure 6.3: In the left picture the indium wire is shown with the BK7 window already lying on top before pressing. The explosion view in the middle gives an overview of the different parts involved in the sealing/pressing process [Gro16a]. In the right picture, the final pressed indium sealing area is shown.

It additionally gives more freedom in the geometry of the windows, such as in the preparation chamber, where the windows are square-shaped. During the integration process of the windows, the 1 mm indium wire is placed on the polished sealing surface. Afterwards, the window is pressed with a metal pressure plate and a Teflon ring to avoid scratches on the glass. The 8 screws are torqued in 0.1 N m steps to a maximum torque of 1 N m. The Teflon ring and the pressure plate are removed after at least one week. From that point on, the windows do not need any further support or treatment. On the right side of figure 6.3 the pressed indium sealing area is shown after the pressing process. After the pressure plate is removed, components like the collimators can be mounted by reusing the same holes around the windows.

6.2.3 Vacuum Components

In addition to the description of the overall design of the PS and the EC, the main vacuum components of the UHV system which were (re)designed and implemented throughout this thesis, will be explained in more detail.

Ion Getter Pump and Titanium Sublimation Pump

The pump concept is based on two TSPs and one IGP. Both pumps start working after the roughening pump is detached, and maintain the vacuum pressure from that point on. While both pumps are working together, only the IGP is able to pump noble gases. The working principals and the dependencies on the pressure and the saturation are explained in section 2.2.5.

In MAIUS-B, the IGP *VacIon 20 Plus* from *Agilent* provides a pumping rate of $25\,\mathrm{L\,s^{-1}}$ (unsaturated) and $15\,\mathrm{L\,s^{-1}}$ (saturated) for nitrogen at the operation pressure of 1×10^{-10} to $5 \times 10^{-10}\,\mathrm{hPa}$. The power connection, as well as the high voltage cable on the back of the pump as shown in figure 6.1, was redesigned and customized to a 90° angle throughout this thesis, to fit within the specific size constraints.

The TSP is made of three titanium-molybdenum filaments which are fed through a CF DN40 flange mounted to a CF DN40 tube. Figure 6.4 shows the two TSPs which are used in MAIUS-B. To comply with the material requirements inside the magnetic shield, the TSP at the atom chip cube was self designed in MAIUS-A and is also used in MAIUS-B. The TSP at the PS uses a standard *VG Sienta ST22*, but the filaments are modified by the supplier to be shorter [Gro16a; Sei14]. While the TSP at the PS itself is reused, the CF tube and the sieve concept was designed and implemented within this thesis.

As indicated in figure 6.4 and shown in detail in the top views, both TSPs are equipped with a sieve. In case of failure of the filaments, the sieve prevents floating fragments during the microgravity phase from entering the science

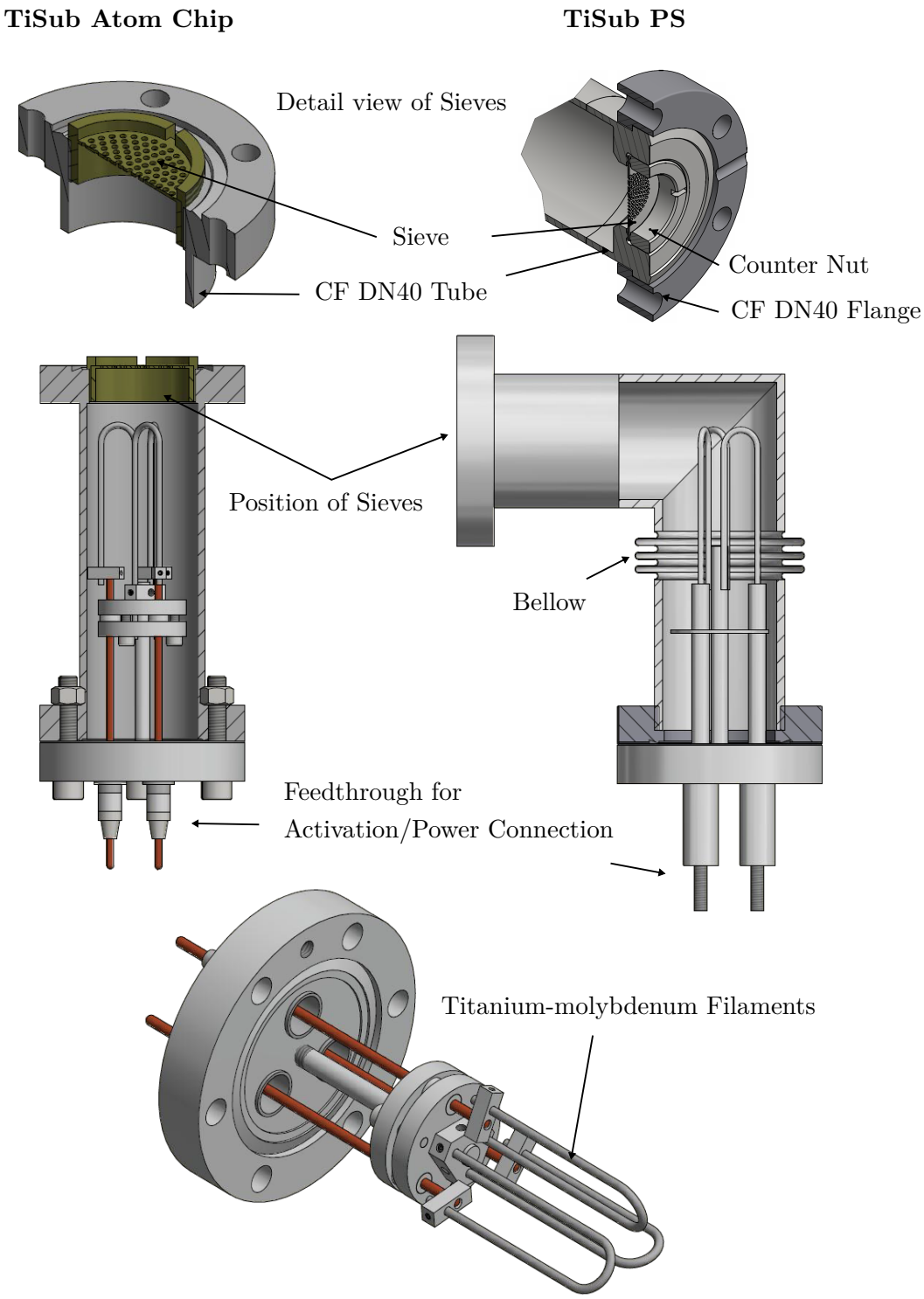

Figure 6.4: CAD-Model of the titanium sublimation pumps used in MAIUS-B. The left/bottom TSP is the one used at the atom chip cube [Gro16a; Sei14] and the right one is used in the PS and was redesigned within this thesis. The detailed views above show the sieves used to avoid debris in case of failure of the filaments during loads.

chamber and harming the experiment. For the activation, a current of 48 A is applied to one of the filaments. This will heat up the titanium-molybdenum filament to around 1 200 °C (1 473.15 K) and the titanium will sublimate and condense on the colder walls. This layer getters atoms of the remaining gas inside the UHV system. Although the mesh reduces the pumping speed significantly, calculations in MAIUS-A in [Gro16a] for a similar setup, showed an estimated pumping rate after the sieve in the region of 17-19 $\mathrm{L\,s^{-1}}$. The re-activation time of the TSP depends on the pressure level. Current laboratory operation showed that the TSPs need to be activated approximately every three months. Once the system is moved prior to launch and during the launch campaign, the activation will be done more frequently.

Differential Pumping Stage

A DPS is used in the vacuum chamber in order to keep a high partial pressure of ^{87}Rb and ^{41}K in the preparation chamber, and at the same time keep a low pressure in the science chamber. The DPS as a main feature of the vacuum chamber, was redesigned within the scope of this thesis. As a lessons learned from MAIUS-A, the chamber was modified for a better alignment and adjustment. Instead of screwing the DPS in via a thread, the thread was removed and the DPS was mounted with a counter nut on the one side and a pin on the other side. This prevents the DPS from turning and keeps it aligned. The modifications on the spare MAIUS-A chamber, reused for MAIUS-B, were realized with sinker electrical discharge machining. This technique avoids damage on the chamber, and is preferred because of manufacturing limitations with more commonly used techniques. In figure 6.5, a generated CAD-Model is showed with a cut view through the middle of the DPS.

The graphite tube is placed inside the front of the DPS and is kept in position by the back which is screwed into the front part. Its surface absorbs a high percentage of atoms when they are in contact with the graphite. As a new feature of the design, the counter nut and the pin keeps the DPS aligned within the chamber as shown in the detailed view A in figure 6.2. On the front

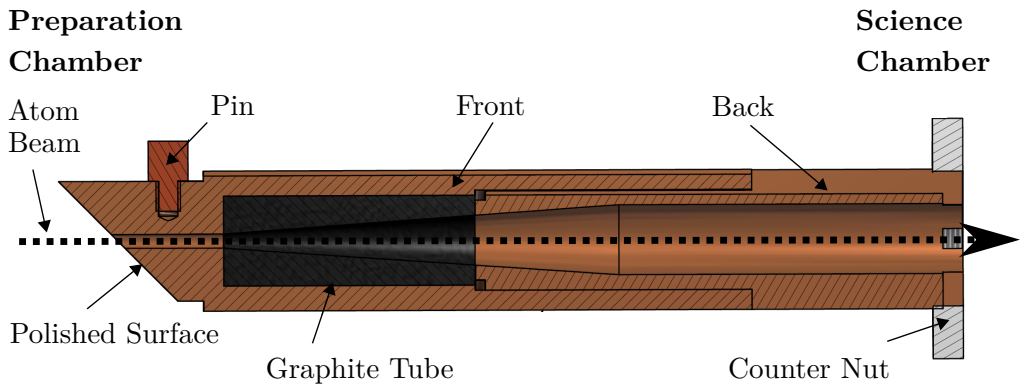

Figure 6.5: CAD-Model of the new DPS, as designed throughout this thesis.

part of the DPS, the surface is designed at a 45° angle and is polished for a better reflection. The polished surface is used in the experimental process and is further explained in [Gro16a; Sei14]. A concentrated beam of atoms, as indicated in figure 6.5, is injected into the small tunnel with the laser light from the preparation chamber, through the DPS, into the science chamber. This process is further explained in the scientific background in section 2.1.

Rb and K Oven

As an atom source for ^{87}Rb and ^{41}K, two ovens were newly developed within this dissertation, in a titanium tube connected via CF DN16 flanges. As shown in figure 6.6, a glass ampule with 1 g of ^{87}Rb (*Strem Chemicals 93-3736 Rubidium* 99.9 %) and 1 g of ^{41}K (*Strem Chemicals 93-1990 potassium* 99.95 %) per oven is placed inside. Once the vacuum system is pinched off from the roughening pump, the glass ampule is broken with a ring of four screws pressing from the outside on the titanium tube. To avoid glass fragments and to avoid the liquid Rb or K from floating around, a sieve is placed at the entrance of the tube. Depending on the pressure and the species, the oven needs to be heated. Heating is achieved with a heating wire coiled around the tube and connected to the plug at the end. Thereby, the vapor pressure can be tuned and adjusted according to the needs of the experiment. To provide

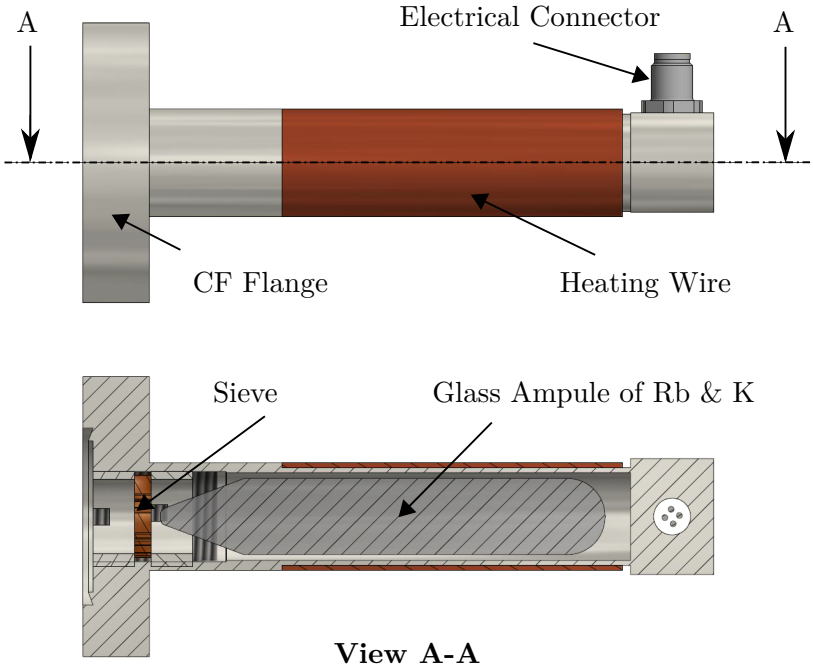

Figure 6.6: The generated CAD-Model of the new Rb and K oven design is shown. In detail view A, the inside of the design as carried out within this thesis is pointed out.

sufficient vapor pressure, the laboratory operation of the experiment shows that the Rb-oven can be kept at room temperature, while the K-oven is kept at around 46 °C.

6.3 Qualification of the UHV System

As discussed in section 6.1, a qualification of the payload is mandatory. In this section, the entire qualification process of the UHV system of the MAIUS-B payload will be discussed, as it was performed as a primary outcome of this thesis at the vibration test facility at the ZARM in Bremen. The contribution within this dissertation includes the test preparation, the actual conduction of the vibration tests, and the later presented discussion of the results for the tests of the PS and the PP. The three random vibration test levels stated in

Table 6.1: MAIUS random vibration test profile level with the power spectral density (PSD) and RMS values [Gro16a]. ($1\,g_0$=$9.81\,m\,s^{-2}$)

	Flight Level		**Acceptance Level**		**Qualification Level**	
Frequency	PSD		PSD		PSD	
Hz	$g_0{}^2$/Hz	$(m/s^2)^2$/Hz	$g_0{}^2$/Hz	$(m/s^2)^2$/Hz	$g_0{}^2$/Hz	$(m/s^2)^2$/Hz
20 - 400	0.000 3	0.029	0.002	0.192	0.004 5	0.433
400 - 600	0.004	0.385	0.03	2.887	0.067 5	6.496
600 - 1 300	0.000 3	0.029	0.002	0.192	0.004 5	0.433
1 300 - 2 000	0.004	0.385	0.03	2.887	0.067 5	6.496
RMS Value	$2.0\,g_0$	$19.6\,m\,s^{-2}$	$5.4\,g_0$	$53.0\,m\,s^{-2}$	$8.1\,g_0$	$79.5\,m\,s^{-2}$

table 6.1, are the flight, acceptance, and qualification levels, as derived from [Gro16a]. All critical components are tested, and hard mounted in all three axes, for a duration of 60 s. On a component level, the tests are performed at $8.1\,g_{0RMS}$ (qualification level). For the functional groups and on subsystem level, such as the PS and the PP, the flight ($19.6\,m\,s^{-2}{}_{RMS}$ / $2.0\,g_{0RMS}$) and acceptance ($53.0\,m\,s^{-2}{}_{RMS}$ / $5.4\,g_{0RMS}$) levels are tested. All tests were conducted in all three axes and the pressure was monitored. Before and after every random vibration test, a resonance sine sweep was performed from 5 to 2 000 Hz with a level of $2.45\,m\,s^{-2}$ ($0.25\,g_0$) and a sweep rate of 2.0 Oct/ min. Comparing the measured frequency responses of the test specimen during the two resonance runs, allows for screening of structural design flaws which occurred during the vibration test.

For the post-processing of the random vibration tests, the acceleration spectral density (ASD) response, and thereby the RMS values, are derived by several three axis acceleration sensors. These sensors are placed on positions of interest and additional control sensors are used as a reference.

The sensor placement for the PS vibration test is shown in figure 6.7, where the control sensor is used as a trigger signal for the pressure reading. In this figure, the IGP is shown with the sensor R3 placed on the top plate of the IGP mounting to monitor the behavior and the acceleration. The PS is mounted as it is in flight, with six brackets, including the vibration

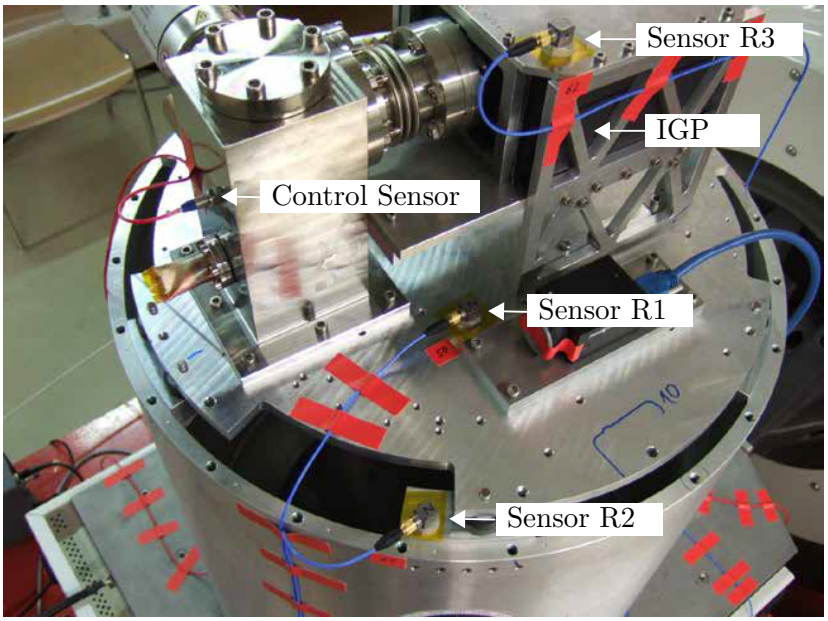

Figure 6.7: The test setup for the PS vibration test is shown. The Z-axis is, for all tests, in the axial direction with the X- and Y-axis in the radial plain. The control sensor is used as a reference for the pressure reading, and additional control sensors (not shown) are used as a reference for the applied accelerations without damping.

dampers, to a test hull segment. By this test setup, the actual damped accelerations at a specific point, such as the sensor R3, can be investigated and the impact of the vibration isolation is shown. The ASD of the PS which was tested at the acceptance level, is plotted in figure 6.8. The plots show the three tests in X-, Y- and Z-axis, and furthermore all three axes per test axis, which were monitored by the three axis sensor R3 at the IGP. The blue line indicates the test results, while the red line shows the applied random vibration level in the frequency range of 20 to 2 000 Hz. Additionally, the RMS acceleration level of the sensor response is shown for all nine tests. These acceleration values indicate that the vibration isolation by the dampers works well and the expected vibrations at the IGP are lower than the applied random level of $53.0\,\mathrm{m\,s^{-2}_{RMS}}$ ($5.4\,\mathrm{g_{0RMS}}$). The peaks at the lower frequency ranges (70-110 Hz) for the plots, where the test and sensor axis is aligned, are indicating the expected eigenfrequency of the dampers. At these points, the measured values exceed the applied acceleration (red line). However, the

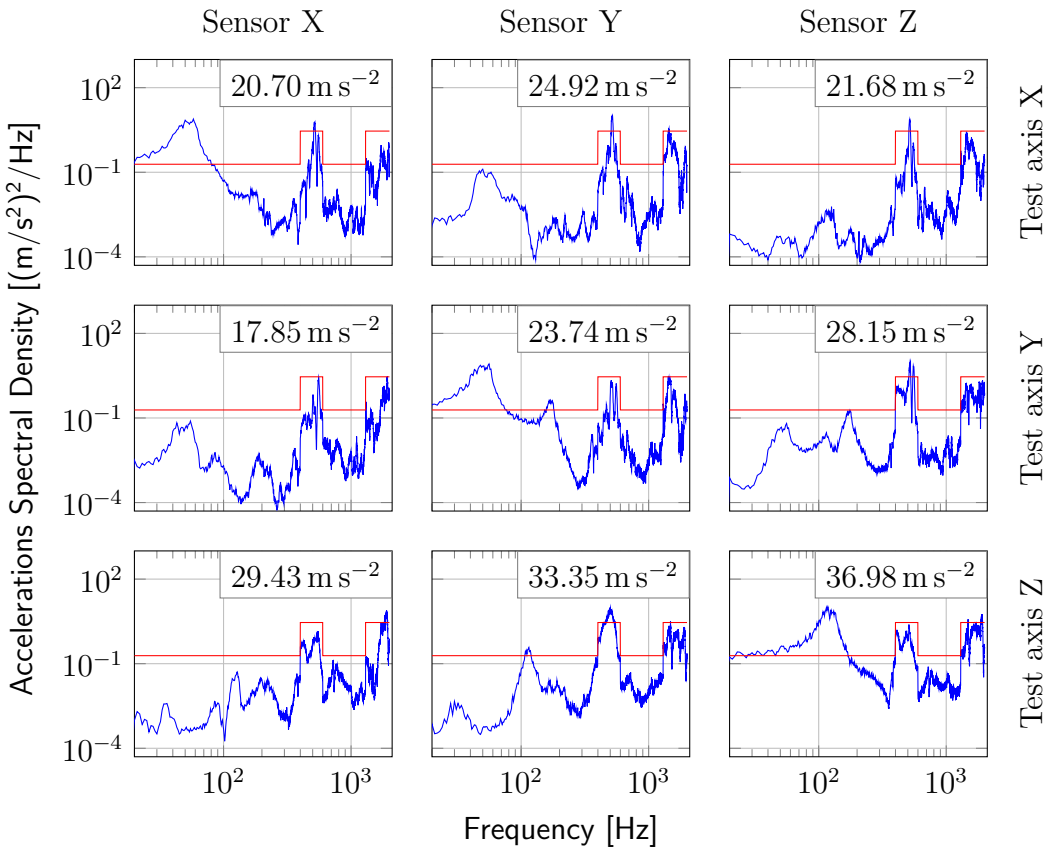

Figure 6.8: The plots show the ASD of the vibration test (acceptance level (53.0 m s^{-2}$_{\mathrm{RMS}}$ / 5.4 g$_{0\mathrm{RMS}}$)) of the MAIUS-B PS. The three-axis sensor (see sensor R3 in figure 6.7) was placed on the top of the mounting plate of the IGP. The system was tested in X, Y and Z axes, and for all tests, all three axes are plotted. By the red line, the applied acceleration of the test profile is shown. In each plot, the value from the sensor is shown, which states the actual RMS acceleration value. All tests are plotted over the frequency in the tested range of 20 to 2 000 Hz. (1 g$_0$=9.81 m s^{-2})

values above 110 Hz indicate a sufficient vibration isolation. In figure 6.9 the test setup for the PP and the sensor placement is shown. The TSP at the vacuum chamber is placed at the atom chip cube (see figure 6.2) and is only mounted at the cube and not further supported. Therefore, the sensor R2 is placed at the end of the TSP flange. On the top-right side of the image, sensor R3 is placed at the flange connection of the IGP. The test setup with the integrated test hull segment is shown, as well as additional sensors which

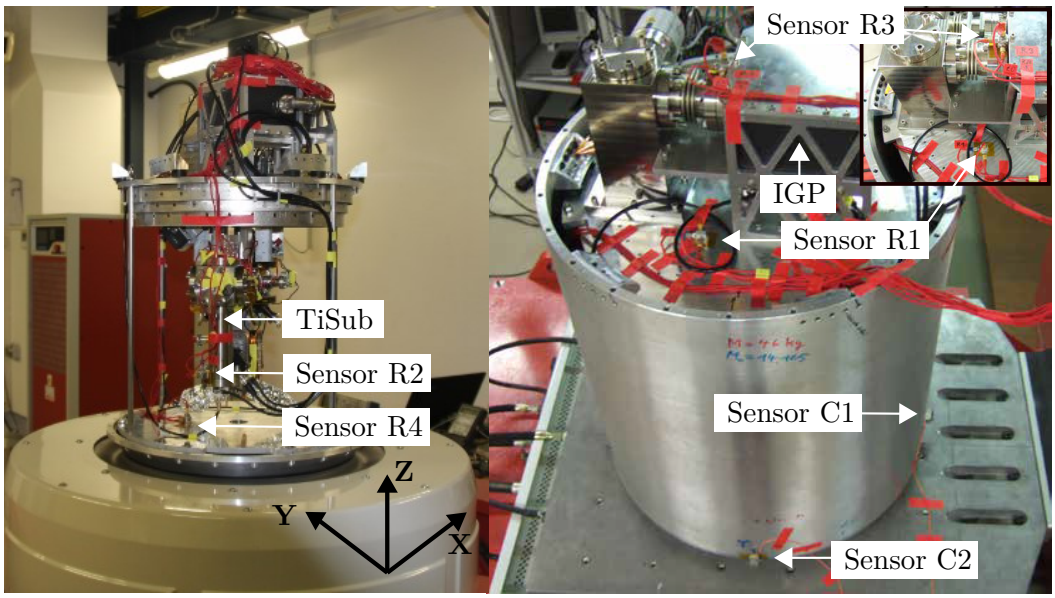

Figure 6.9: The test setup for the PP vibration test is shown above. The left image shows the Z-axis test configuration, where the PP is tested on the heat expander. In this image the hull segment used for the vibration tests is not yet mounted to show the three axis sensor positions on the lower ground plate R1, and at the end of the TSP R2. In the right image, the test configuration on the slip table is shown, which is used for the X- and Y-axis. It also shows the test hull segment with the two control sensors C1 and C2. It additionally indicates the positions of the sensors R1 and R3 on the PS section.

can be used as references. Figure 6.9 shows the test axis and the two test modes of the vibration test, with the payload mounted on the head expander for the test axis Z (left), and the X- and Y-axis on the slip table (right).

The RMS acceleration (g_{RMS}) for the tests of the PS and the PP in flight and acceptance level are presented in table 6.2. In this table, the response of the sensors R3 (at the IGP) for the PS test, the sensor R2 (at TSP), and R3 (at IGP flange) for the PP tests are shown.

These results indicate that the vibration isolation is working very well and that the actual acceleration level of crucial vacuum components, like the IGP or TSP, are significantly lower than the applied load level. However, one can see a difference between the sensors R2 and R3 of the PP test, which could be

Table 6.2: RMS accelerations response for the PS and PP tests in flight (F) and acceptance (A) level. For each test axis, all three axes per sensor are shown. For the PS test, R3 is located on top of the IGP (see figure 6.7). For the PP test, R3 is on the CF connection of the IGP and R2 is at the end of the TSP (see figure 6.9).

	Test Axis	Applied Load Level $m\,s^{-2}{}_{RMS}$	Sensor Axis X $m\,s^{-2}{}_{RMS}$	Y $m\,s^{-2}{}_{RMS}$	Z $m\,s^{-2}{}_{RMS}$
PS-IGP	X	19.6 (F)	8.53	10.79	9.52
(Sensor R3)	Y	19.6 (F)	7.46	10.40	12.36
	Z	19.6 (F)	10.99	13.64	15.21
PS-IGP	X	53.0 (A)	20.70	24.92	21.68
(Sensor R3)	Y	53.0 (A)	17.85	23.74	28.15
	Z	53.0 (A)	29.43	33.35	36.98
PP-TSP	X	19.6 (F)	7.06	3.14	2.06
(Sensor R2)	Y	19.6 (F)	5.49	5.79	2.45
	Z	19.6 (F)	4.71	5.89	6.57
PP-TSP	X	53.0 (A)	17.27	7.75	4.51
(Sensor R2)	Y	53.0 (A)	12.16	13.83	5.49
	Z	53.0 (A)	10.89	14.22	15.79
PP-IGP	X	19.6 (F)	9.52	2.94	6.57
(Sensor R3)	Y	19.6 (F)	9.71	8.83	6.97
	Z	19.6 (F)	11.67	7.95	11.77
PP-IGP	X	53.0 (A)	24.53	7.06	15.89
(Sensor R3)	Y	53.0 (A)	22.76	21.78	16.48
	Z	53.0 (A)	28.35	18.84	28.65

caused by a different structural damping effect. Nevertheless, these differences are expected due to the different mounting concepts.

As mentioned above, a sine resonance sweep was performed before and after each test and the results were compared. For all tests, the comparison showed no significant differences, especially for the resonance case which indicates the structural integrity of the overall design. The comparison for all sensors shown in figures 6.7 and 6.9 were taken into account.

For the final qualification of the vacuum system in MAIUS-B, the pressure was monitored for both tests. As a requirement described in section 6.1, the pressure should be below the threshold of 5×10^{-10} hPa approximately 19 s after the load phase (stage burn out). At this time of the mission, the attitude control system has orientated the experiment into position and the test sequences starts. Although the pressure will rise during the load phase by the stage burn of the rocket, the system needs to be able to maintain itself as fast as possible to perform as planned. A higher background pressure will lower the atom number due to collisions with the remaining gas as explained in section 3.2, and will decrease the performance. Therefore, it is important to test the influence of the load phase, as well as the maintaining phase afterwards.

In figure 6.10 the test results of the pressure readings for all tests, in all three axes, for the PS and the PP test are shown. The orange line indicates the flight level test and the blue line shows the acceptance level. By the gray area, the load phase of 60 s is highlighted. The horizontal black dotted line marks the threshold of 5×10^{-10} hPa and the vertical green dotted line marks the start of the experimental sequences. Figure 6.10 indicates that the pressure for the PS and the PP test in X- and Y-axis for both load levels are below the threshold within several seconds. For the Z-axis test, both plots are showing higher pressure values during the load phase compared to the X- and Y-axis tests. This results in a higher gas input into the system and increases the maintaining time of the vacuum system significantly. For the acceptance level test, the vacuum system was not able to maintain the pressure within 19 s. This shows that the impact of vibrations in this test axis are significantly higher. Although it is not possible to detect the final cause of this behavior, the most likely cause is the IGP, with its high mass and the TSP which are both connected with a CF flange connection. Since the vacuum system was fully sealed with a pressure of around 2×10^{-10} hPa, it can be assumed that none of the manufactured vacuum components have a manufacturing flaw, which could have caused the leakages. This indicates that the pressure rise is originated by a leakage rate through the CF flange connections, and shows their significant impact on the overall performance of the UHV system.

All three axes were tested shortly after each other, starting with the X- and Y-axis. At the time the Z-axis test was performed, the UHV system had already been tested twice within a short period of time. This led to a higher initial pressure (about 1×10^{-10} hPa above the tests in X- and Y-axis) prior to the test of the Z-axis. It is most likely that a combination of the above discussed aspects caused the higher pressure and the longer pressure maintaining time during the Z-axis test. Nevertheless, the important value for the qualification of the UHV system is the flight level, which has been set (including an additional margin) close to the actual maximum load level (see 3.1.1) during a sounding rocket flight. The pressure of the PP test for this level complies with the requirement. It is also worth mentioning that the current pressure of the UHV system after several months of operation is at 2×10^{-11} hPa. This is one order of magnitude better than the initial pressure before the test. This will have a positive impact on the behavior of the UHV system during the flight. Hence, the PP with its UHV system of the MAIUS-B scientific payload, has passed the qualification process performed throughout this thesis, which marks an important milestone within the MAIUS mission towards the launch.

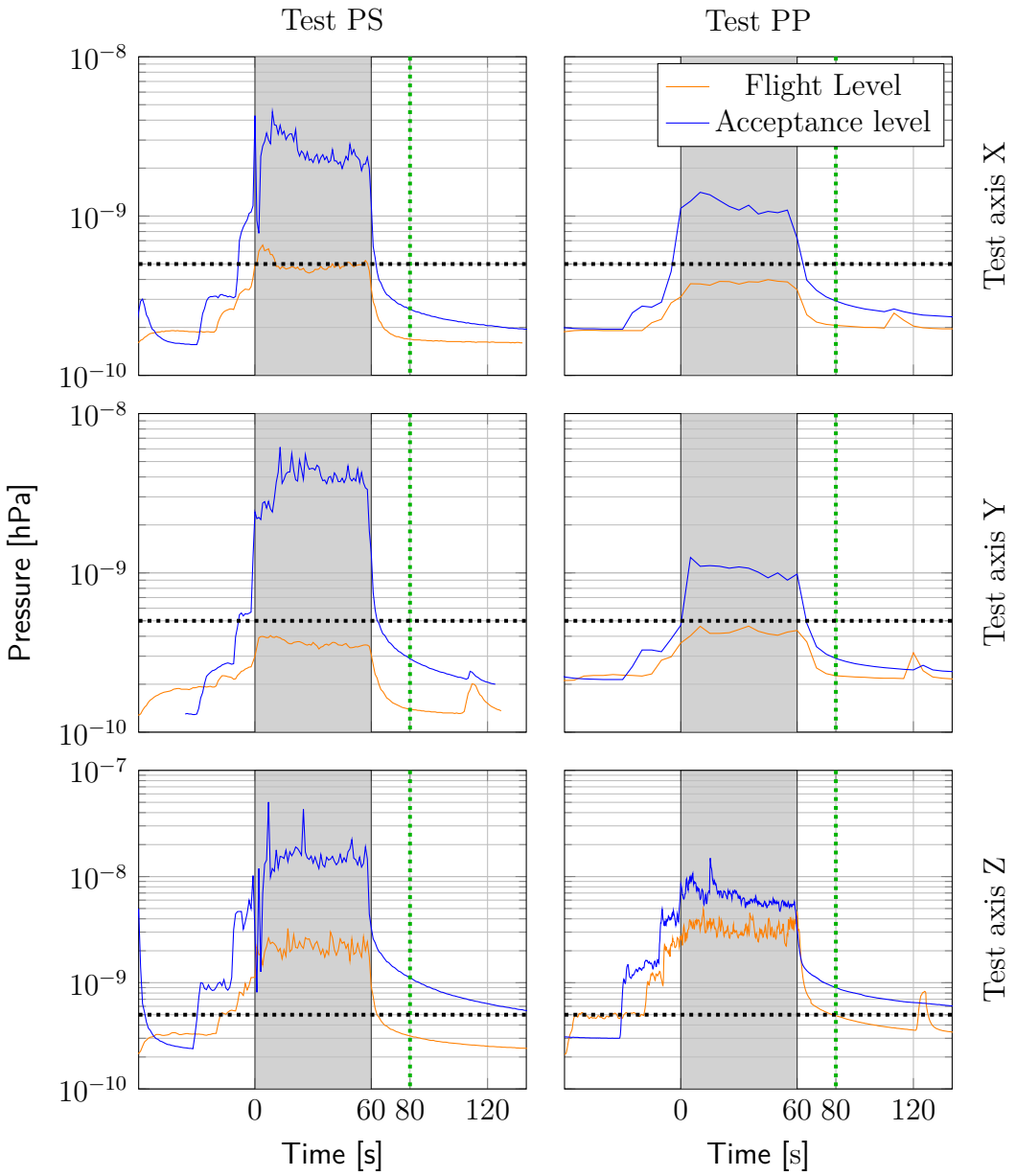

Figure 6.10: The plots show the pressure readings during the random vibration tests for the PS and the PP. All tests were performed, in all three axes, in flight ($19.6\,\mathrm{m\,s^{-2}_{RMS}}$ / $2.0\,\mathrm{g_{0RMS}}$) and in the acceptance ($53.0\,\mathrm{m\,s^{-2}_{RMS}}$ / $5.4\,\mathrm{g_{0RMS}}$) level. The gray area indicates the test duration of 60 s. The black dotted line shows the pressure value required by the experiment $\leq 5 \times 10^{-10}$ hPa. Approximately 19 s after the load phase (stage burn out) the experimental sequence starts, which is indicated by the green dotted line in the plots.

6.4 Observations and Lessons Learned

During the laboratory operation and the vibration tests, several observations and lessons learned were derived. After several months of laboratory operation of the PP, a constant pressure level of around 2×10^{-11} hPa was observed. This indicates that the MAIUS-B pumping system is working well and is able to achieve pressure levels more than one order of magnitude better than required ($\leq 5 \times 10^{-10}$ hPa). In the laboratory operation, in a temperature controlled room at 23±1 °C (296.15±1 K), an activation of the TSPs every three months, with a constant IGP operation, is sufficient to keep the pressure level as mentioned above. Due to a failure of the air conditioning system in August of 2020, the temperature of the vacuum system was rising up to around 35 °C (308.15 K) which led to a pressure of up to 4.5×10^{-10} hPa. Once the air conditioning system was running again, the TSPs were activated more frequently and the vacuum level was able to maintain itself again at the initial pressure region of 2×10^{-11} hPa. This shows the significant impact of the ambient temperature on the vacuum level. However, the temperature inside the final integration room is at 20±5 °C (293.15±5 K) and the launch tower is controlled to be at 17±7 °C (290.15±7 K) prior to launch (see section 3.1.1), which will have a positive impact on the vacuum level. The vacuum level prior to launch is therefore expected to be in the order of 2×10^{-11} hPa.

The vibration tests, as discussed in the previous section, clearly state the impact of mechanical loads on the pressure of the UHV system of the MAIUS-B payload. As shown in figure 6.10, the dynamic loads during the vibration tests lead to a gas input into the system and to a higher pressure. The qualification process is considered to be passed, although some lessons learned are derived from the tests.

While the expected pressure (2×10^{-11} hPa) is one order of magnitude better than the initial vibration test pressure, the transport to the launch site, the final integration, and movements of the payload prior to launch might lead to a higher initial pressure. In order to achieve an initial pressure as low as

possible prior to the launch, the two TSPs of the MAIUS UHV system should be activated as close as possible to the launch. The activation will provide a higher pumping rate during the flight. This will have a positive impact on the pressure, and the pressure maintaining time of the vacuum system, after the load phase towards the start of the experimental sequences.

The design process of the vacuum system is another important lesson learned from the qualification process. Any major design changes of the final integrated and pumped down vacuum system, will lead to significant time delays in the range of six to eight months (depending on the project). This delay is caused by the long vacuum preparation time and the complex assembly of the vacuum system. Such a major design change will consume time and financial and human resources, which are all limited factors for every project. In figure 6.10, it was indicated that mechanical loads have a significant impact on the system. This is mainly caused by leakage rates which occur at the CF flange connections during mechanical loads. As the CF flange connections are the driven cause of leakages, it is important to further investigate the CF flange connections under external loads. Since major design changes are still comparatively easily achieved during the design phase, the influence of mechanical loads on critical CF connections should be considered at this point, which is one of the main lessons learned for future designs of space-borne UHV systems. However, there were no tests or literature data available for the influence of CF connections under static loads. As a main part of the scope of this thesis, the next chapter presents the first experimental investigations for CF connections under static loads, as they appear by the acceleration during the rocket launches.

7 Investigation of CF-Flange Connections under Mechanical Loads

One of the main components for the design of UHV systems for multiple ground and space based experiments, is the CF connection. A CF flange connection is a widely used COTS connection system. As further explained in section 2.2.4.1, the sealing principle is based on an OFHC copper ring gasket, which is pressed with screws in between two flanges. In the sealing process, the tightening torques and the bolt pretension of the mounting screws are used to press the knife-edge into the softer copper gasket. This results in deformations of the copper gasket. As such, the softer copper seals any fine surface irregularities on the knife-edge. The CF flange produces a UHV sealed connection with leakage rates of less than $1 \times 10^{-12}\,\mathrm{Pa\,m^3\,s^{-1}}$ [VAC20a].

As mentioned in section 2.2, the final achievable pressure of a UHV system is an equilibrium between the pumping speed on the one side, and the outgassing and leakage rate on the other side. For a spaceborne quantum optical experiment, such as MAIUS or BECCAL, a residual pressure of less than $5 \times 10^{-10}\,\mathrm{hPa}$ is required within the vacuum system. To be able to comply with this requirement, and to achieve this pressure level, conditions during the space mission flight need to be taken into account. One of the main impact factors for a UHV system on a rocket are the mechanical loads, such as vibration or static loads by accelerations.

In the previous chapter, the vibration tests of the MAIUS-B UHV system were presented. One of the observations during the vibration tests of the MAIUS-B vacuum system, is the pressure increase caused by dynamic loads (vibrations). This increase is caused by a leakage rate, which occurs at the CF flange connections, as all other parts are fully sealed. While the impact of the dynamic loads on the UHV system and the CF connections are tested during the qualification process and certain data is existing, the static loads are not further tested. Data on the leakage rate of CF flanges caused by static loads is extremely useful to improve the design process and avoid high leakage rates and a higher pressure level. A pressure rise has a direct impact on the performance of the quantum optical experiment, as indicated in chapter 3. It also makes it possible to optimize, as well as improve, the assembly process for future space missions. Nevertheless, there is no data available for the leakage rate of CF connections. As a primary outcome of this thesis and presented throughout this chapter, a new leakage rate test setup was developed and built. The results of the performed tests are discussed and the findings throughout this dissertation are summarized. These results provide the science community with the first set of data for the leakage rate of CF connections under static loads.

The tests presented in this chapter investigate the influence on several parameters of the CF flange connection. For the optimization and the improvement of the assembly procedure, the influence of the tightening torque is tested. The lightweight material aluminum (*AluVaC®*, similar to 6082 AW) is investigated, as well as the standard material stainless steel (316LN-ESR, 14429-ESU). In addition, the connection between two different materials, stainless steel and aluminum, is investigated. The last test parameter is the copper gasket, where an annealed or a non-annealed copper (OFHC) gasket is used.

In the first section of this chapter, the expected loads for different space missions are stated. As an outcome of this thesis, the next section introduces the newly designed and implemented leakage rate test setup and methodology,

considering the previously stated test requirements. Prior to the discussion of the results, the data post-processing and the test uncertainties used within this dissertation, are explained. The results of the leakage rate tests, for the different CF flange materials (aluminum [*AluVaC®*], stainless steel [316LN-ESR, 14429-ESU]), copper gaskets (annealed, non-annealed) and tightening torques (10 N m, 12.5 N m, 15 N m) are discussed. In the last section, the findings of the performed leakage rate tests of CF flange under static loads are compared and summarized. This gives the first data set on the influence of static loads on the leakage rate for CF connections, which can be used to optimize the design and assembly process for space suitable UHV systems.

7.1 Expected Static Loads for Space Missions

This section shows the expected static loads during different types of rocket missions. The focus here is on sounding rocket missions such as MAIUS and the static loads during a launch of the *SpaceX* Falcon 9 rocket.

During the ascent of the MAIUS-1 mission, the accelerations were measured by an inertial measurement unit, within the MORABA service module. Figure 7.1 shows the accelerations in longitudinal and lateral direction, with a maximum peak of 121.6 m s^{-2} (12.4 g_0) at 34 s within the longitudinal axis. These values are similar to the expected accelerations during the MAIUS-2 and MAIUS-3 flights.

Throughout a launch of a Falcon 9 rocket, the payload is either hard mounted or soft stowed. Although the actual acceleration data for most space flights are export controlled, the published data of the interface definition document of the company *Nanoracks* can be taken as an example [Gre20]. The presented accelerations can be interpreted as a flight with a Falcon 9 rocket on a supply mission to the ISS. Table 7.1 summarizes the maximum accelerations in all three axes, which are applicable for a hard mounted and a soft

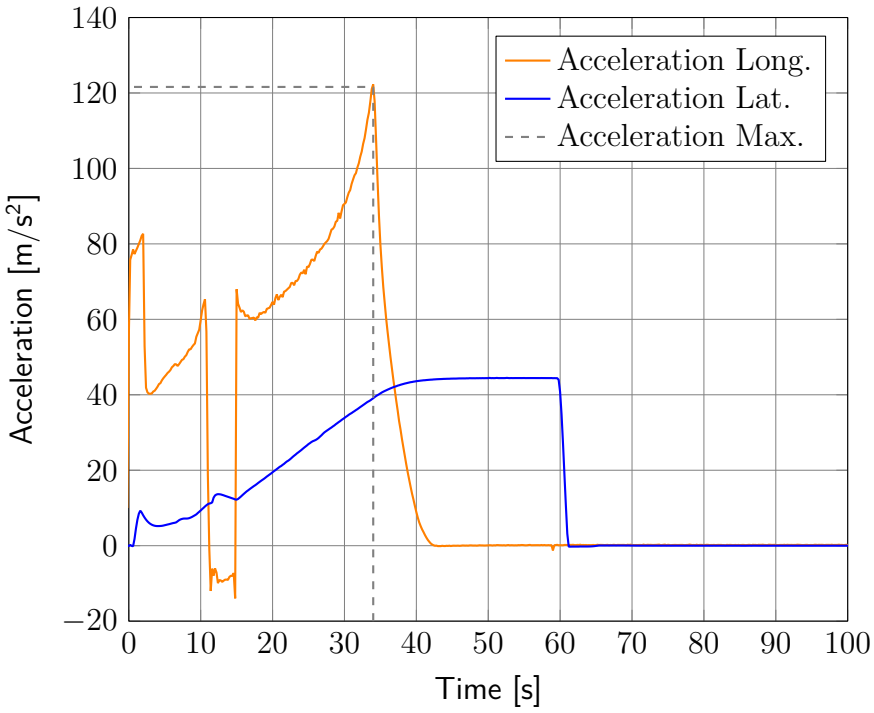

Figure 7.1: The plot shows the accelerations in longitudinal (blue line) and lateral (orange line) direction, for the ascent of the MAIUS-1 sounding rocket mission. The maximum peak during the rocket ascent shows an acceleration of 121.6 $\mathrm{m\,s^{-2}}$ (12.4 $\mathrm{g_0}$) at 34 s within the longitudinal axis. (1 $\mathrm{g_0}$=9.81 $\mathrm{m\,s^{-2}}$)

stowed payload. However, the payload shall include an additional margin of safety [Gre20].

Table 7.1: Accelerations (static) loads during the launch and landing of a Falcon 9 rocket [Gre20]. (1 $\mathrm{g_0}$=9.81 $\mathrm{m\,s^{-2}}$)

	Acceleration x-axis in $\mathrm{m\,s^{-2}}$	Acceleration y-axis in $\mathrm{m\,s^{-2}}$	Acceleration z-axis in $\mathrm{m\,s^{-2}}$
Launch	± 68.7	± 39.2	± 39.2
Landing	± 91.23	± 17.7	± 17.7

7.2 Experimental Leakage Rate Test

A main task within this thesis is the design and implementation of a new leakage rate test setup. The following sections discuss the test requirements, the newly designed and implemented test setup, and the used methodology as it was carried out within this dissertation.

7.2.1 Test Requirements

The leak detector *ASM 340* by *Pfeiffer Vacuum* is used throughout the tests conducted in this thesis. Helium-4 (^{4}He) is used as tracer gas for the leakage detection. One of the main requirements is to avoid a helium contamination of the air around the leakage detector. This is important, since the leakage detector is not perfectly helium sealed and accumulates helium from the surrounding air over time. Such a contamination can significantly increase the ground value of the measured leakage rate over time, and therefore increase the lowest detectable leakage rates. This lowers the overall performance of the test setup and limits the possible detectable leakage rate.

For a reproducible test environment, the test should be performed inside a test chamber, which is capable of being evacuated down to approximately 1×10^{-1} hPa and pressurized with helium of up to 1 200 hPa. The chamber should be evacuated by a backing pump, and then flushed and pressurized with helium to produce a pure helium atmosphere, detected via a pressure sensor. This enables a controlled, repeatable and reproducible test environment for all tests.

The test setup needs to be accessible for power, sensor connections, the connection of the leakage detector, a pump connection, and the helium inlet. This accessibility needs to be realized by vacuum suitable feedthroughs, to minimize possible helium contamination of the surrounding air.

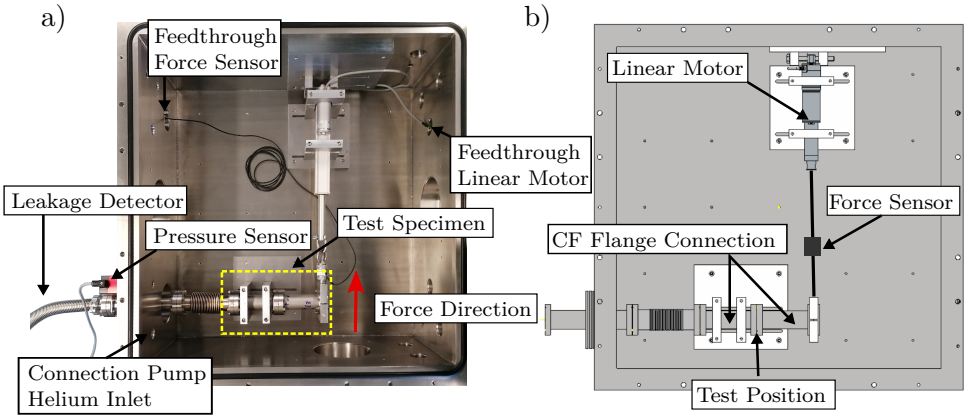

Figure 7.2: The experimental test setup for the leakage rate test under static loads is shown. Figure b) (CAD-Model) shows the linear motor, the force sensor and the CF flange connection with the test position. Figure a) of the actual chamber, shows the feedthroughs for the pressure sensor, the linear motor control, the force sensor, and the connection for the helium inlet as well as the connection to the leakage detector. The red arrow indicates the force direction. In the yellow dotted box is the position of the test specimen (see also figure 7.3a), and the connection to the linear motor [Els21].

The static loads should be applied with a linear motor, which needs to be usable under low vacuum conditions (down to 1×10^{-1} hPa). The linear motor has to be controllable from the outside and adjustable via its power supply, with a force sensor as the feedback signal for the static load. The force sensor should have a minimum of connecting pieces to avoid unwanted deformations. The general structural design of the mounting brackets of the linear motor, and the test specimen, should be adjustable to align the force application. The design of the mounting brackets should have a sufficient stability to remain in position, avoid deformation, and minimize any movement under static loads.

7.2.2 Test Setup

To comply with the requirements to provide a controlled, repeatable and reproducible test environment, and at the same time minimize the contamination of the leakage detector, the experimental setup is built inside a vacuum

chamber as shown in figure 7.2a. The leakage detector is connected via a flexible CF hose to a CF DN40 feedthrough, which is connected inside the chamber to the test specimen (yellow dotted box in figure 7.2a). The initial evacuation of the chamber and the flushing with helium is realized by a three-way valve, connected via a feedthrough. The three-way valve connects the chamber with a backing pump for the evacuation. To flush it with helium, the valve position is switched and the chamber is connected via a pressure regulator to the helium reservoir.

The force (red arrow in figure 7.2a) is applied to the test specimen with a linear motor (*Model DLB-12-50-A-200-HS2-IP65* by *Transmotec*), which is mounted with brackets on the chamber bottom and to the back wall. This mounting concept disables the linear motor from movements and keeps it in position, when the force is applied. A feedthrough connects the linear motor with an adjustable power supply. Additional feedthroughs connect the pressure sensor (*Model PCR280* by *Pfeiffer Vacuum*) and the force sensor (*Model KM30z-2KN* by *ME-Meßsysteme*) for the data acquisition. The force sensor is able to measure up to 2 000 N and is mounted in between the linear motor arm and the mounting bracket at the free end of the test specimen, as shown in figure 7.2b. The measured force is used as the control variable and the feedback signal for the linear motor control.

A simplified schematic model of the CF flange connection (test specimen) is shown in figure 7.3a. For the test specimen, two standard CF DN40 tubes are used, each with a total length of 126 mm from end-to-end. The test tubes are connected with six M6 screws (including washers) made of stainless steel A2-70 and standard plate nuts. This combination and type of screw is commonly used throughout UHV systems and was therefore chosen for these tests. The left side of the test specimen is mounted with brackets (fixed support in figure 7.3) to the chamber floor. For the static load tests of the CF connection, a force is applied by the linear motor at the free end of the test specimen. This leads to a momentum on the CF knife-edge connection, which could result in a gap at the copper gasket and thereby a leakage. Figure 7.3b shows the

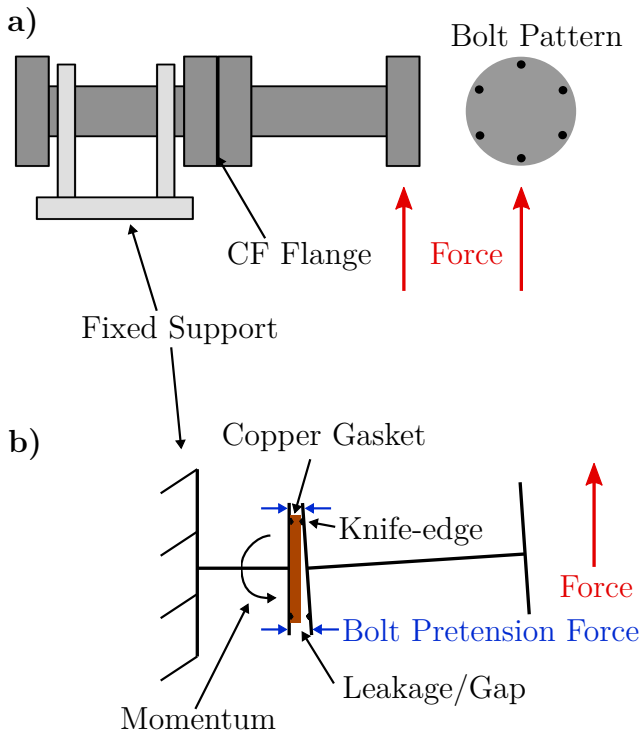

Figure 7.3: Figure a) shows the test specimen, consisting of a CF DN40 tube connection, fixed on one side, with the force applied at the end of the second tube. On the right side, the CF flange bolt pattern is shown in respect to the applied force. Figure b) shows a simplified model of the CF flange connection, including the bolt pretension force by the mounting screws, the knife-edge, the copper gasket, and the momentum induced on the CF connection by the applied force. It indicates the moment of failure, when the force on the CF flange connection is high enough to cause a gap and thereby a leakage [Els21].

point of failure of the CF knife-edge/gasket connection, when the upper part of the CF connection is pressed into the copper gasket and the lower part of the knife-edge is spread from the gasket. At this point, the deformation of the CF flanges and the CF connection bolts is big enough to cause a gap despite the bolt pretension force. Such a gap will result in a pressure rise of the vacuum system. This shows that the bolt pretension force and the tightening torque of the screws of the CF flange connection have an influence which needs to be investigated.

To ensure reproducibility, all the test specimens are assembled by the same mounting procedure. Only new pristine CF tubes (knife-edges) are used, which prevents interference behavior of the knife-edge due to previous use or damage. After the initial assembly of the tubes, with the copper gasket in between, the six screws are tightened by hand. All screws are torqued following a star pattern, to ensure an equal tightening of the CF connection and avoid negative settling effects. After one or two intermediate torque steps, which are not further defined, the final bolt pretension torque is applied. In the last step, the screws were torqued again with the same star pattern and the same torque to take settling effects into account.

7.2.3 Methodology

Throughout all the tests, stainless steel A2-70 screws in M6 are used for the CF DN40 flange connections. Without lubricant on the nuts and the screws, the coefficient of friction is between 0.2 to 0.35 and is assumed to be 0.3. This results in a tightening torque of 10.4 N m for M6 stainless steel A2-70 screws [Wü22]. Therefore, 10 N m is tested to investigate the influence of the tightening torque on the leakage rate during static loads. Additionally, 12.5 N m and 15 N m tightening torques are tested, to investigate the impact of a higher tightening torque on the leakage rate.

Stainless steel (316LN-ESR, 14429-ESU) and aluminum (*AluVaC®*) material for the CF tubes are tested. While stainless steel is a commonly used material for UHV components, aluminum is of interest because it has around a three times lower density (see table 2.2 in section 2.2.4.2). The light weight of aluminum makes it interesting for space missions, where a compact and low mass design is one of the main design drivers. In addition, aluminum has a sufficiently low magnetic permeability, which is one of the requirements of a cold atom interferometer for future space missions.

The *AluVaC®* components require an annealed copper gasket, used for all tests where aluminum is involved. To investigate the impact of the copper

Table 7.2: List of leakage rate test series performed throughout this thesis, with the different materials, tightening torques, and the gasket treatment of the tested CF flange connection. The name of the test series, such as 316AluCUA, indicates the material and if the used gasket is annealed (CUA) or non-annealed (CU).

Test Series	Material Test Tube 1	Material Test Tube 2	Gasket Treatment	Tightening Torque in N m
1 - 316316CU	316LN-ESR	316LN-ESR	non-annealed	10, 12.5, 15
2 - 316316CUA	316LN-ESR	316LN-ESR	annealed	10, 12.5, 15
3 - AluAluCUA	*AluVaC®*	*AluVaC®*	annealed	10, 12.5, 15
4 - 316AluCUA	316LN-ESR	*AluVaC®*	annealed	10, 12.5, 15

gasket for a stainless steel (316LN-ESR, 14429-ESU) CF connection, annealed and non-annealed copper gaskets are tested. In addition, a mixed flange connection with stainless steel and *AluVaC®* tubes is tested. Table 7.2 summarizes the different tests which have been performed throughout this thesis and will be discussed in the following sections.

All tests are based on an integral leakage rate test method, following the same test procedure as shown in Figure 7.4. For this test method, the test specimen is placed inside the test chamber which is filled with helium. The leakage detector is connected to the test specimen as shown in figure 7.2a, and constantly measures the leakage rate during the tests.

Prior to the tests, the chamber is evacuated by the backing pump to a pressure of around 1×10^{-1} hPa. In the second step, the three-way valve is switched to the helium reservoir to flush the chamber. The initial evacuation ensures a pure helium atmosphere inside the chamber and avoids mixing effects with the air. The chamber is filled to a pressure of 1 100 hPa for all tests. The leakage rate is monitored and a rise would indicate a leakage of the setup, which would need to be further investigated before the test can start. If the leakage detector shows no leak, a wait time of $\geq$10 min is held to measure the ground value (base value) of the leakage detector.

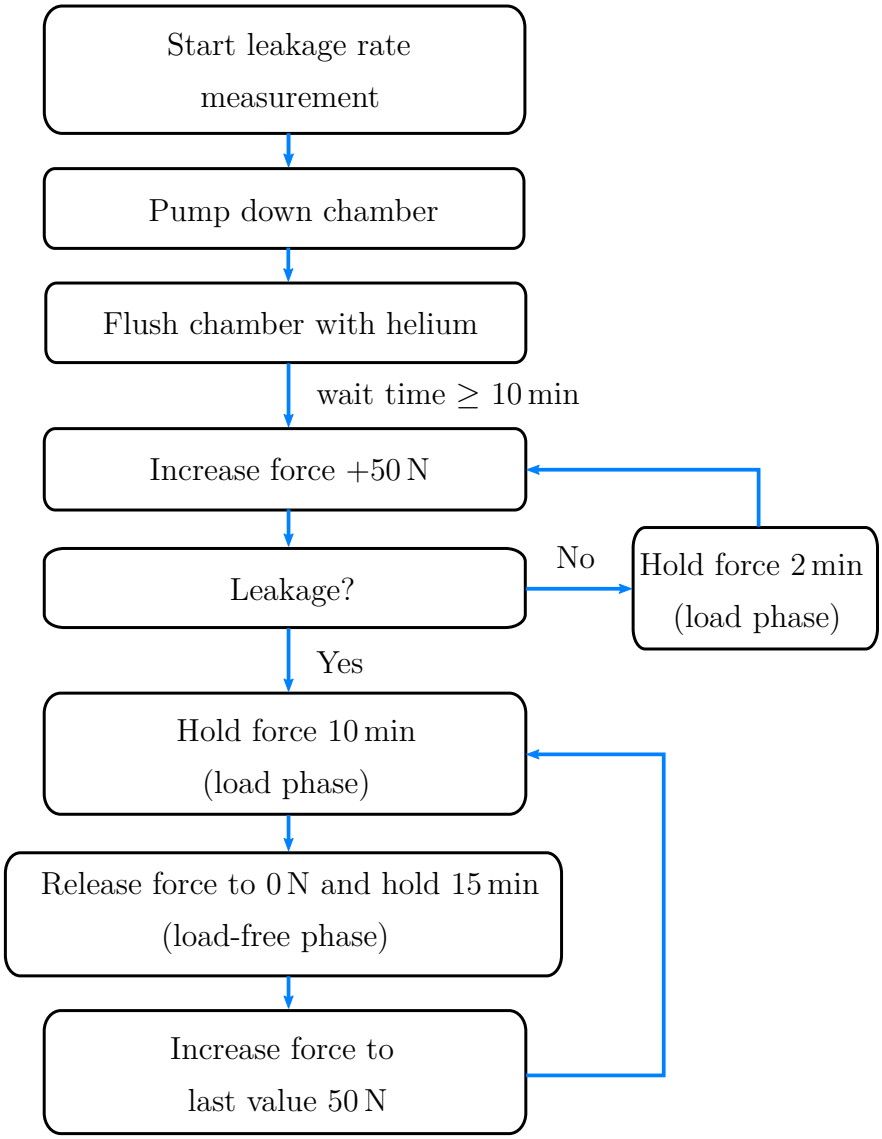

Figure 7.4: This flow chart shows the test procedure for the leakage rate measurements, developed within this thesis. Due to the limit of the measuring range of the force sensor of 2 000 N, the last force step is at 1 950 N [Els21].

At this point, the leakage rate test starts with a released linear motor and a force of 0 N. In the first step, the force is increased in 50 N steps. If the leakage rate stays at the ground value, the force step (load phase) is held for 2 min, before the force is increased by 50 N. 2 min are sufficient, considering the dead time of the leakage detector, which was measured in pre-tests to be only a few seconds. As shown in the flow chart in figure 7.4, this loop continues until the leakage detector indicates the first significant increase of the leakage rate. This marks the first elastic leakage of the tested CF flange connection, as shown in the raw data plot, for stainless steel at a torque of 12.5 N m, in figure 7.5. At this point, the force and the resulting momentum on the CF connection is high enough to form a gap and thereby a leakage. From this point onward, the force (load phase) is held for 10 min. This time was set using the example load phase for the total burn time of all engines of a Falcon 9 launch into a low earth orbit for approximately 440 s [Spa20].

To investigate which force has caused a temporary (elastic) or a permanent (plastic) leakage, the force is released to 0 N and kept for 15 min (load-free phase). If the leakage rate decreases to its initial base value, the force causes an elastic deformation (elastic leakage) and the CF connection is able to seal itself again. In case of a plastic leakage, the leakage rate will settle on a higher value than the base value, as shown in the first plastic leakage in figure 7.5.

For the duration of the load-free time, several points were taken into account. Since the test cannot be paused over night, the overall test should be performed within a maximum of 12 h. However, the load-free phase needs to be long enough to be able to accept settling effects and to ensure a reliable leakage rate, which can also be used on longer timescales. The load-free phase is intended to display the overall microgravity flight of a sounding rocket mission (approximately 300-360 s). The load-free phase was set for 15 min, as a good trade-off for the tests.

Subsequently, the force will be increased to the next higher force step, continuing the procedure sequentially up to the last force step of 1 950 N. This upper limit is set by the measuring range of the force sensor of 2 000 N.

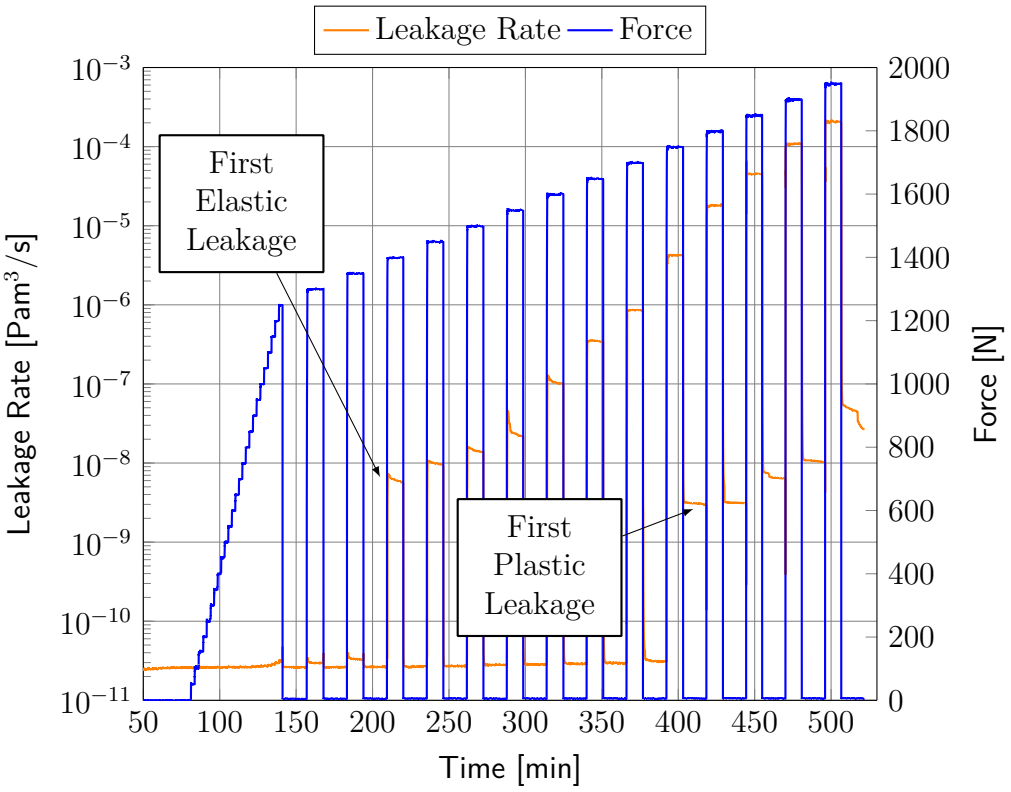

Figure 7.5: The plot shows as an example the raw data for stainless steel at a torque of 12.5 N m (test series 2 of table 7.2). It indicates the leakage rate and the force increased over time with the points where the first elastic and the first plastic leakage occurs. The elastic leakage is detected during the load phase, where the force is held, while the plastic leakage is detected during the load-free phase when the force is released.

7.3 Experimental Results

As a primary outcome of this thesis, the following sections show the results of the four performed test series, including their data post-processing and the test uncertainties. The results are discussed in detail and the findings are summarized in tables 7.3 and 7.4.

7.3.1 Data Post-processing and Test Uncertainties

The upcoming sections discuss the results of all four test series (see section 7.2). The tests are conducted by the same test procedure as presented in the flow chart in figure 7.4, from 0 N, increasing the force in steps of 50 N up to 1 950 N. With the stepwise increase, the points of the first elastic and plastic leakages are experimentally investigated. Additionally, the absolute leakage rate should be identified within the boundaries of the test uncertainties of the test setup. To determine the force and leakage rate values from the raw data, the mean value of the leakage rate for the load and load-free phase is calculated for each load step. In the upcoming sections, the leakage rate is plotted over the associated force values.

As an example, figure 7.6 shows the raw data plot for stainless steel, torqued at 10 N m (test series 2, copper gasket annealed), which identifies settling effects once the load is released. These settling effects can be explained by the elastic behavior, deformation and re-deformation of the CF knife-edge/copper gasket connection, the mounting screws and the tested tubes. The main fraction of the elastic behavior is assumed to be happening in the copper gasket, due to its comparatively soft material. In figure 7.6, two points are marked, where the settle effects are clearly shown over the entire load-free phase. A constant decrease of the leakage rate is shown, although the force is fully released. In the prior force steps, the leakage rate converges against a value, but the settle effects can be still seen during the initial time once the load is released. If the mean value is calculated over the entire load-free phase, these values might not provide a reliable absolute leakage rate value. The reason is the high values (multiple orders of magnitude) during the settlement, compared to the expected mean value. This will result in a high standard deviation of the absolute leakage rate. The standard deviation s for the mean value of the leakage rate and the force was calculated by

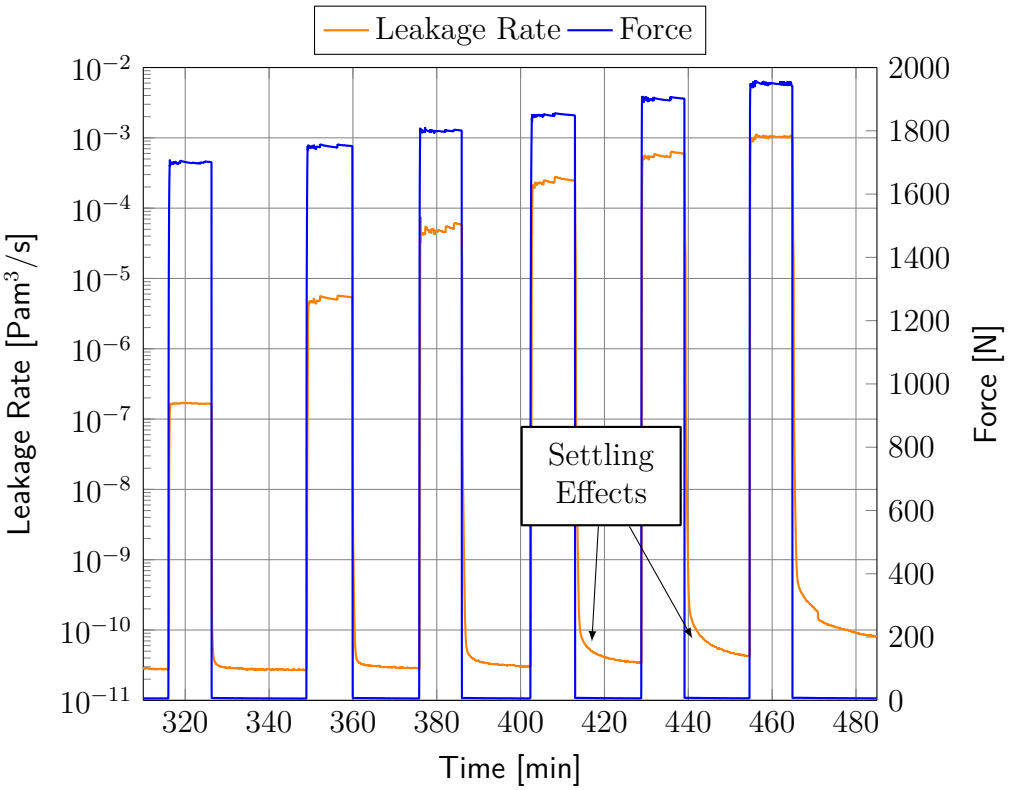

Figure 7.6: The plot shows as an example the raw data for stainless steel at a torque of 10 N m (test series 2 of table 7.2). It indicates the settling effects which occur during the tests.

[Kin19]

$$s = \sqrt{\frac{\sum_{i=1}^{n}(x_i - \bar{x})^2}{n-1}}, \tag{7.1}$$

where x_i is the +value of the i^{th} data point, $\bar{x}$ the mean value of the data set and n the number of data points in the data set. In addition, the uncertainties of the leakage detector in the y-axis, and the force sensor in the x-axis, are added and implemented in the result plots. The 0.5 % uncertainty [MM21] of the full scale value (2 kN) of the force sensor (*Model KM30z-2KN* by *ME-Meßsysteme*), results in an absolute uncertainty of ±10 N. The leakage detector has an uncertainty of 15 % of the measured value.

While the mean value over the entire load-free phase takes the settle effects into account, it is in many cases not reliable and useful for the determination of the absolute leakage rate value. Rather, the majority of the settle effects should be excluded, which can be done by a trimmed mean value. A trimmed mean excludes a certain percentage α of the highest and lowest values. In the presence of significant settling effects, it excludes the values during the leakage rate drop, and results in more accurate absolute values. Literature values for α are between 10 % and 20 %, while 0 % would result in the (arithmetic) mean value [Kre05]. For the data-processing in these test sets, an α of 10 % was chosen. This includes the majority of data, and results in a reliable fit for the data set.

Additionally, the mean value over the last 2 min are calculated and plotted. Within this time, a significant amount of values are taken into account, but settle effects are almost eliminated, or will result in a high standard deviation and uncertainty. These absolute leakage rate values can be used as an extrapolation for a permanent leakage rate exceeding the 15 min measuring time. In the visualization of the test results, the mean value, the trimmed mean value, and the mean value of the last 2 min will be plotted in one figure. These figures will be used to discuss the results in the following sections.

7.3.2 Test Series 1 (316316CU)

This section discusses the results of the test series 1 (TS1) for all three tightening torques 10 N m, 12.5 N m and 15 N m. The two test tubes are both made of stainless steel (316LN-ESR) with a non-annealed copper gasket. Figure 7.7 shows the plots of all torques for the mean (upper plot), trimmed mean (middle plot), and the mean value of the last 2 min (lower plot).

In the 10 N m tightening torque test, the first leakage is shown during the load phase at the 1 150 N force step. The force step with a calculated mean value of 1 149.7 N, results in a leakage rate for the trimmed mean of $2.2 \times 10^{-9}\,\mathrm{Pa\,m^3\,s^{-1}}$. The ground value was at $2.5 \times 10^{-11}\,\mathrm{Pa\,m^3\,s^{-1}}$. In the

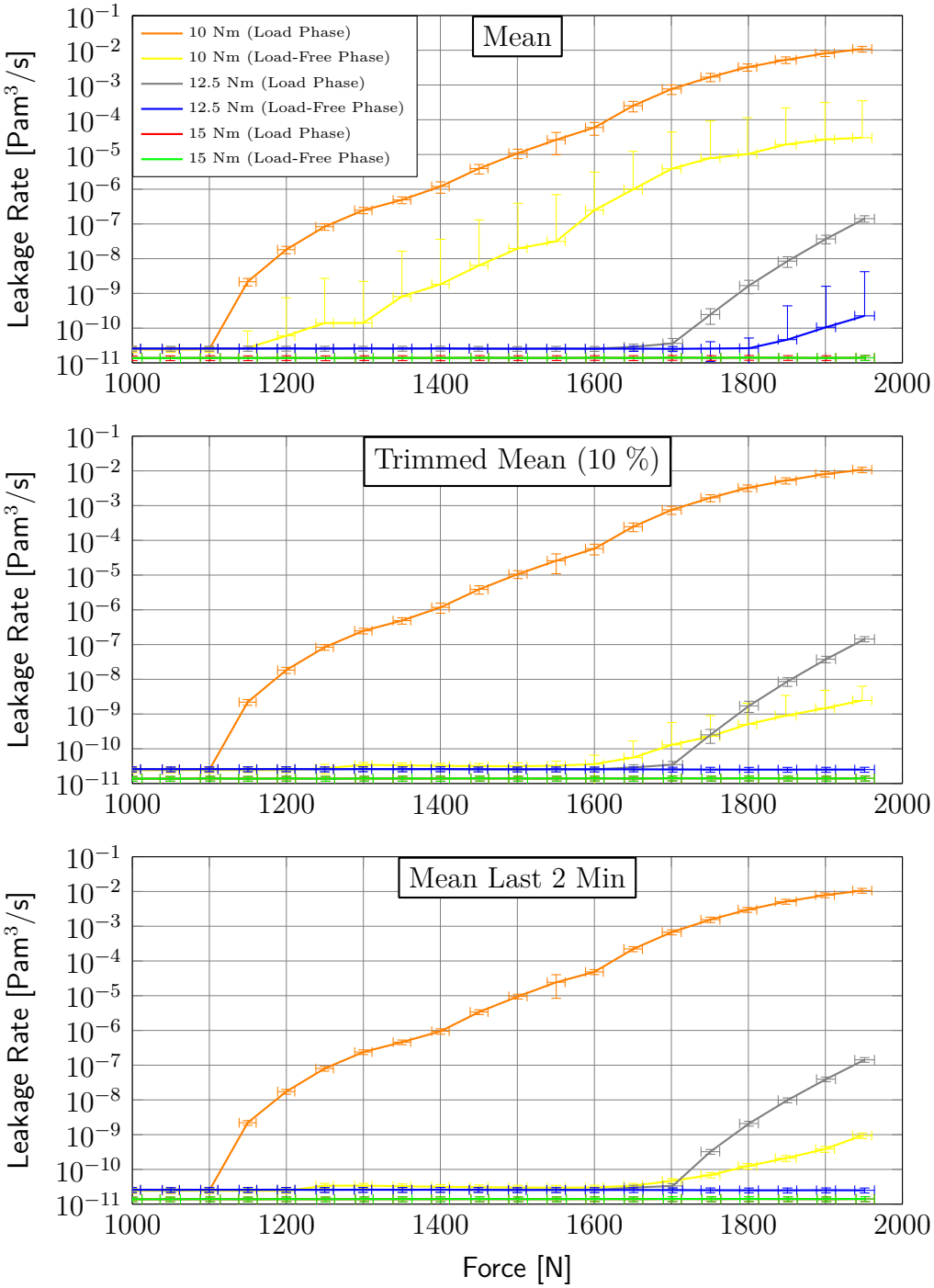

Figure 7.7: The plots of the test series 1 (see table 7.2) with both test tubes made of stainless steel (316LN-ESR) and a non-annealed copper gasket. The load and load-free values are plotted for all three tightening torques 10 N m, 12.5 N m and 15 N m.

following force steps, the leakage rate continuously increases with each force step throughout the load phase, when the force is applied. To identify if the force caused a permanent (plastic) leakage, the force is released after the load phase. Since the upper plot in figure 7.7 includes full settling effects, the high uncertainties make the values not reliable to determine the absolute leakage rate. The trimmed mean values indicate a first plastic leakage in the force range of 1 650 to 1 750 N, with a constant increase of the following force steps. However, the raw data and the plotted uncertainties show that the leakage rate was not converging yet, and a constant decrease occurred (similar to figure 7.6). In this case, the mean values over the last 2 min are the most reliable data to determine the absolute values for a permanent (plastic) leakage. It shows the first increase of the leakage rate at the force range between 1 700 to 1 750 N, and goes up to a leakage rate value of $9.4 \times 10^{-10}\,\mathrm{Pa\,m^3\,s^{-1}}$ for the last force step of 1 950 N (actual mean value 1 947.9 N).

For the tightening torques of 12.5 N m, all three plots indicate the first increase of the leakage rate at 1 700 N and a significant increase of around one order of magnitude at 1 750 N. The mean force of 1 701.8 N, results in a leakage rate of $3.3 \times 10^{-11}\,\mathrm{Pa\,m^3\,s^{-1}}$ and $3.2 \times 10^{-10}\,\mathrm{Pa\,m^3\,s^{-1}}$ for 1 750.6 N. The following force steps continuously increase the leakage rate up to $1.4 \times 10^{-7}\,\mathrm{Pa\,m^3\,s^{-1}}$ for the 1 950 N (1 950.9 N) step. The trimmed mean and the mean of the last 2 min, shows no increase of the leakage rate up to the last force step of 1 950 N. In this case no permanent leakages occur due to the applied force.

The tightening torques of 15 N m indicates no leakages throughout the load and the load-free phase. In comparison to each other, it is shown that the leakage rate for the stainless steel tubes with a non-annealed copper gasket depend on the tightening torque. The lower torque of 10 N m results in an earlier leakage than for 12.5 N m, for the load and load-free phase, while 15 N m indicates no leakage at all.

7.3.3 Test Series 2 (316316CUA)

In test series 2 (TS2), the results for all three tightening torques, with both test tubes made of stainless steel (316LN-ESR) and an annealed copper gasket, are presented. Figure 7.8 shows the load and free load phase for the different determinations of the leakage rate value. The first leakage is indicated for the tightening torque of 10 N m at the load phase with the calculated force of 1 500.0 N. Throughout this load phase, the leakage rate was rapidly dropping over one order of magnitude and then settled at a certain leakage rate value. The raw data indicates that once the force was applied, an initial leakage occurred, but due to elastic material behavior, the gap causing the leak was getting smaller again. This was only the case for the 1 500 N and 1 550.0 N force step. Once the force was high enough, this behavior was not observed anymore. Because of that, the mean values for the last 2 min should be considered for the quantification of the absolute leakage rate value. The leakage rate at the 1 500 N force step is then calculated to $1.0 \times 10^{-9}\,\mathrm{Pa\,m^3\,s^{-1}}$. This absolute value should only be used as a leakage rate on longer time scales. The following force steps continue to increase the leakage rate, except for the force step at 1 700 N. This indicates that the force 1 700 N was not high enough to cause a higher leakage.

The upper plot in figure 7.8 indicates, while considering the uncertainties, that the first permanent (plastic) leakage occurs at the 1 800 N force step. As shown in the raw data plot in figure 7.6, the values are affected by the settling effects. For the 15 min measuring time, the values are not converged yet and a longer measuring time would have been needed. Irregardless, the test procedure was followed for all tests to ensure repeatable and consistent tests within the overall time constraints for the tests (see section 7.3.1). For the absolute value of the leakage rate, the mean of the last 2 min should be used. These values indicate a slow increase of the leakage rate from the 1 850 N (1 850.1 N) force step onward, with a slightly increased leakage rate of $3.5 \times 10^{-11}\,\mathrm{Pa\,m^3\,s^{-1}}$ compared to the ground value of $2.9 \times 10^{-11}\,\mathrm{Pa\,m^3\,s^{-1}}$.

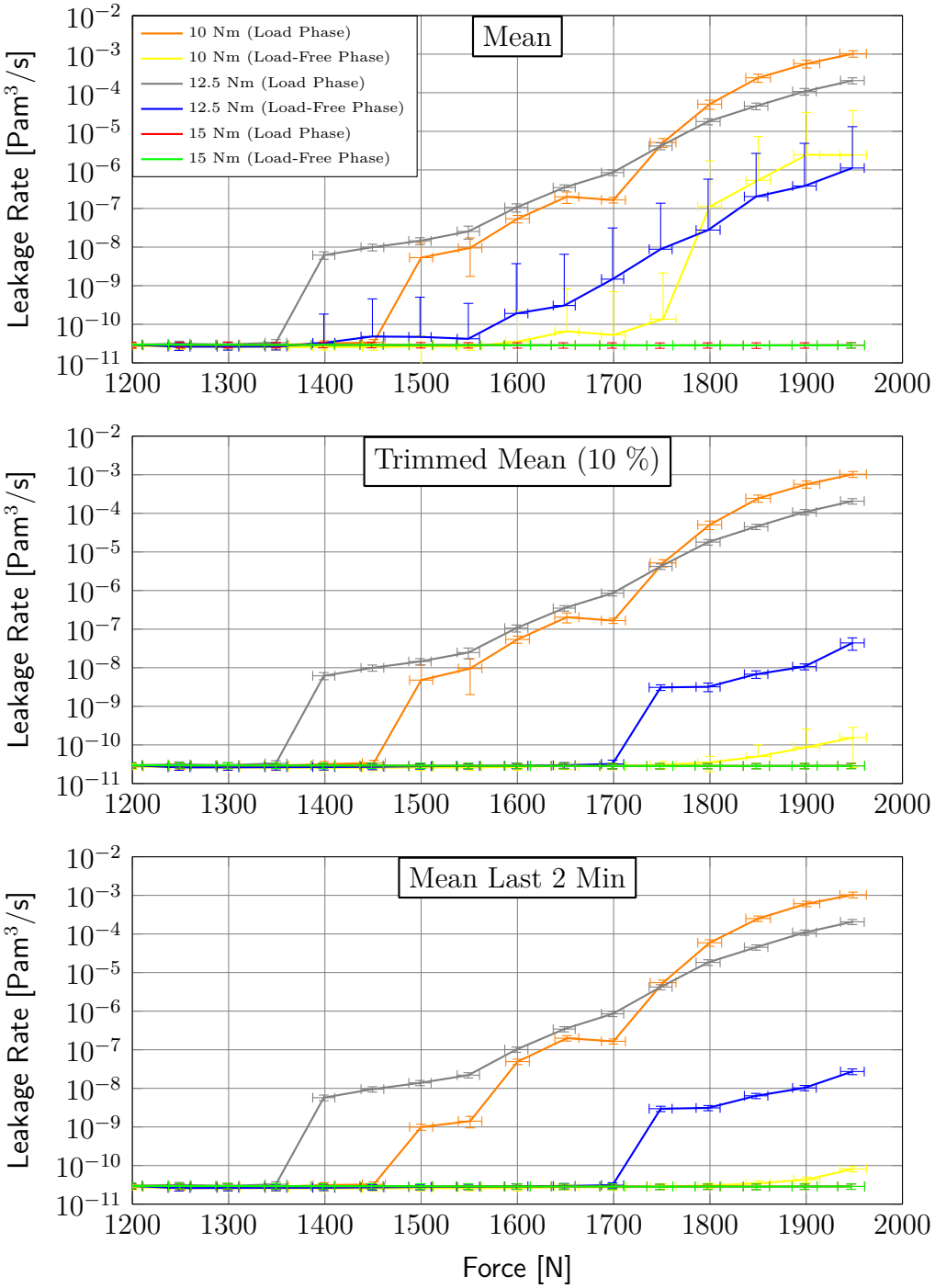

Figure 7.8: The plots of the test series 2 (see table 7.2) with both test tubes made of stainless steel (316LN-ESR) and an annealed copper gasket. The load and load-free values are plotted for all three tightening torques 10 N m, 12.5 N m and 15 N m. (upper plot adapted from [Els21])

The last force step of the calculated force value of 1 948.8 N has a leakage rate of $8.2 \times 10^{-11}\,\mathrm{Pa\,m^3\,s^{-1}}$.

Within the test of the tightening torque of 12.5 N m, the first significant leakage is indicated at the 1 400 N (1 398.8 N) force step. The force results in a leakage rate of $6.2 \times 10^{-9}\,\mathrm{Pa\,m^3\,s^{-1}}$ for the trimmed mean value. The following force steps increase the leakage rate consistently up to a leakage rate of $2.1 \times 10^{-4}\,\mathrm{Pa\,m^3\,s^{-1}}$ for the last force step of 1 950 N (1 948.0 N). The plot of the load-free phase indicates a significant leakage rate increase at the force step of 1 750 N (1 748.8 N), which results in a permanent leakage rate of $3.1 \times 10^{-9}\,\mathrm{Pa\,m^3\,s^{-1}}$ for the trimmed mean value. The mean value for the last 2 min, is at $3.0 \times 10^{-9}\,\mathrm{Pa\,m^3\,s^{-1}}$ in the same range.

The tightening torque of 15 N m indicates no leakages throughout the load and the load-free phase, as shown in all plots in figure 7.8. Test series 2 shows that a tightening torque of 12.5 N m indicates the first leakages, for the load and load-free phase, at a lower force step than for 10 N m. However, higher force steps above 1 750 N, result for 10 N m compared to 12.5 N m, in a higher leakage rate during the load phase. This shows that the applied force needs to be taken into account when deciding on the tightening torques. Since the load-free phase shows higher leakage rates even at lower force steps, a tightening torque of 12.5 N m is not advisable for stainless steel (316LN-ESR) CF tubes with an annealed copper gasket.

7.3.4 Test Series 3 (AluAluCUA)

In test series 3 (TS3), two test tubes made of aluminum (*AluVaC®*) are investigated. An annealed copper gasket is used and the tests are performed for all three tightening torques 10 N m, 12.5 N m and 15 N m. The load and load-free phase of the tests are presented in figure 7.9 for the different determinations of the leakage rate value.

The tightening torque of 10 N m shows the first leakage for a force of 1 050 N (1 049.7 N) within the load phase. At this point, the first increase of the leakage rate to a value of $6.3 \times 10^{-10}\,\mathrm{Pa\,m^3\,s^{-1}}$ is shown, for the mean value of the last 2 min. The leakage rate increases with the following force steps up to 1 350 N, but afterwards the leakage rate is rather constant or evenly decreasing. The leakage rate increases again once the force is greater than 1 800 N.

The first plastic leakage is shown during the load-free phase for the force step of 1 350 N with a calculated value of 1 333.9 N. The leakage rate in the following steps decreases where the force is less than 1 500 N. The leakage rate for forces greater than 1 500 N, increases consistently up to the last value of 1 950 N. This behavior indicates, that after the initial increase of the leakage rate, the following force steps were not high enough to cause further permanent leakages. This could be explained by the lower strength of aluminum, compared to stainless steel (see table 2.2).

In the tightening torque of 12.5 N m, the first leakage throughout the load phase is observed at the force step of 1 700 N (1 698.5 N). The applied force results in a significant increase of the leakage rate to a value of $9.7 \times 10^{-6}\,\mathrm{Pa\,m^3\,s^{-1}}$ for the mean and the trimmed mean value over the entire measuring time. The mean value calculated over the last 2 min settles the leakage rate in the same range with a value of $9.1 \times 10^{-6}\,\mathrm{Pa\,m^3\,s^{-1}}$. In the following force steps, the leakage rate increases with a maximum force step of 1 900 N. The last step of 1 950 N results in a lower leakage rate, but in the same order of magnitude.

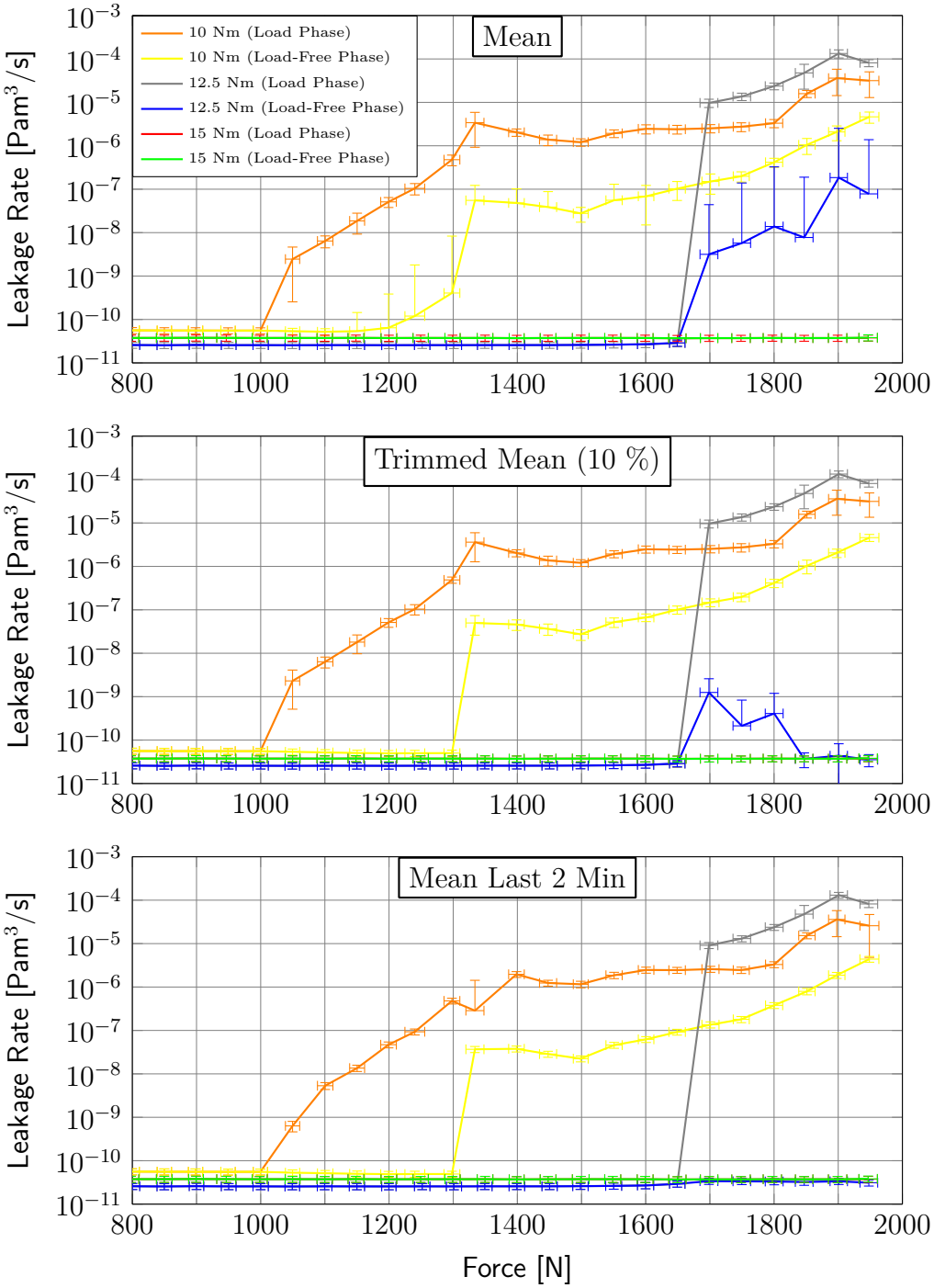

Figure 7.9: The plots of the test series 3 (see table 7.2) with both test tubes made of aluminum (*AluVaC*®) and an annealed copper gasket. The load and load-free values are plotted for all three tightening torques 10 N m, 12.5 N m and 15 N m. (upper plot adapted from [Els21])

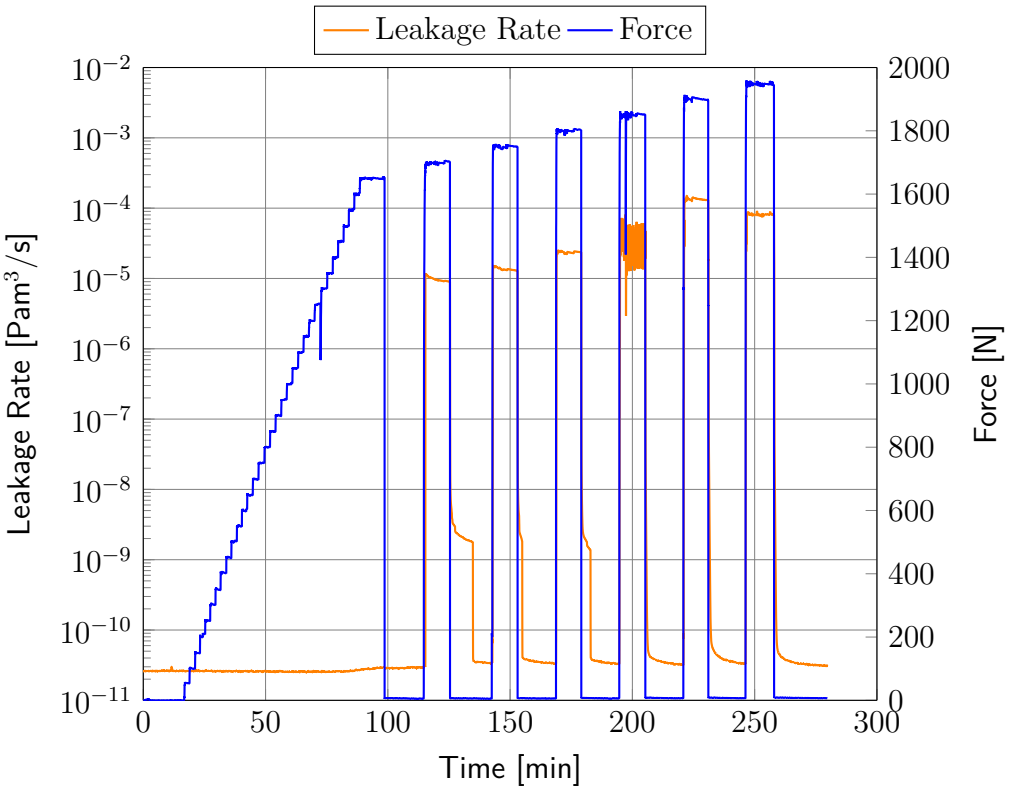

Figure 7.10: The plot shows the raw data for aluminum at a torque of 12.5 N m (test series 3 of table 7.2). It shows the leakage rate and the force over time.

The load-free plot for 12.5 N m indicates the first permanent leakage at the same force step of 1 700 N. The raw data plot in figure 7.10 shows that after the force is released, the leakage rate can be initially observed in the range from 2×10^{-9} Pa m^3 s^{-1} to 4×10^{-9} Pa m^3 s^{-1}. However, after around 8 min, the leakage rate drops suddenly to a value of 3.4×10^{-11} Pa m^3 s^{-1}. Throughout the remaining load-free phase, the leakage rate stays at this value, which is in the same order of magnitude as the ground value of 2.6×10^{-11} Pa m^3 s^{-1}. The next two force steps exhibit similar behavior with a sudden drop after a certain amount of time. The last three force steps show no such behavior, but also indicate settling effects as already seen throughout other tests. The sudden drop can be explained by the elastic behavior of the test specimen. Although it is assumed that the highest fraction of this behavior is caused by the softer copper gasket, the tightening screws of the CF connection will also

have an impact. The initial gap caused by the previously applied force results in a permanent leakage, but the gap and the leakage was sealed again. In the determination of the absolute value, only the mean value over the last 2 min can be used as an extrapolation on longer time scales. In the load phase at the 1 850 N force step, the leakage rate changes over a wide range. This is caused by the leakage detector, which changes its operation mode from fine to gross leakage mode (see section 2.2.6).

The tightening torque of 15 N m showed no leakage in the load or the load-free phase, which is similar to the test series above. In comparison to each other, the tightening torque of 10 N m shows an earlier elastic or plastic leakage, than for 12.5 N m. The load phase for the 12.5 N m plot shows that once the leakage occurred, the leakage rate itself was above the leakage rate for the 10 N m tightening torques. The plots of the load-free phase indicate an earlier increase of the leakage rate for 10 N m than for 12.5 N m. The test of the aluminum tubes show a dependency on the leakage rate, where the first leakages (elastic or plastic) occur earlier for lower tightening torques.

7.3.5 Test Series 4 (316AluCUA)

In test series 4 (TS4), the tests were conducted with one test tube made of stainless steel (316LN-ESR) and one made of aluminum (*AluVaC®*), with an annealed copper gasket. In the tightening torque of 10 N m, no increase of the leakage rate was observed throughout the load and load-free phase. The ground value of the leakage rate during this test was in the range of $3.2 \times 10^{-11}\,\mathrm{Pa\,m^3\,s^{-1}}$.

The 12.5 N m tightening torque indicates a first leakage throughout the load phase for the force step of 1 600 N (1 600.1 N). However, the leakage rate is only increasing to a value of $3.2 \times 10^{-11}\,\mathrm{Pa\,m^3\,s^{-1}}$, which is in the same range as the ground value for the tightening torque of 10 N m. The following force steps are not causing a significant increase of the leakage rate, with the highest value of $3.7 \times 10^{-11}\,\mathrm{Pa\,m^3\,s^{-1}}$ for the last force step. The same behavior is seen for the load-free phase plot, where the first increase is shown at the 1 600 N force step and a slow increase occurs for the following values. The highest leakage rate was observed at the last force step at a value of $3.2 \times 10^{-11}\,\mathrm{Pa\,m^3\,s^{-1}}$. Considering the uncertainties for the leakage rate, there are no significant leakages occurring for the load and load-free phase for the 12.5 N m tightening torque.

Throughout the load phase of the tests, with a tightening torque of 15 N m, the force step of 1 750 N (1 752.4 N) results in the first significant leakage. The raw data plot in figure 7.12 shows that after the initial leakage, the leakage rate decreases rapidly. This indicates that the applied force is not high enough to obtain the leakage, which results in a high standard deviation and uncertainty for the determination of the absolute leakage rate value. The mean value over the last 2 min shows the most reliable leakage rate value ($1.3 \times 10^{-9}\,\mathrm{Pa\,m^3\,s^{-1}}$) considering the uncertainties. The plots in figure 7.11 show that, within the next force steps, the leakage rate is again in the range of the ground value ($3.3 \times 10^{-11}\,\mathrm{Pa\,m^3\,s^{-1}}$). The leakage rate is at a constant level and no further leakages occur up to the last force step. During the

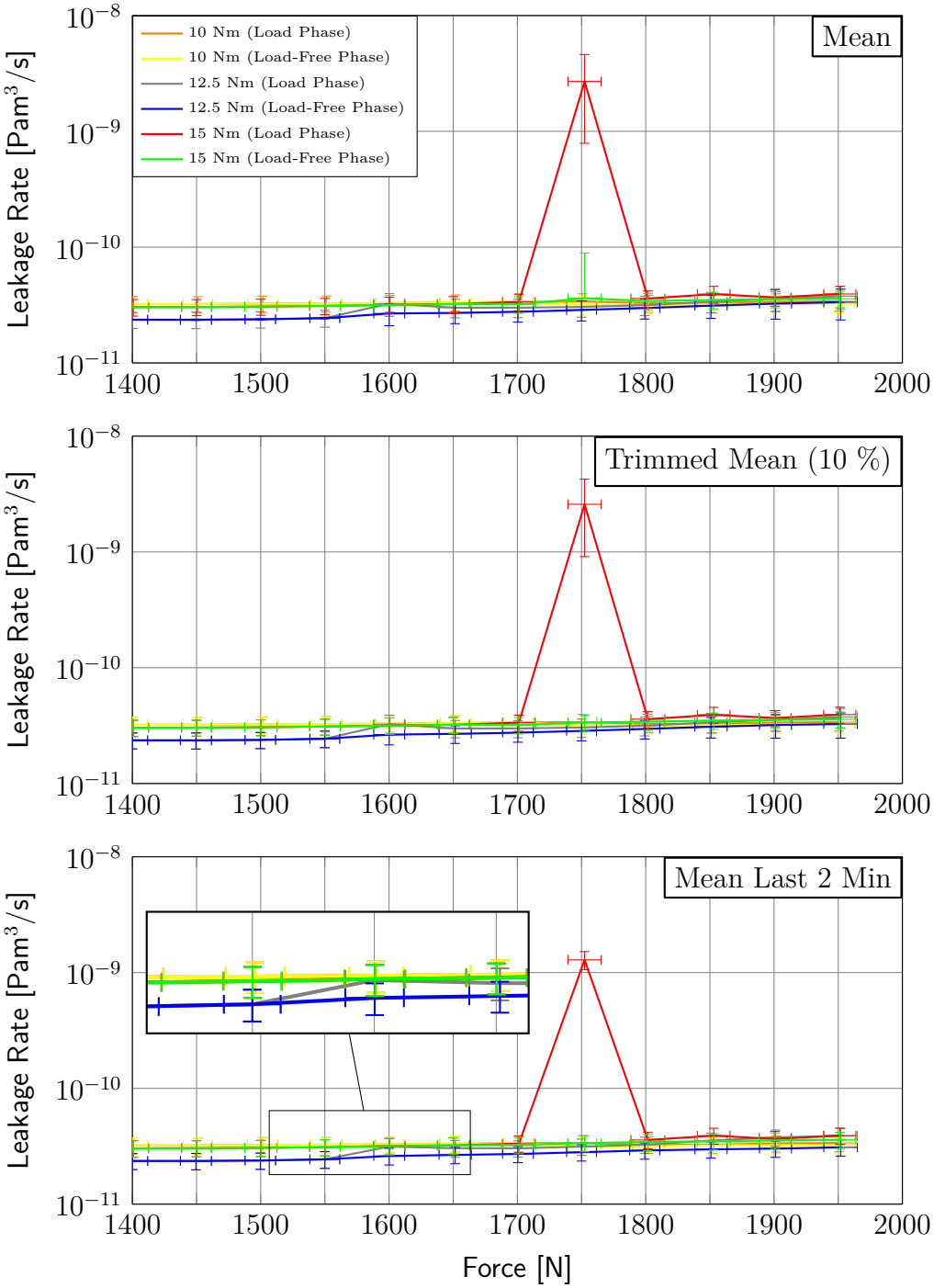

Figure 7.11: The plots of the test series 4 (see table 7.2) with one test tube made of stainless steel (316LN-ESR) and one of aluminum (*AluVaC*®), and an annealed copper gasket. The load and load-free values are plotted for all three tightening torques 10 N m, 12.5 N m and 15 N m.

load-free phase there is no increase of the leakage rate observed, which shows that no permanent (plastic) leakages occurred. In summary, it can be stated

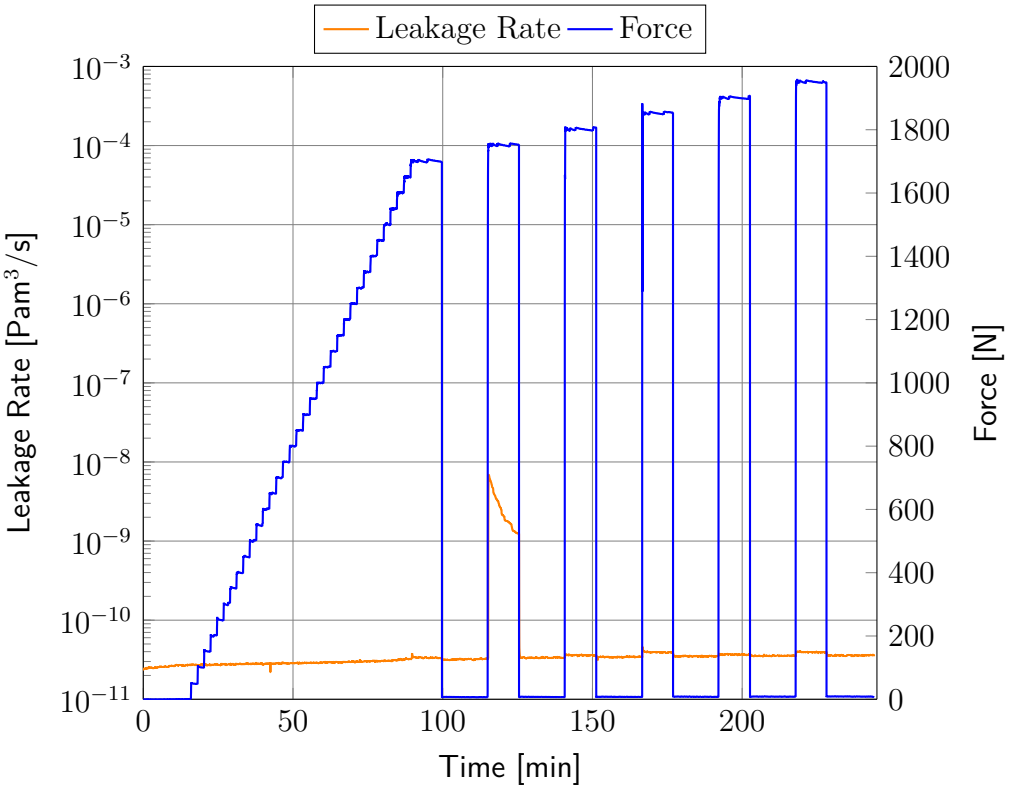

Figure 7.12: The plot shows the raw data for aluminum and stainless steel at a torque of 15 N m (test series 4 of table 7.2). It shows the leakage rate and the force over time.

that for the test with one test tube in aluminum and one in stainless steel, no significant leakages for the 10 N m tightening torque occurred, and only minor increased leakage rates occurred for 12.5 N m. In this context, it is worth mentioning that the ground value for 10 N m was in the same region as the determinant values of the indicated leakages for the 12.5 N m tightening torque. The only significant increase was observed at a tightening torque of 15 N m. For the following force steps, the leakage rate was at the ground value again.

7.4 Comparison of Results

This section compares the results of the four test series (see table 7.2). Table 7.3 summarizes the data points where the first elastic leakage occurs and table 7.4 summarizes the data for the first plastic leakage, indicating a permanent leakage. While the different tests are explained in detail in each of the dedicated sections, these tables show an overview of the findings throughout this thesis of all the test series. The dependency of the tightening torque on the leakage rate within each test series can also be found within the different test sections. In the tables, the determination method is marked, as well as the total test uncertainties as discussed in section 7.3.1.

For the tightening torque of 15 N m there was no elastic or plastic leakage detected for TS1, TS2 or TS3. While the tests indicate that this tightening torque is advisable for CF DN40 flanges, this torque is 1.5 times higher than the standard tightening torque (10.4 N m) for the used stainless steel A2-70 screws. A higher torque could lead to material failure on longer time scales, which could result in damage and leakages within the UHV system. However, on the measured time scales, the data showed no direct disadvantage for the leakage rate of the CF flange connection.

In the load phase of TS1, the lower tightening torque of 10 N m showed the first increase in the leakage rate at a lower force step (1 150 N), compared to 1 500 N within TS2. The same is observed for the load-free phase, which also indicates that the first plastic leakage occurs at a lower force step (1 700 N) for TS1. The data indicates an advantage in using an annealed copper gasket for the tightening torque of 10 N m for stainless steel (316LN-ESR) CF DN40 tubes.

In contrast, the tightening torque of 12.5 N m shows that TS1 has a higher first elastic and plastic leakage compared to TS2. The higher tightening torque, together with the non-annealed copper gasket, leads to a higher force before leakages occur. In the load-free phase of TS1 no leakage was observed,

while for TS2 plastic leakages occurred from a force step of 1 750 N onward. For the decision of the type of copper gasket used for stainless steel CF tubes, the data indicates that the tightening torque needs to be taken into account.

In the comparison between stainless steel (TS1 and TS2) and aluminum (TS3), the tightening torque of 10 N m shows, for both the load and load-free phase, a leakage at a lower force step for aluminum. For the tightening torque of 12.5 N m, TS3 shows a first elastic leakage at the same force step of 1 700 N as for TS1. However, the leakage rate values for TS3 show, compared to TS1, a significant increase of the leakage rate of around five orders of magnitude. The load-free phase of TS3 indicates similar values as for the TS2, while TS1 shows no leakages at all. This data shows, that for aluminum CF tubes, a tightening torque of 12.5 N m is advisable. Compared to stainless steel, the data for aluminum, for a tightening torque of 12.5 N m, shows similar behavior. For this torque, the data shows no disadvantage in using aluminum CF tubes instead of stainless steel.

Deviating from the other tests, TS4 shows no elastic or plastic leakage for a tightening torque of 10 N m. The data for the tightening torque of 12.5 N m indicates an elastic and plastic leakage from 1 600 N onward. However, the leakage rate values are in the same range as the lowest measurable limits of the leakage detector, and no significant leakage occurs for all force steps. Throughout TS4, one leakage was seen for the tightening torque of 15 N m at the force step of 1 750 N while the load was applied, although further force steps showed no leakages. The load-free phase of TS4 indicated no permanent leakage for 15 N m, similar to the other test series. This indicates that the use of different materials, stainless steel (316LN-ESR) and aluminum ($AluVaC^{®}$), shows a positive effect on the leakage rate. The tightening torque of 10 N m is most advisable for a mixture of these materials, up to applied force of 1 950 N.

Table 7.3: This table summarizes the data of the experimental leakage rate tests (see table 7.2). It shows the values for the first elastic leakage for the different tightening torques (10 N m, 12.5 N m, 15 N m). The leakage rate is presented for all determination methods, the mean value (M), the trimmed mean value (T), and the mean value for the last 2 min (L). It includes total uncertainties for the force and leakage rate value.

Test Series	Tightening Torque in N m	Force Step in N	Calculated Force in N	Total Unc. in N	Det. Method	Leakage Rate in $Pa\,m^3\,s^{-1}$	Total Unc. in $Pa\,m^3\,s^{-1}$
TS 1 316316CU	10	1150	1149.7	11.0	M	2.2×10^{-9}	5.3×10^{-10}
					T	2.2×10^{-9}	4.2×10^{-10}
					L	2.2×10^{-9}	3.4×10^{-10}
	12.5	1700	1701.8	12.8	M	3.6×10^{-11}	1.4×10^{-11}
					T	3.5×10^{-11}	8.3×10^{-12}
					L	3.3×10^{-11}	5.4×10^{-12}
	15	>1950	>1951.7	12.0	M		
					T	no leakage detected	
					L		
TS 2 316316CUA	10	1500	1500.0	12.0	M	5.3×10^{-9}	7.7×10^{-9}
					T	4.8×10^{-9}	7.0×10^{-9}
					L	1.0×10^{-9}	1.8×10^{-10}
	12.5	1400	1398.8	11.4	M	6.2×10^{-9}	1.4×10^{-9}
					T	6.2×10^{-9}	1.3×10^{-9}
					L	5.7×10^{-9}	1.0×10^{-9}
	15	>1950	>1946.8	13.9	M		
					T	no leakage detected	
					L		
TS 3 AluAluCUA	10	1050	1049.7	11.1	M	2.5×10^{-9}	2.2×10^{-9}
					T	2.3×10^{-9}	1.8×10^{-9}
					L	6.3×10^{-10}	1.7×10^{-10}
	12.5	1700	1698.5	13.9	M	9.7×10^{-6}	2.1×10^{-6}
					T	9.7×10^{-6}	2.0×10^{-6}
					L	9.1×10^{-6}	1.5×10^{-6}
	15	>1950	>1946.7	14.4	M		
					T	no leakage detected	
					L		
TS 4 316AluCUA	10	>1950	>1950.6	12.4	M		
					T	no leakage detected	
					L		
	12.5	1600	1600.1	12.0	M	3.3×10^{-11}	7.2×10^{-12}
					T	3.7×10^{-11}	6.4×10^{-12}
					L	3.1×10^{-11}	5.4×10^{-12}
	15	1750	1752.4	12.9	M	2.7×10^{-9}	1.9×10^{-9}
					T	2.6×10^{-9}	1.7×10^{-9}
					L	1.3×10^{-9}	2.3×10^{-10}

Table 7.4: This table summarizes the data of the experimental leakage rate tests (see table 7.2). It shows the values for the first plastic (permanent) leakage for the different tightening torques (10 N m, 12.5 N m, 15 N m). The leakage rate is presented for all determination methods, the mean value (M), the trimmed mean value (T), and the mean value for the last 2 min (L). It includes total uncertainties for the force and leakage rate value.

Test Series	Tightening Torque in N m	Force Step in N	Calculated Force in N	Total Unc. in N	Det. Method	Leakage Rate in $Pa\,m^3\,s^{-1}$	Total Unc. in $Pa\,m^3\,s^{-1}$
TS 1 316316CU	10	1700	1700.5	12.3	M	3.9×10^{-6}	4.1×10^{-5}
					T	1.3×10^{-10}	4.4×10^{-10}
					L	4.7×10^{-11}	8.0×10^{-12}
	12.5	>1950	>1951.0	12.8	M	no leakage detected	
					T		
					L		
	15	>1950	>1951.7	12.0	M	no leakage detected	
					T		
					L		
TS 2 316316CUA	10	1850	1850.0	12.8	M	5.4×10^{-7}	6.8×10^{-6}
					T	5.0×10^{-11}	5.0×10^{-11}
					L	3.5×10^{-11}	5.6×10^{-12}
	12.5	1750	1748.8	11.9	M	8.8×10^{-9}	1.3×10^{-7}
					T	3.1×10^{-9}	5.2×10^{-10}
					L	3.0×10^{-9}	4.7×10^{-10}
	15	>1950	>1946.8	13.9	M	no leakage detected	
					T		
					L		
TS 3 AluAluCUA	10	1350	1333.9	14.1	M	5.5×10^{-8}	6.7×10^{-8}
					T	5.0×10^{-8}	2.4×10^{-8}
					L	3.7×10^{-8}	5.9×10^{-9}
	12.5	1700	1698.5	13.9	M	3.2×10^{-9}	4.1×10^{-8}
					T	1.3×10^{-9}	1.3×10^{-9}
					L	3.4×10^{-11}	5.5×10^{-12}
	15	>1950	>1946.7	14.4	M	no leakage detected	
					T		
					L		
TS 4 316AluCUA	10	>1950	>1950.6	12.4	M	no leakage detected	
					T		
					L		
	12.5	1600	1600.1	12.0	M	2.7×10^{-11}	5.8×10^{-12}
					T	2.6×10^{-11}	4.9×10^{-12}
					L	2.6×10^{-11}	4.3×10^{-12}
	15	>1950	1951.2	12.5	M	no leakage detected	
					T		
					L		

8 Conclusion

8.1 Summary

MAIUS-B aims to operate the first dual-species ultracold atom interferometer on a sounding rocket throughout the two upcoming missions MAIUS-2 and MAIUS-3. As one of the primary outcomes of this thesis, the UHV system of the scientific payload MAIUS-B was newly designed, assembled and qualified (see chapter 6). A detailed overview of the scientific payload of MAIUS-B is given in chapter 5. The new thermal and mechanical design is introduced, which was designed and implemented within the scope of this thesis. This includes the new TCS and GSE concept, the mass and size budget, the suspension, and the umbilical and sealing concept. In addition, this thesis provides the science community with the first data set of the investigations on CF flange connections under mechanical loads. These results, as presented in section 7.3, can be used to improve the design and assembly process of UHV systems for a wide range of future space missions, such as cold atom experiments.

In October 2018, the overall payload design of the scientific payload MAIUS-B, flying on both missions MAIUS-2 and MAIUS-3, passed its CDR. Following this, the five subsystems; electronics (EL), physics package (PP), laser system (LS), laser electronics (LE), and batteries (BA), were assembled in a flight configuration, tested, and qualified towards the first launch mission MAIUS-2, planned for 2023. The scientific payload is integrated into seven hull segments in a RADAX design, with an outer diameter of 500 mm. The overall scientific

payload design, including a general mission and payload overview, and a brief introduction of all five subsystems, is given throughout chapter 5.

Compared to the 2017 successfully launched sounding rocket mission MAIUS-1, which contained the scientific payload MAIUS-A, the MAIUS-B payload design was adapted and redesigned from a single-species to a dual-species ultracold atom experiment for the missions MAIUS-2/3. MAIUS-A had a final mass of 309.2 kg and a length of 2 790 mm. First design iterations for MAIUS-B, performed within this thesis, showed an additional mass and length of approximately 90 kg and 930 mm, respectively. Since the same two-stage VSB-30 sounding rocket is used, the MAIUS-B payload was optimized for mass and size, also within the scope of this thesis, to fit into the limits of 340 kg and 3 m. These limits are given by the parachute system of the rocket, and the maximum stress of the manacle-ring, connecting the payload and the rocket motors. In addition, a higher payload mass results in a lower apogee during the parabolic flight and thereby in a shorter microgravity and experimental time. As a first approximation, in an investigation performed by MORABA, with the used motors and nose cone type, a reduction of around 0.55 s per kg is indicated.

The mass and size optimizations conducted throughout this thesis started with a reduction of the thickness of the hull segments from 5 mm to 4 mm, resulting in a mass reduction of around 10 kg. In cooperation with the subsystem responsible, the design of the subsystems was continuously mass and size optimized. One of the main size optimizations was done by the new design of the PS, as part of the PP, which results in a 233.5 mm lower height. As an outcome of this thesis (see section 5.7.1), a mass of 335.3 kg and a length of 2.8 m was derived, which ensures a safe flight, parachute landing, and minimizes the losses in experimental time. This mass results in a microgravity time of approximately 330 s throughout the MAIUS-2/3 missions.

The suspension of the payload within the hull segments was adapted compared to MAIUS-A as part of this thesis, to house the more dense and compact payload of the new overall design layout. All components of the subsystems

are mounted on an instrument platform, mounted by five M5 x 12 mm stainless steel (class 10.9) screws to the hull via brackets. These brackets consists of two vibration dampers and one safety pin, as a safety measure to avoid damaging movement by mechanical loads during the flight. Building up on the heritage of MAIUS-A, the suspension concept (including the vibration dampers, safety pins and the brackets itself) was adapted throughout this thesis, as shown in chapter 5.7.2. Each subsystem is equipped with a total of six brackets beside the PP (as shown in section 5.4), which required a second mounting level and a total of twelve brackets, to account for the high mass of 73.8 kg and a length of 754.5 mm. To ensure a safe operation, a load assessment for the bracket safety factor and for the safety against the connection slippage (bracket to hull segment) was performed in this thesis. For the loads, an acceleration of $127.5\,\mathrm{m\,s^{-2}}$ ($13.0\,\mathrm{g_0}$) for the rocket ascent, $245.3\,\mathrm{m\,s^{-2}}$ ($25.0\,\mathrm{g_0}$) throughout the re-entry phase, and shocks between $490.6\,\mathrm{m\,s^{-2}}$ ($50.0\,\mathrm{g_0}$) and $981.0\,\mathrm{m\,s^{-2}}$ ($100.0\,\mathrm{g_0}$) during the landing and the motor ignition were considered. Considering the PP as the heaviest subsystem, and assuming a worst case scenario with only one mounting level and six brackets, the load assessment showed a minimum safety factor of 1.4. The safety factor against slipping, between the bracket and the hull segment, with a total of five screws per bracket, results in a minimum factor of 5.6 for the PP. This shows that the suspension designed throughout this thesis is capable of carrying the MAIUS-B payload up to $981.0\,\mathrm{m\,s^{-2}}$ ($100.0\,\mathrm{g_0}$) with a reasonable safety margin.

Another outcome of this thesis, was the newly developed and implemented TCS (see section 5.3). Its new design compensates for a high amount of electronic components in a very compact and dense design on the one side, and temperature sensitive components on the other side. The estimated internal heat load produces an overall load of 707.6 W. In addition, a hull temperature up to 120 °C (393.15 K), caused by aerodynamic drag during ascent of the rocket, was taken into account. The new TCS design is divided into two liquid cooling cycles, one for the three electronic subsystems (BA, LE, EL) and one for the PP and LS. Each cooling cycle is connected via umbilicals to the GSE, where two chillers provide the liquid cooling until lift-off. The

chillers are placed on the launch tower and therefore built into an aluminum case, additionally covered by pyroblankets, to withstand the exhaust gas of the launching rocket. While the active liquid cooling is automatically unlocked during lift-off, the MAIUS-B TCS is designed to account for the temperature rise during the flight, while keeping all temperature sensitive components within their required temperature range. Beside this flight mode, the TCS concept was also designed to take the laboratory operation into account. This required the active cooling to compensate for high internal heat loads during the ground operation, testing, and optimization of the experiment prior to launch.

Within the scope of this thesis and as a contribution to the MAIUS-B payload, the TCS concept was developed to include the instrument platform of the subsystems as the heatsink. As explained in detail in section 5.3, this newly developed design concept takes on the one side the heat loads of the different subsystems into account, and realizes on the other side a compact and mass optimized design of the instrument platforms. For the EL, LE and LS, two plates with a milled groove are mounted together, with a stainless steel meander inside. The BA is only equipped with one plate to reduce mass, since it has a comparatively low heat load of 28.8 W. The PP is equipped with a heatsink and several high power amplifiers at the back wall of the pump stack. The TCS, as designed and implemented within this thesis, is a key technology development for the successful transition from a single-species experiment as in MAIUS-A, to a dual-species experiment in MAIUS-B. With its size and mass optimized design, this concept can be used for a multitude of future space missions, but is also easily applicable for ground based experiments.

To prevent freezing down to -40 °C (233.15 K), a glycol/water mixture with 52 % glycol is used as the cooling liquid throughout the cooling cycles. A flow rate test (explained in section 5.3), was performed within this thesis and showed for the 52 % glycol mixture, a flow rate of 5.2 $\mathrm{L\,min^{-1}}$. This was taken into account for the overall TCS concept.

The laser modules require a controlled pressure environment between 800 hPa and 1 100 hPa. Therefore, the payload is sealed and pressurized with artificial air (80 % nitrogen and 20 % oxygen) to around 1 000 hPa. The sealing is done by two sealing plates, on both sides of the payload, with a rubber o-ring. The umbilicals and feedthroughs for cooling, data and power connection from the GSE to the payload, were redesigned and implemented within this thesis, as shown in section 5.7.3. The MAIUS-A payload used DSUB connectors, which showed leakages at the sealing plate, especially for the high power feedthroughs. Compared to MAIUS-A, military grade connectors are used in MAIUS-B for the power and data connections. A pressure test with the hull assembly and the sealing plates was performed as part of thesis, which showed a pressure loss of 40 hPa over 90 h. During a pre-test, only the upper and lower hull segment, including the sealing plates and feedthroughs, were tested. A pressure degradation of 6 hPa over 48 h, compared to 55 hPa over 40 h within MAIUS-A, indicates the improvement of the new sealing concept.

A new UHV system for the MAIUS-B PP, including the new pumps, the new mounting concepts of the EC, the new DPS, and the new ovens, were designed and successfully implemented as one of the contributions of this thesis. The vacuum system as shown in chapter 6, is capable of maintaining a pressure of 2×10^{-11} hPa, which is one order of magnitude better than the required pressure of 5×10^{-10} hPa. The pumping concept is realized with two TSPs and one IGP. The first TSP and the IGP are within the PS and placed on top of the PP to avoid interference with the experiment. In contrast to MAIUS-A, the IGP is mounted horizontally to the instrument platform, which results in a lower height. To place the TSP, it is designed in a 90° angle. The second TSP is mounted close to the experiment to account for the high outgassing rate of the atom chip and its Teflon cables.

The mounting of the EC was adapted throughout this thesis to provide a better accessibility for the assembly and the laboratory operation. The DPS between the 2D and 3D-MOT chamber, was newly designed and now provides a better alignment. A new oven design was implement within this thesis to

accommodate both atom species, ^{87}Rb and ^{41}K, and is currently operated throughout the ground tests of the MAIUS-B PP prior to launch.

The qualification process (see section 6.3) of the MAIUS-B PS and PP, including the new UHV system, was performed as a main part of this thesis. Throughout the vibration tests, conducted at the vibration test facility at the ZARM in Bremen, the PP was qualified up to a level of $19.6\,\mathrm{m\,s^{-2}_{RMS}}$ ($2.0\,\mathrm{g_{0RMS}}$). The expected maximum load level during the sounding rocket flight was given with $17.7\,\mathrm{m\,s^{-2}_{RMS}}$ ($1.8\,\mathrm{g_{0RMS}}$). For the qualification, the pressure was monitored and showed the performance of the UHV system under vibration loads. The qualification of the PP requires a pressure of below $5 \times 10^{-10}\,\mathrm{hPa}$ within 19 s after the 60 s test. These 19 s are derived from the flight mission, where 19 s after the load phase and the stage burnout, the experimental sequences start. At this point, the pressure is required to ensure a sufficient experiment performance. During the vibration test of the MAIUS-B PP at a level of $19.6\,\mathrm{m\,s^{-2}_{RMS}}$ ($2.0\,\mathrm{g_{0RMS}}$), the pressure level was reached within the 19 s and the qualification test was passed.

CF flange connections play a major role in the UHV design of current and future space missions. At the same time, as indicated by the qualification tests in section 6.3, the pressure rise during mechanical loads is caused by leakages through the CF connections. To investigate the leakage rate of CF flange connections, this thesis provides the first set of data on the influence of static loads. Therefore, a test setup (see 7.2.2) was designed and built throughout this thesis, to test CF DN40 flange connections as used within the MAIUS-B UHV system. Four test series were conducted to investigate the influence of the tightening torque (10 N m, 12.5 N m, 15 N m), the flange material (aluminum [*AluVaC®*], stainless steel [316LN-ESR, 14429-ESU]), and different OFHC copper gaskets (annealed, non-annealed).

For the performed tests, the applied force on the test flanges subsequently increased up to 1 950 N, which indicates when the first elastic and plastic leakages occur. In section 7.3, the findings of this thesis throughout the performed tests are discussed and presented in detail. TS1 and TS2 indicate

that for the two stainless steel flanges, a non-annealed copper gasket should be used with a tightening torque of 12.5 N m or 15 N m. However, for a tightening torque of 10 N m, the non-annealed copper gasket results in an elastic and plastic leakage for a lower applied force than for the annealed copper gasket.

TS3, with two aluminum flanges tested with the required annealed copper gasket, shows a similar behavior to stainless steel with a non-annealed gasket, for all tightening torques. The leakage rate increases in case of an elastic or plastic leakage, for aluminum compared to stainless steel, and is several orders of magnitude higher.

The TS4, with a flange connection made by one stainless steel flange and one aluminum flange, showed that a tightening torque of 10 N m is recommended. Throughout the tests, no elastic or plastic leakages within this tightening torque were measured. However, the tightening torque of 12.5 N m and 15 N m also showed no significant leakages.

While all tests indicate that in many cases a tightening torque of 15 N m seams to be advisable, is it important to state that this torque exceeds the standard tightening torque (10.4 N m) for the used stainless steel A2-70 screws. This could lead to material failure on longer time scales and result in damage and leakages within the UHV system. However, on the measured time scales, the data showed no direct disadvantage for the leakage rate of the CF flange connection.

This thesis has generated the first data set as seen in tables 7.3 and 7.4, which can be used for future UHV systems to optimize the design and the assembly process of space suitable UHV designs.

8.2 Outlook

The scientific payload of MAIUS-B on a sounding rocket, with a dual-species atom interferometer with ^{87}Rb and ^{41}K BECs, marks the next step towards future missions on the ISS or onboard a satellite. As the next milestones prior to launch, the payload will be fully assembled and integrated into the hull. This is followed by a bench and flight simulations test, and the final spin and vibration test campaign of the integrated payload. Once the payload has passed all tests, the flight ready payload is transported to the launch site in Sweden for the launch campaign MAIUS-2.

After the first flight campaign, the flight data will be investigated. In the time up to the MAIUS-3 launch, the payload will be investigated in detail to identify, repair, or exchange possibly damaged parts of the payload. In addition, further ground operations, optimizations and experiments are performed. Following the same procedure as for MAIUS-2, the scientific payload is transported again, prior to the launch campaign of MAIUS-3.

In parallel to this thesis, a new oven design is in development and currently being tested. The current design of the oven has a glass ampule which is broken, and can cause a high gas input when cracked, as well as produce glass debris which can block the flow. For the new design, the oven is filled in a separated oven filling chamber prior to the actual assembly into the vacuum system. Therefore, the new oven design should include a valve which can be remotely controlled. This allows for a transport from the oven filling chamber to the experiment. Such a design will also allow control of the rubidium and potassium partial pressure.

For future UHV system designs, alternative pumping concepts should be investigated, with consideration to the mass and the size. An investigation or a concept study for future UHV system designs could identify the usability of COTS systems for future space missions. However, new pumps would need to be vibration tested to qualify their ability to be used within a space mission.

The data on leakage rates for CS flanges under mechanical load, as provided within this thesis, can also be extended. The test setup design in this thesis could be used to test a wider range of materials, different screws, different CF flange sizes, or gasket types.

Such a data set could help to set up an FEM simulation as a prediction tool throughout the design process. In this case, the experimental data can be used to verify the simulation and identify flaws in the FEM model. Such a leakage rate prediction tool would identify which applied loads would result in a leakage. So far, it is only possible to identify possible design flaws of the vacuum system design during the vibration test, once the system is already finally assembled and pumped down. At this point, major design changes would cost time, money, and human resources, all limited throughout a space mission. If the prediction tool already indicates leakages during the design, changes can mostly be implemented in hours or days instead of months. An FEM based prediction tool is currently under development at the University of Bremen. In addition to static load tests, additional dynamic tests will be performed and the FEM model will be extended.

List of Figures

List of Tables

Bibliography

[Agu14] D. N. Aguilera, H. Ahlers, B. Battelier, et al. "STE-QUEST—test of the universality of free fall using cold atom interferometry". In: *Classical and Quantum Gravity* 31.11 (2014), p. 115010.

[Ahl16] H. Ahlers, H. Müntinga, A. Wenzlawski, et al. "Double bragg interferometry". In: *Physical review letters* 116.17 (2016), p. 173601.

[Alo22] I. Alonso, C. Alpigiani, B. Altschul, et al. "Cold Atoms in Space: Community Workshop Summary and Proposed Road-Map". In: *arXiv preprint arXiv:2201.07789* (2022).

[Amm97] H. Ammann and N. Christensen. "Delta Kick Cooling: A New Method for Cooling Atoms". In: *Phys. Rev. Lett.* 78 (1997), pp. 2088–2091. DOI: 10.1103/PhysRevLett.78.2088. URL: https://link.aps.org/doi/10.1103/PhysRevLett.78.2088.

[Ave20] D. C. Aveline, J. R. Williams, E. R. Elliott, et al. "Observation of Bose–Einstein condensates in an Earth-orbiting research lab". In: *Nature* 582.7811 (2020), pp. 193–197.

[Bal99] S. Bali, K. M. O'Hara, M. E. Gehm, et al. "Quantum-diffractive background gas collisions in atom-trap heating and loss". In: *Physical Review A* 60.1 (1999), R29.

[Bar13] B. Barrett, P-A. Gominet, E. Cantin, et al. "Mobile and remote inertial sensing with atom interferometers". In: *arXiv preprint arXiv:1311.7033* (2013).

[Bec18] D. Becker, M. D. Lachmann, S. T. Seidel, et al. "Space-borne Bose–Einstein condensation for precision interferometry". In: *Nature* 562.7727 (2018), pp. 391–395.

[Bos24] Bose. "Plancks Gesetz und Lichtquantenhypothese". German. In: *Zeitschrift für Physik* 26.1 (1924), pp. 178–181. ISSN: 0044-3328. DOI: 10.1007/BF01327326. URL: http://dx.doi.org/10.1007/BF01327326.

[Bur18] A. Burchianti, C. D'Errico, S. Rosi, et al. "Dual-species Bose-Einstein condensate of K 41 and Rb 87 in a hybrid trap". In: *Physical Review A* 98.6 (2018), p. 063616.

[Cac09] L. Cacciapuoti and C. Salomon. "Space clocks and fundamental tests: the ACES experiment". In: *The European Physical Journal Special Topics* 172.1 (2009), pp. 57–68.

[Ceg05] E. Ceglia. *European Users Guide to Low Gravity Platforms - Issue 2 Revision 0.* 2005.

[CNE21] CNES. *PHARAO.* Website. Available online at `https://pharao.cnes.fr/en/home-35` (Accessed on 7th of February 2021). 2021.

[Dep21] C. Deppner, W. Herr, M. Cornelius, et al. "Collective-Mode Enhanced Matter-Wave Optics". In: *Phys. Rev. Lett.* 127 (10 2021), p. 100401. DOI: 10.1103/PhysRevLett.127.100401. URL: https://link.aps.org/doi/10.1103/PhysRevLett.127.100401.

[Die98] K. Dieckmann, R. J. C. Spreeuw, M. Weidemüller, et al. "Two-dimensional magneto-optical trap as a source of slow atoms". In: *Phys. Rev. A* 58 (1998), pp. 3891–3895. DOI: 10.1103/PhysRevA.58.3891. URL: https://link.aps.org/doi/10.1103/PhysRevA.58.3891.

[DIN90] DIN. *Vakuumtechnik; Benennung und Definitionen; Allgemeine Benennungen.* Tech. rep. DIN 28400-1:1990-05. Deutsches Institut für Normung e.V., 1990.

[Dun14] H. Duncker, O. Hellmig, A. Wenzlawski, et al. "Ultrastable, Zerodur-based optical benches for quantum gas experiments". In: *Appl. Opt.* 53 (2014), pp. 4468–4474. DOI: 10.1364/AO.53.004468.

[Ein07] A. Einstein. "Über das Relativitätsprinzip und die aus demselben gezogenen Folgerungen". In: *Jahrbuch der Radioaktivität* 4 (1907), pp. 411–462.

[Ein24] A. Einstein. "Quantentheorie des einatomigen idealen Gases". In: *Sitzungsberichte Der Preussichen Akademie Der Wissenschaften* (1924), pp. 261–267.

[Ell18] E. R. Elliott, M. C. Krutzik, J. R. Williams, et al. "NASA's Cold Atom Lab (CAL): system development and ground test status". In: *npj Microgravity* 4.1 (2018), pp. 1–7.

[Els18] M. Elsen, J. Grosse, M. D. Lachmann, et al. "Final Design of the MAIUS-2/3 Payload – An Atom Interferometer on a Sounding Rocket". In: *Proc. of the 69th International Astronautical Congress*. 2018.

[Els21] M. Elsen, T. T. H. Dao, C. Braxmaier, et al. "Leakage rate detection of ConFlat seals in aluminum and stainless steel flanges under mechanical loads for quantum optical experiments in space". In: *Journal of Vacuum Science & Technology B* 39.6 (2021), p. 064204. DOI: 10.1116/6.0001525. eprint: https://doi.org/10.1116/6.0001525. URL: https://doi.org/10.1116/6.0001525.

[Els75] R. J. Elsey. "Outgassing of vacuum materials-II". In: *Vacuum* 25.8 (1975), pp. 347–361.

[Eng19] F. Engelmann. *Maschinenelemente kompakt*. Springer Berlin Heidelberg, 2019. DOI: 10.1007/978-3-662-57955-8. URL: https://doi.org/10.1007/978-3-662-57955-8.

[Ett06] J. Ettl. *Post Flight Report: TEXUS 42 (PRELIMINARY VERSION)*. Tech. rep. DLR-MR-TEXUS 42-0002. MORABA, German Aerospace Center, 2006.

[Far14] D. M. Farkas, E. A. Salim, and J. Ramirez-Serrano. "Production of rubidium bose-einstein condensates at a 1 hz rate". In: *arXiv preprint arXiv:1403.4641* (2014).

[Fol02] R. Folman, P. Krüger, J. Schmiedmayer, et al. "Microscopic atom optics: From wires to an atom chip". In: *Adv. At. Mol. Phys.* 48 (2002). DOI: 10.1016/S1049-250X(02)80011-8.

[Fry21] K. Frye, S. Abend, W. Bartosch, et al. "The Bose-Einstein condensate and cold atom laboratory". In: *EPJ Quantum Technology* 8.1 (2021), pp. 1–38.

[Gou10] D. Goujon, P. Rochat, P. Mosset, et al. "Development of the space active hydrogen maser for the aces mission". In: *EFTF-2010 24th European Frequency and Time Forum*. IEEE. 2010, pp. 1–6.

[Gra04] F. Grangeon, C. Monnin, M. Mangeard, et al. "Development of an ultra-high vacuum system for space application". In: *Vacuum* 73.2 (2004), pp. 243–248.

[Gre20] M. Greer. *Interface Definition Document (IDD) Nanoracks Mainframe (Nanode)*. Tech. rep. NR-NANODE-S0001. Nanoracks, 2020.

[Gro16a] J. Grosse. "Thermal and Mechanical Design and Simulation for the first High Precision Quantum Optics Experiment on a Sounding Rocket". PhD thesis. Universität Bremen, 2016.

[Gro16b] J. Grosse, S. T. Seidel, D. Becker, et al. "Design and qualification of an UHV system for operation on sounding rockets". In: *Journal of Vacuum Science & Technology A: Vacuum, Surfaces, and Films* 34.3 (2016), p. 031606.

[Gro17a] J. Grosse, S. Seidel, M. D. Lachmann, et al. "The MAIUS Sounding Rocket Missions – Recent Results, Lessons Learned and Future Activities". In: *Proc. of the 68th International Astronautical Congress*. 2017.

[Gro17b] J. Grosse, S. T. Seidel, D. Becker, et al. "Lessons Learned from the First Flight of an Atom Interferometer Payload on a VSB-30 Sounding Rocket Payload". In: *22nd ESA Symposium on European Rocket and Balloon Programmes and Related Research*. 2017.

[Her12] S. Herrmann, H. Dittus, C. Lämmerzahl, et al. "Testing the equivalence principle with atomic interferometry". In: *Classical and Quantum Gravity* 29.18 (2012), p. 184003.

[Her13] W. Herr. "Eine kompakte Quelle quantenentarteter Gase hohen Flusses für die Atominterferometrie unter Schwerelosigkeit". PhD thesis. Hannover, Germany: Gottfried Wilhelm Leibniz Universität Hannover, 2013.

[ISO07] ISO. *Vacuum technology-Bakable flanges-Part 2: Dimensions of knife-edge flanges*. Tech. rep. ISO/TS 3669-2:2007(E). International Organization for Standardization, 2007.

[Jou12] K. Jousten. *Wutz Handbuch Vakuumtechnik: Theorie und Praxis; 11th ed.* Wiesbaden: Vieweg+Teubner, 2012. URL: `https://cds.cern.ch/record/1562899`.

[Ket99] W. Ketterle, D. S. Durfee, and D. M. Stamper-Kurn. "Making, probing and understanding Bose-Einstein condensates". In: *arXiv preprint cond-mat/9904034* (1999).

[Kin19] A. P. King and R. Eckersley. *Statistics for biomedical engineers and scientists: How to visualize and analyze data*. Academic Press, 2019.

[Kir18] R. Kirchhartz, M. Hörschgen-Eggers, and W. Jung. "Sounding Rockets are unique Experimental Platforms". In: *69th International Astronautical Congress*. 2018. URL: `https://elib.dlr.de/125360/`.

[Kre05] U. Krengel. *Einführung in die Wahrscheinlichkeitstheorie und Statistik*. Vol. 8. Springer, 2005. DOI: 10.1007/978-3-663-09885-0.

[Kub16] A. Kubelka, S. Herrmann, J. Grosse, et al. "A three-layer magnetic shielding for the MAIUS-1 mission on a sounding rocket". In: *Rev. Sci. Instr.* 87.6 (2016), p. 063101. DOI: 10.1063/1.4952586.

[Kup13] M. E. Kupfer. "Analysis Of Low-Temperature Indium Seals For Hermetic Packaging Of Large-Area Photodetectors". PhD thesis. University of Illinois at Chicago, 2013.

[Kür20] C. Kürbis, A. Bawamia, M. Krüger, et al. "Extended cavity diode laser master-oscillator-power-amplifier for operation of an iodine frequency reference on a sounding rocket". In: *Appl. Opt.* 59 (2020), p. 253. ISSN: 1559-128X. DOI: 10.1364/ao.379955.

[Lan11] M. Landini, S. Roy, L. Carcagní, et al. "Sub-Doppler laser cooling of potassium atoms". In: *Physical review A* 84.4 (2011), p. 043432.

[Lau15] P. Laurent, D. Massonnet, L. Cacciapuoti, et al. "The ACES/PHARAO space mission". In: *Comptes Rendus Physique* 16.5 (2015), pp. 540–552.

[Lév09] T. Lévèque, A. Gauguet, F. Michaud, et al. "Enhancing the area of a Raman atom interferometer using a versatile double-diffraction technique". In: *Physical review letters* 103.8 (2009), p. 080405.

[Liu18] L. Liu, D. Lü, W. Chen, et al. "In-orbit operation of an atomic clock based on laser-cooled 87 Rb atoms". In: *Nature communications* 9.1 (2018), pp. 1–8.

[Liu21] Q. Liu, Y. Xie, L. Li, et al. "Development of an ultra-high vacuum system for a cold atom physics rack in space". In: *Vacuum* 190 (2021), p. 110192.

[Mac20] C. Maccarrone, P. Manassero, and C. Paolini. "Ion getter pumps". In: *arXiv preprint arXiv:2006.02721* (2020).

[Mih19] M. Mihm, J. P. Marburger, A. Wenzlawski, et al. "Acta Astronautica ZERODUR ® based optical systems for quantum gas experiments in space". In: *Acta Astronautica* 159 (2019), pp. 166–169. DOI: 10.1016/j.actaastro.2019.03.060.

[MM21] ME-Meßsysteme. *Kraftsensor KM30z 2kN*. 2021.

[MOR21] MORABA. *Orbiting laser interferometer to measure Earths gravity.* Website. Available online at `https://moraba.de/en/moraba/sounding-rockets/` (Accessed on 3rd of February 2021). 2021.

[Mos82] E. A. Moshey. "A compilation of outgassing data on vacuum materials". In: *Princeton Plasma Physics Laboratory Engineering Memorandum,(15 Feb 1982)* (1982).

[Muh03] D. Muhs, H. Wittel, D. Jannasch, et al. *Roloff/matek maschinenelemente.* Springer, 2003. DOI: 10.2172/1119379.

[Ols81] R.E. Olsen and J. Mockovciak. "Operational Factors Affecting Microgravity Levels in Orbit". In: *Journal of Spacecraft and Rockets* 18.2 (1981), pp. 141–144.

[Pet02] C. J. Pethick and H. Smith. "Bose-Einstein Condensation in Dilute Gases". In: *Cambridge University Press* (2002).

[Pfe13a] Pfeiffer. *Leak Detection Compendium.* Asslar: Pfeiffer Vacuum GmbH, 2013.

[Pfe13b] Pfeiffer. *Vacuum Technology Book Volume II.* Vol. Band 2 - Know-how Book. Asslar: Pfeiffer Vacuum GmbH, 2013.

[Phi98] W. D. Phillips. "Nobel Lecture: Laser cooling and trapping of neutral atoms". In: *Reviews of Modern Physics* 70.3 (1998), p. 721.

[Pie21] B. Piest. "Double-species Bose-Einstein condensation on an atom chip for a sounding rocket mission". PhD thesis. Gottfried Wilhelm Leibniz Universität Hannover, 2021.

[Rei99] J. Reichel, W. Hänsel, and T. W. Hänsch. "Atomic micromanipulation with magnetic surface traps". In: *Physical Review Letters* 83.17 (1999), p. 3398.

[Ren15] W. Ren, J. Xiang, Y. Zhang, et al. "Development of an ultrahigh vacuum system for space cold atom clock". In: *Vacuum* 116 (2015), pp. 54–59.

[Ren20] W. Ren, T. Li, Q. Qu, et al. "Development of a space cold atom clock". In: *National Science Review* 7.12 (2020), pp. 1828–1836.

[Rud10] J. Rudolph. "Towards atom interferometry in microgravity". PhD thesis. Hannover, Germany: Gottfried Wilhelm Leibniz Universität Hannover, 2010.

[Sab14] M. Sabbatini. *ESA User Guide to Low Gravity Platforms.* Tech. rep. HSO-K/MS/01/14, Issue 3 Revision 0. European Space Agency, 2014.

[SAE12] SAES. *CapaciTorr®Pumps MK5 Series*. Tech. rep. SAES Getters., 2012.

[Sah19] M. Sahelgozin. "Design and construction of a transportable quantum gravimeter and realization of an atom-chip magnetic trap". PhD thesis. Hannover: Institutionelles Repositorium der Leibniz Universität Hannover, 2019.

[Sei14] S. T. Seidel. "Eine Quelle für die Interferometrie mit Bose-Einstein-Kondensaten auf Höhenforschungsraketen". Phd. Thesis. Gottfried Wilhelm Leibniz Universität Hannover, 2014.

[Spa20] SpaceX. *FALCON USER'S GUIDE*. Tech. rep. 11.4. SpaceX, 2020.

[Spa21] SpaceX. *Capabilities & Services*. Website. Available online at `https://www.spacex.com/media/Capabilities&Services.pdf` (Accessed on 4th of February 2021). 2021.

[Sta13] A. Stamminger. "DLR's mobile rocket base - flight tickets for your microgravity experiments". In: *Proc. of the 64th International Astronautical Congress*. 2013.

[Ste19] D. A. Steck. *Rubidium 87 D Line Data*. Website. Available online at `https://steck.us/alkalidata/rubidium87numbers.pdf` (Accessed on 27th of February 2021). 2019.

[Tec15] Agilent Technologies. *AGILENT ION PUMPS - Technical Notes*. 2015.

[Tec19] Agilent Technologies. *VacIon Plus 20 pumps - User Manual*. 87-900-106-01 (I). 2019.

[Tie19] T. G. Tiecke. *Properties of Potassium*. Website. Available online at `https://www.tobiastiecke.nl/archive/PotassiumProperties.pdf` (Accessed on 27th of February 2021). 2019.

[Tin13] G. M. Tino, F. Sorrentino, D. N. Aguilera, et al. "Precision gravity tests with atom interferometry in space". In: *Nuclear Physics B-Proceedings Supplements* 243 (2013), pp. 203–217.

[Tou17] P. Touboul, G. Métris, M. Rodrigues, et al. "MICROSCOPE mission: first results of a space test of the equivalence principle". In: *Physical review letters* 119.23 (2017), p. 231101.

[VAC16] VACOM. *AluVaC - Lightweight UHV Chambers and Components with CF knife-edge*. Website. Available online at `file:///C:/Users/OUTGAS~1/AppData/Local/Temp/pib_aluvac_en_web.pdf` (Accessed on 16th of March 2021). 2016.

[VAC20a] VACOM. *Standard Components*. Website. Available online at file:///C:/Users/OUTGAS~1/AppData/Local/Temp/chapter_03_standard_components.pdf (Accessed on 11th of March 2021). 2020.

[VAC20b] VACOM. *Technical Information and Certificates*. Website. Available online at file:///C:/Users/OUTGAS~1/AppData/Local/Temp/chapter_00_technical_introduction-2.pdf (Accessed on 16th of March 2021). 2020.

[Wü22] Würth. *DIN/ISO- AND STANDARD PARTS6. Dimensioning metric screw assemblies*. 2022.

[War22] M. Warner, M. Elsen, J. Grosse, et al. "Outgassing rate testbed for in-operation analysis of powered and heated assemblies". In: *Journal of Vacuum Science & Technology B* 40.4 (2022), p. 044203. DOI: 10.1116/6.0001898. eprint: https://doi.org/10.1116/6.0001898. URL: https://doi.org/10.1116/6.0001898.

[Wel01] K. Welch. *Capture pumping technology*. Elsevier, 2001.

[Wel93] K. M. Welch, D. J. Pate, and R. J. Todd. "The Pumping of Helium and Hydrogen by Sputter-Ion Pumps Part II: Hydrogen Pumping". In: (1993). DOI: 10.2172/1119379. URL: https://www.osti.gov/biblio/1119379.

[Wic17] A. Wicht, A. Bawamia, M. Krüger, et al. "Narrow linewidth diode laser modules for quantum optical sensor applications in the field and in space". In: *Components and Packaging for Laser Systems III*. Vol. 10085. International Society for Optics and Photonics. SPIE, 2017, pp. 103 –118. DOI: 10.1117/12.2253655. URL: https://doi.org/10.1117/12.2253655.

[Wil04] S. Wildermuth, P. Krüger, C. Becker, et al. "Optimized magneto-optical trap for experiments with ultracold atoms near surfaces". In: *Physical Review A* 69.3 (2004), p. 030901.

[Zab33] R. M. Zabel. "Vapor pressure of vacuum cements". In: *Review of Scientific Instruments* 4.4 (1933), pp. 233–234.

[Ziv07] S. Zivanov, H. Schweda, D. Goujon, et al. "Physics package of the 35kg space active hydrogen maser for the ACES space mission of ESA". In: *2007 IEEE International Frequency Control Symposium Joint with the 21st European Frequency and Time Forum*. IEEE. 2007, pp. 637–641.

[Zoe10] T. van Zoest, N. Gaaloul, Y. Singh, et al. "Bose-Einstein condensation in microgravity". In: *Science* 328.5985 (2010), pp. 1540–1543.

List of Publications

Journals

M. Elsen, T. T. H. Dao, J. Grosse, and C. Braxmaier. "Leakage rate detection of ConFlat seals in aluminum and stainless steel flanges under mechanical loads for quantum optical experiments in space", J. Vac. Sci. Technol. B 39, 064204, 2021. (Peer-reviewed Publication)

M. Warner, M. Elsen, L. Wörner, J. Grosse, and C. Braxmaier. "Outgassing rate testbed for in-operation analysis of powered and heated assemblies", J. Vac. Sci. Technol. B 40, 044203 2022.

Proceedings

M. Elsen, J. Grosse, T. Wendrich, W. Bartosch, M. D. Lachmann, et al. "Sounding Rockets as a Pathway for Orbital Missions", Proc. of the 25th ESA Symposium on European Rocket and Balloon Programmes and Related Research, 2022, Biarritz, France.

M. Elsen, J. Grosse, E. M. Rasel, C. Braxmaier, and the MAIUS-Team. "The Pathway to Launch the MAIUS-2/3 Payload on a Sounding Rocket", Proc. of the 70th International Astronautical Congress (IAC), 2019, Washington, USA.

J. Grosse, M. Elsen, C. Braxmaier, and the QUANTUS-Team. "Thermal Control System for the MAIUS Atom Interferometer Payloads on a VSB-30 Sounding Rocket", Proc. of the 24th ESA Symposium on European Rocket and Balloon Programmes and Related Research, 2019, Essen, Germany.

M. Elsen, J. Grosse, T. Wendrich, W. Bartosch, D. Becker, et al. "Final Design of the MAIUS-2/3 Payload – An Atom Interferometer on a Sounding Rocket", Proc. of the 69th International Astronautical Congress (IAC), 2018, Bremen, Germany.

J. Grosse, O. Kouker, P. Laschewski, B. Lockett, M. Elsen, et al. "SECAMP - Student Experiments with Cold Atoms on Micro- and Hypergravity Platforms", Proc. of the 69th International Astronautical Congress (IAC), 2018, Bremen, Germany.

J. Grosse, S. T. Seidel, M. D. Lachmann, D. Becker, M. Elsen, et al. "The MAIUS Sounding Rocket Missions – Recent Results, Lessons Learned and Future Activities", Proc. of the 68th International Astronautical Congress (IAC), 2017, Adelaide, Australia.

M. Elsen, J. Grosse, K. Döringshoff, T. Wendrich, B. Piest, et al. "Design of the MAIUS-2/3 Atom Interferometer on a Sounding Rocket", Proc. of the 67th International Astronautical Congress (IAC), 2016, Guadalajara, Mexico.

Conference Talks

M. Elsen, J. Grosse, T. Wendrich, W. Bartosch, M. D. Lachmann, et al. "Sounding Rockets as a Pathway for Orbital Missions", 25th ESA Symposium on European Rocket and Balloon Programmes and Related Research, 2022, Biarritz, France.

M. Elsen, J. Große, T. Wendrich, B. Piest, M. D. Lachmann, et al. "Assembly, Integration and Test of the MAIUS-B Payload for the Sounding Rocket Missions MAIUS-2/3", 43nd COSPAR Scientific Assembly, 2021, Virtual Conference.

M. Elsen, J. Grosse, E. M. Rasel, C. Braxmaier, and the MAIUS-Team. "The Pathway to Launch the MAIUS-2/3 Payload on a Sounding Rocket", 70th International Astronautical Congress (IAC), 2019, Washington, USA.

M. Elsen, J. Grosse, E. M. Rasel, C. Braxmaier, and the MAIUS-Team. "Technologies and Concepts of the UHV System for the MAIUS-2/3 Sounding Rocket Missions", 21st International Vacuum Congress (IVC), 2019, Malmö, Sweden.

M. Elsen, J. Grosse, T. Wendrich, W. Bartosch, D. Becker, et al. "Final Design of the MAIUS-2/3 Payload – An Atom Interferometer on a Sounding Rocket", 69th International Astronautical Congress (IAC), 2018, Bremen, Germany.

M. Elsen, J. Große, D. Becker, B. Piest, M. D. Lachmann, et al. "An Ultra-High Vacuum System for the MAIUS-2/3 Atom Interferometer on a Sounding Rocket", 42nd COSPAR Scientific Assembly, 2018, Pasadena, USA.

M. Elsen, J. Große, D. Becker, B. Piest, M. D. Lachmann, et al. "An Ultra-high vacuum system for the atom interferometer of the MAIUS-B sounding rocket payload", DPG-Frühjahrstagung, 2018, Berlin, Germany.

M. Elsen, J. Grosse, K. Döringshoff, T. Wendrich, B. Piest, et al. "Design of the MAIUS-2/3 Atom Interferometer on a Sounding Rocket", 67th International Astronautical Congress (IAC), 2016, Guadalajara, Mexico.

Supervision

In the dissertation the results from the supervision of the following students' works are included:

- Thi Thu Hien Dao. "Experimental and Numerical Investigation of the Leakage Rate of Vacuum Sealing Technologies under the Influence of Static Loads", Master Thesis, University of Bremen, 2019.
- Felix Gümpel & Torsten Raupach. "UHV Technologies for quantum applications in space", Student Project, University of Bremen, 2022.

This dissertation has been editorially revised for publication. The changes were made in consultation with Prof. Claus Braxmaier and Prof. Hansjörg Dittus, as part of the doctoral procedures.